Kent Academic Repository

OPTICAL METHODS OF ACOUSTIC DETECTION

A THESIS SUBMITTED TO
THE UNIVERSITY OF KENT AT CANTERBURY
IN THE SUBJECT OF PHYSICS
FOR THE DEGREE OF DOCTOR OF PHILOSOPHY

By

Sean Francis O'Neill

September 2000

Contents

5.   Use of Low-Finesse Interferometric Cavities

as Ultrasonic Sensors

6.   Acoustic Detection using Er^{3+} Fibre Bragg Grating Lasers.

Abstract

This thesis details the experimental investigation of a fibre Bragg gratings (FBG) as to its suitability as a point ultrasonic sensor for medical applications, the FBG being interrogated by a low-coherence psuedo-heterodyne technique. The noise-limited pressure resolution of the FBG sensor was found to be *4.5kPa/√Hz* at a frequency of 1.911 MHz. The ability of the FBG sensor to accurately determine the spatial field profile from a focussed ultrasonic transducer was also investigated and compared with results obtained from a commercially available piezoelectric hydrophone. Ultrasonic shielding materials on the bare optical fibre were also experimentally investigated in an attempt to provide a more localised grating response to the ultrasonic field.

The ultrasonic response of low-finesse Fabry-Perot cavities based around 50μm thick polymer films was also investigated as a potential alternative to the use of fibre Bragg gratings, the cavity being interrogated by a low-coherence interferometric heterodyne technique. The noise-limited pressure resolution for a low-finesse Fabry-Perot cavity based on a 50μm thick polyethylene teraphthalate film was found to be *72 Pa/√Hz* at an ultrasonic frequency of 1.911 MHz and *11 Pa/√Hz* at 612 kHz. The ability of this cavity sensor to spatially resolve the ultrasonic field profile was also examined experimentally.

Finally, the use of in-fibre Er^{3+} FBG based lasers as acoustic sensors in the frequency range 200Hz– 20 kHz was examined experimentally using a heterodyne interferometric interrogation method to assess the potential of these devices as highly sensitive acoustic sensors for military applications. The noise limited pressure resolution of the most sensitive fibre laser was found to be *4×10^{-3} Pa/√Hz* over a frequency range of 4-6 kHz. An array of 4 distributed feedback fibre lasers was constructed and two separate methods of demultiplexing the laser array were compared and contrasted. The limiting system noise sources were also measured where possible.

Acknowledgements

Chapter 1

1.1 Introduction

The most familiar type of acoustic sensor is the human ear. The human ear shares some characteristics with artificial methods of acoustic detection, and hence a brief discussion of the ear affords a relatively easy introduction to some of the concepts encountered later when discussing artificial methods of acoustic (and ultrasonic detection). These concepts can be briefly summarised as follows:-

- frequency range.
- frequency selectivity.
- dynamic range.
- mechanical amplification.
- mechanical resonance.
- directional sensitivity.

In the ear, the acoustic field is transduced into a mechanical displacement by the eardrum. The small mechanical movements of the eardrum are mechanically amplified by an interconnected series of bones known as the hammer, anvil and stirrup, collectively known as the ossicles. The resultant mechanical displacement of the ossicles is transmitted into the cochlea via another membrane called the oval window, where hairs in the cochlea connected to electrically sensitive nerve endings provide both acoustic detection and frequency selective signal processing, the end result being further interpreted by the brain as, for example, speech, music or noise. A schematic diagram of a human ear is given in figure 1.1 overleaf. The Eustachian tube provides pressure equalisation between the inner and outer ear. The semicircular canals provide the ability to balance and to detect motion.

Semicircular Canals (3)

Stirrup

Anvil

Nerves

Hammer →

connects
to the
brain

Pinna

Cochlea

Eardrum

Outer Ear
Canal

Eustachian
Tube

connects to
the nose
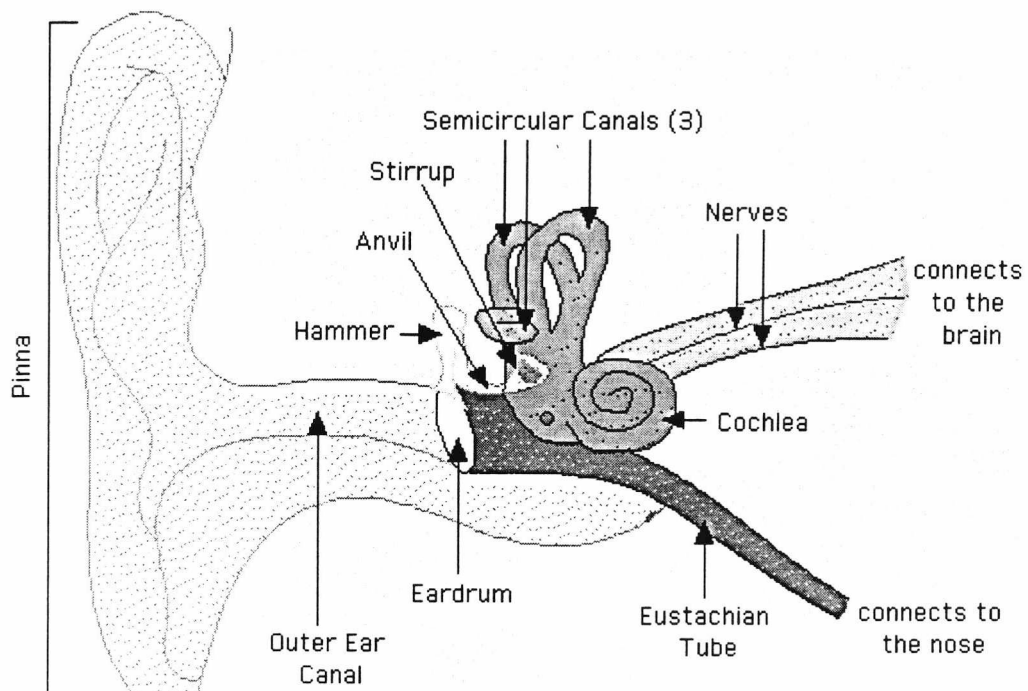
Figure 1.1 – Schematic diagram of human ear.

The pinna or outer ear provides some degree of directional sensitivity as well as capturing more acoustic energy than the outer ear canal alone. The sound waves are channelled through the outer ear canal and impinge on the eardrum. Mechanical amplification by the hammer, anvil and stirrup bones takes place as mentioned previously. Additional amplification takes place by virtue of resonances of the air column in the closed ear canal (analogous to resonances in an organ pipe). These closed tube resonances occur at approximately 3.7 and 13kHz, although these figures are obviously dependent on the size of the ear canal. The larger surface area of the eardrum compared to the cochlear oval window also provides some degree of mechanical amplification. The extra mechanical amplification afforded by the combined effect of the outer ear, inner ear resonances, ossicles and the larger area of the eardrum compared to the cochlear oval window is approximately a factor of 100, (or 20 decibels). Typical representative parameters for the human ear, ignoring age related effects (loss of high frequency sensitivity, for example) are summarised in Table 1.1 overleaf.

Parameter	Range
Frequency range	20Hz – 20 kHz
Dynamic range	2×10^{-5} – 60 Pa (10^{-12} – 10 W/m^2)
Threshold sensitivity	2×10^{-5} Pa
Frequency selectivity	1 Hz
Amplitude selectivity	1 dB
Frequency of peak sensitivity	3.5 - 4.0 kHz

Table 1.1 – Performance characteristics of the human ear

The frequency range corresponds to the minimum and maximum detectable frequencies. The dynamic range is defined as the difference between the minimum and maximum detectable pressures (or intensities) at 1kHz. The minimum detectable pressure is also known as the threshold of audibility. The maximum detectable pressure is known as the pain threshold. On a decibel scale, the threshold intensity of audibility is assigned a value of 0 dB at 1 kHz, the pain threshold being around 130 dB. Frequency selectivity is the ability to discriminate between closely spaced frequencies. Amplitude selectivity is the ability to distinguish between sounds of the same frequency but with different amplitudes. Figure 1.2 shows the ear's sensitivity as a function of frequency, as well as other interesting features.
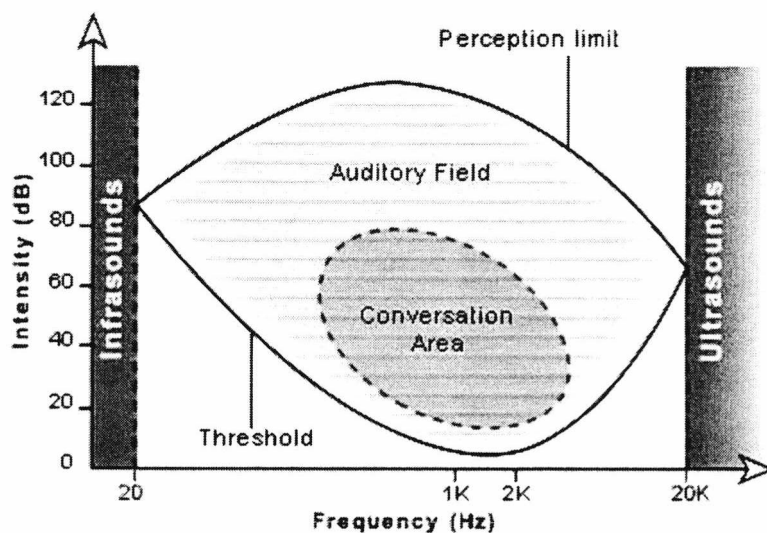
Figure 1.2. Characteristics of human hearing range.

Also shown in figure 1.2 is the distinction between sounds too high or low in frequency to be audible (ultrasound and infrasound). Audible (or acoustic) frequencies are those in the range 20Hz to 20kHz. The frequency range and intensity of normal speech is also shown (dotted oval area), as is the dynamic range (the difference between the upper and lower bounding curves). The dynamic range is obviously frequency dependent. The concepts outlined in this brief description of the characteristics of the human ear are directly transferable to a discussion of the required characteristics of artificial means of acoustic detection. The ideas of frequency and dynamic range, peak frequency sensitivity, mechanical resonances and threshold of audibility all have direct analogues when discussing other forms of acoustic detector.

This thesis is concerned with the investigation of optical methods of acoustic and ultrasonic detection, with a particular emphasis on medical aspects of ultrasonic sensing. These aspects are discussed more comprehensively in subsequent chapters. However, the three aims of this thesis are given below and will be expanded on in more detail in subsequent chapters.

1. The experimental investigation of fibre Bragg gratings as to their suitability as ultrasonic detectors for therapeutic medical applications of high-intensity focused ultrasound in the MHz frequency range.

2. The experimental investigation of an extrinsic low-finesse Fizeau cavity as to its suitability as an ultrasonic detector, again for therapeutic medical applications of high-intensity focused ultrasound in the MHz frequency range.

3. The experimental investigation of an array of erbium fibre lasers with an aim to construction of a multiplexed array which could be used as a highly sensitive hydrophone array in the frequency range 200Hz to 20 kHz.

The next sections of this chapter are concerned with an overview of optical fibre sensors with a particular emphasis on the types of sensors and interrogation techniques employed in the experimental work described in subsequent chapters.

1.2   Fibre-Optic Sensing Concepts

A fibre-optic sensor may be broadly defined as a device in which an optical signal is modulated in response to a measurand field. Fiber optic sensors are often loosely grouped into two basic classes referred to as extrinsic (or hybrid fiber optic sensors), and intrinsic (or all-fiber sensors).

In the case of an extrinsic sensor an optical fiber leads up to a modulating element which impresses information onto the light beam in response to an environmental effect. The information could be impressed in terms of modulating the intensity, phase, frequency, polarization, or spectral content of the light in the fibre. An optical fiber then carries the light with the environmentally impressed information back to an optical and/or electronic processor for signal recovery to allow useful information about the measurand field to be obtained. In some cases the input optical fiber also acts as the output fiber. The intrinsic or all fiber sensor uses an optical fiber to carry the light beam and the environmental effect impresses information onto the light beam while it is in the fiber. Each of these classes of fiber sensor has many subclasses [1] that consist of large numbers of fiber sensors.

1.2.1   Interferometric Sensors

In an interferometric sensor the effect of the measurand is to modulate the phase of the electric field, where phase is converted to an intensity change in the interferometer. The simplest kind of interferometry is an optical arrangement that causes two mutually coherent beams of light to follow physically distinct paths. One of those paths contains the sensing fibre and the other path is used as a reference. When the two beams are combined on a photodetector then they produce a resultant intensity that changes periodically with the phase difference, with periodicity 2π. A polarimetric sensor can be thought of as one in which the two beams occupy essentially the same volume of space but differ by the orthogonality of their states of polarisation. In order to make the two orthogonal states interfere on a detector, they must each be resolved to give components in a common direction. For example, by placing a polariser in the output of a highly birefringent fibre, the two modes are made to interfere provided that the

azimuth of the polariser does not coincide with that of just one of the modes. All practical detectors of optical radiation are non-linear in that they respond to the power of the radiation rather than its electric field strength, averaged over some time period which is long in comparison with the period of an individual optical wavelength.

1.2.2   Mach-Zehnder interferometer.

A common form of optical fibre interferometer is the Mach-Zehnder configuration, with a simple example shown in figure 1.3
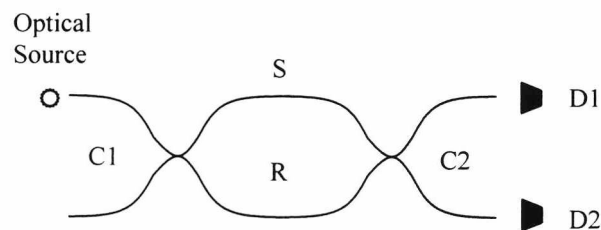
Figure 1.3 Fibre Mach-Zehnder interferometric sensor

The source is coupled into a single mode fibre downlead and is amplitude-divided by coupler C1 into two fibre arms, which can be thought of as representing a *signal* beam (S) and a *reference* beam (R), the measurand modifies the phase of the signal beam, whereas the reference beam has a constant environment. The two beams then recombine at a second directional coupler (C2) terminating at photodetectors D1 and D2 giving an electrical output proportional to the power incident upon them. It can be shown (see later chapters) that the detector signals are given by equations of the form: -

$$I_1 = I_0 \left(1 + V \cos(\phi_a - \phi_B) \right) \tag{1.1}$$

$$I_2 = I_0 \left(1 - V \cos(\phi_a - \phi_B) \right) \tag{1.2}$$

where ϕ_A and ϕ_B are the phases for the signal and reference beams, I_0 is a mean signal intensity, and V is the visibility of the interference. The visibility depends on the relative intensity of the signal and reference beams, their relative states of polarisation, and their mutual coherence. In the optimum case, the relative intensities and states of

polarisation are equal and the optical path length difference between the signal and reference beams is much smaller than the coherence length of the detected light. Under these optimum conditions, the visibility is unity. In practical circumstances the visibility can take any value between zero and unity. The two outputs are in antiphase, so that the sum of the two outputs is constant irrespective of relative phase. Having access to the two outputs can be used to compensate for the effect of changing source intensity. The relative intensities of the two beams depend on the coupling coefficients of the directional couplers used, fixed during manufacture for fused fibre couplers. The relative state of polarisation depends on the birefringence of the fibres and the couplers. Whilst it is possible to fabricate the entire interferometer from highly birefringent fibre and components, and to work with a fixed polarization eigenstate, most interferometers are constructed from normal cylindrically symmetric core monomode optical fibre, as were the interferometers used in the experiments described in this thesis. Therefore environmental effects cause the recombining states to be unequal. Under these circumstances, some form of explicit birefringence control is needed to preserve visibility. One common means is to induce controlled birefringence by bending the fibre [2]. The coherence length is dominated by the spectral properties of the source.

1.2.3   Michelson interferometer

Closely related to the Mach-Zehnder interferometer is Michelson's spectral interferometer, shown in figure 1.4.
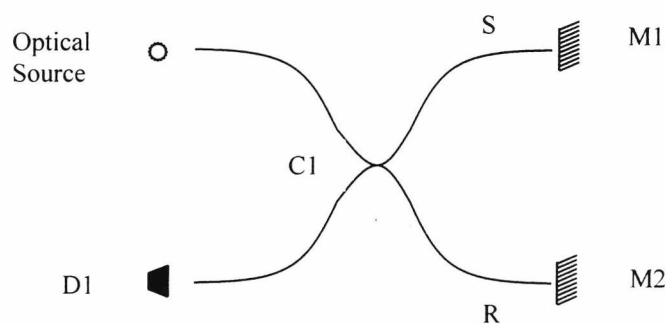
Figure 1.4 Michelson Interferometer.

Here the signal and reference beams terminate in reflectors (M1, M2) so that they are folded back on themselves to recombine at the same coupler (C1) that was used to divide them. The double-pass of the signal beam effectively doubles the sensitivity of the interferometer. However, directing one of the interferometer outputs into the source is disadvantageous as such feedback causes instabilities [3], especially with diode lasers. In practical situations it is usually necessary to incorporate an optical isolator between the source and the coupler. The normal choice of isolator is of the Faraday type: a linearly polarised incident beam passes through an aligned polariser, and then via a magneto-optic crystal in a permanent magnetic field that rotates the polarisation azimuth by $\pi/4$ radians to be aligned with a polarisation analyser at the output. Thus, a counter-propagating (feedback) beam passing through the device will have its polarisation azimuth rotated in the crystal so that it cannot pass through the polariser. The recombining beams in the output arm of the Michelson interferometer are always of equal intensity, irrespective of the coupling ratio. However, the highest mean intensity is achieved for a 50:50 split ratio. Polarisation effects are similar to those in the Mach-Zehnder interferometer. However, there is an interesting means of ensuring equality of polarisation states without having to resort to an adjustable polarisation controller, in which the reflectors at the distal ends of the signal and reference fibres are replaced by Faraday mirrors. These devices are essentially the same as Faraday optical isolators from which the polarisers have been removed. Thus, the returning signal and reference beams are in the states orthogonal to those of the outgoing beams, so that they return to the coupler in the same states as when they left it, irrespective of any birefringence en route, thus optimising the visibility.

1.2.4   Sagnac Interferometer

An important two-beam interferometer is the Sagnac interferometer, shown in figure 1.5 overleaf.
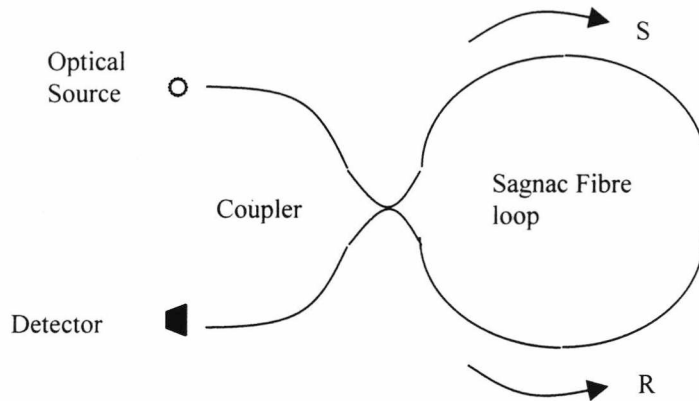
Figure 1.5 Fibre Sagnac interferometer.

The fibre Sagnac interferometer has been developed principally as a gyroscope for the purpose of measuring angular velocity [4]. The signal (S) and reference (R) beams now occupy the same space and are the clockwise and counter-clockwise beams propagating in the loop of fibre that forms the interferometer. At first sight it would appear that the phase difference between the beams would always be zero, as it is for all reciprocal effects i.e. those where the sign (positive or negative) of the effect is independent of the direction of travel through the interferometer. However, non-reciprocal effects, such as angular velocity [5] and magnetic fields [6] all produce a phase shift. Figure 1.5 shows the simplest possible version of the interferometer.

1.2.5   Multiple beam interferometers

So far only arrangements in which two beams interfere have been considered. However, multiple beam interferometry is also used in optical sensing. The most familiar form of multiple-beam interferometer is the Fabry-Perot. This is shown with a fibre optic arrangement and external reflectors in figure 1.6 overleaf.
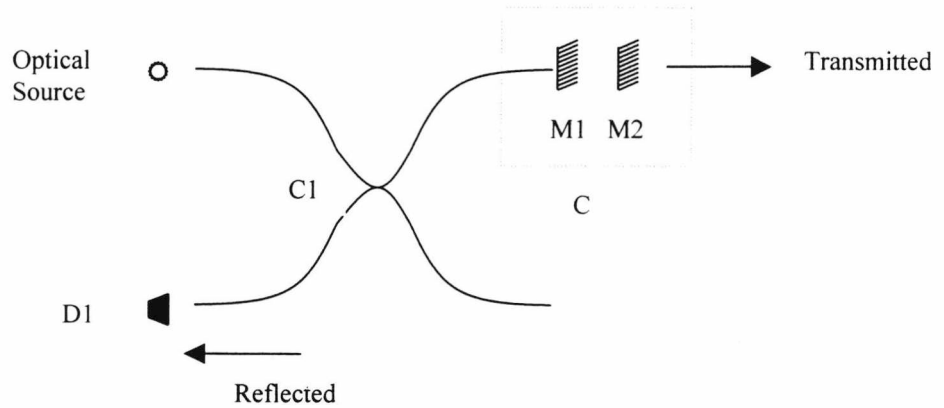
Figure 1.6 Extrinsic Fabry-Perot Interferometer.

The transfer function of the Fabry-Perot is given by the Airy function [7].

$$I = \frac{I_0}{1 + F\sin^2\left(\frac{\phi}{2}\right)}, \quad F = \frac{4R}{(1-R)^2} \tag{1.3}$$

where ϕ is the round-trip phase difference between the mirrors M1, M2 and F is the finesse. R is the mirror reflectance and attenuation is neglected. The effect of the multiple transitions of the signal beam backwards and forwards between the mirrors that form the cavity is to increase the sensitivity to measurand-induced phase changes. The finesse and reflectivity are related, as shown in figure 1.7.
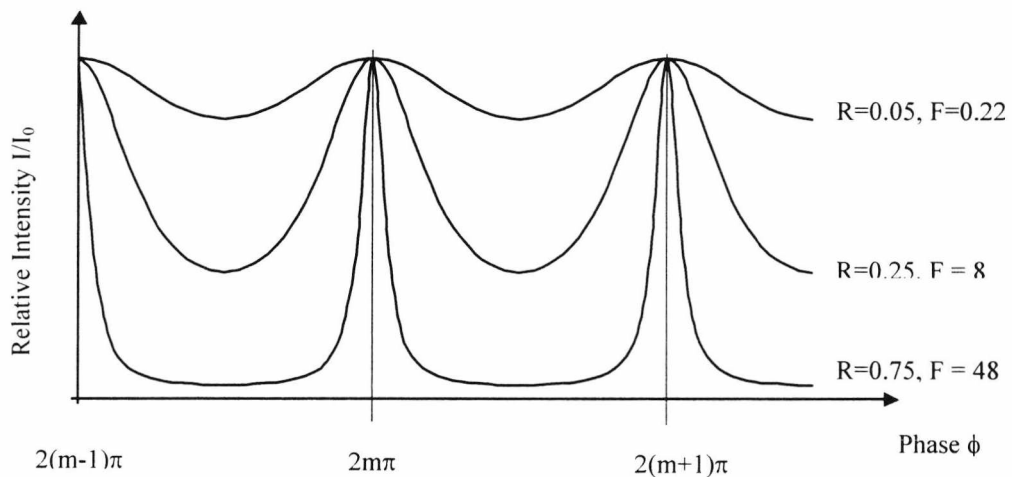
Figure 1.7 Relationship between reflectivity, finesse and round-trip phase difference for a Fabry-Perot interferometer.

A common form of Fabry-Perot uses the natural Fresnel reflection of about 4 % that takes place at the uncoated fibre-air interface at the cleaved fibre ends. Under those circumstances, the transfer function is more like the low-finesse case shown in figure 1.7. Alternatively an extrinsic sensor can be fabricated using materials other than silica optical fibre [8]. In-fibre Bragg gratings have also been used to define the mirrors to form the interferometer [9]. The extreme limit of low-finesse corresponds to two-beam interference, in which case the arrangement is more properly called a Fizeau interferometer. The Fizeau interferometer operated in reflection gives good visibility provided that the two reflections are of comparable intensity [10].

1.2.6   Polarimetric Sensors

Figure 1.8 shows a simple arrangement for a polarimetric fibre sensor.
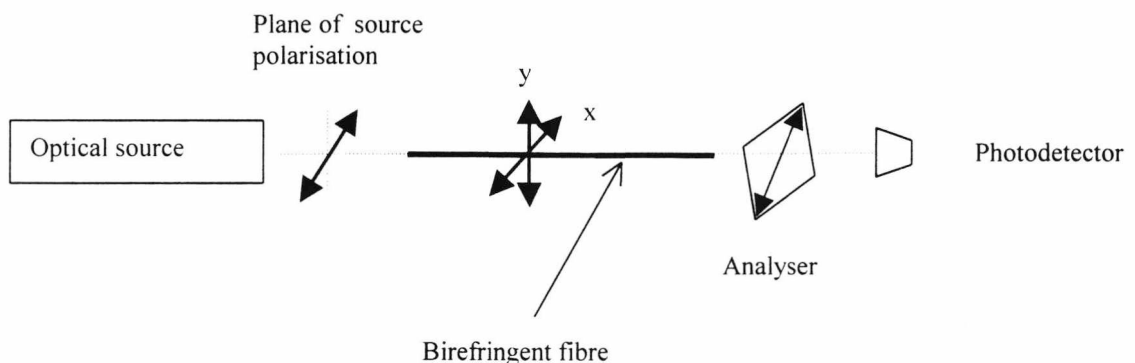
Figure 1.8 Polarimetric fibre sensor configuration.

A linearly polarised source is used, which couples to the two polarisation eigenmodes of a fibre with high linear birefringence. The two states of polarisation are now the equivalents of the signal and reference beams of the interferometer. The states propagate through the fibre, acquiring a measurand-dependent phase difference as described previously. Orthogonal states of polarisation do not interfere. Thus a polarisation analyser is used to resolve the two states into a common azimuth so that they interfere. As before, the visibility depends on the relative intensities of the recombining modes. Optimum intensity and visibility are achieved by using a source

polarised at $\pi/4$ radians to the fibre polarisation eigenaxes (x, y on figure 1.8), and an analyser at $\pi/4$ to the eigenaxes at the output. The simple sensor arrangement shown in figure 1.8 has successfully been used to construct distributed acoustic sensors, as demonstrated in [11].

1.3. Low coherence interferometry.

In an interferometer, fringes are visible only when the optical path difference is less than the source coherence length, where the coherence length, l_C is inversely proportional to the spectral width $\Delta\lambda$ of the source, $l_C \sim \lambda/\Delta\lambda$. When an interferometer is illuminated with a low-coherence source, it is possible to identify the position of zero optical path difference (OPD) by looking for the highest visibility fringe [12]. It is possible to measure the OPD of a remote sensing interferometer using a tandem interferometer arrangement [13], as shown in figure 1.9 below.
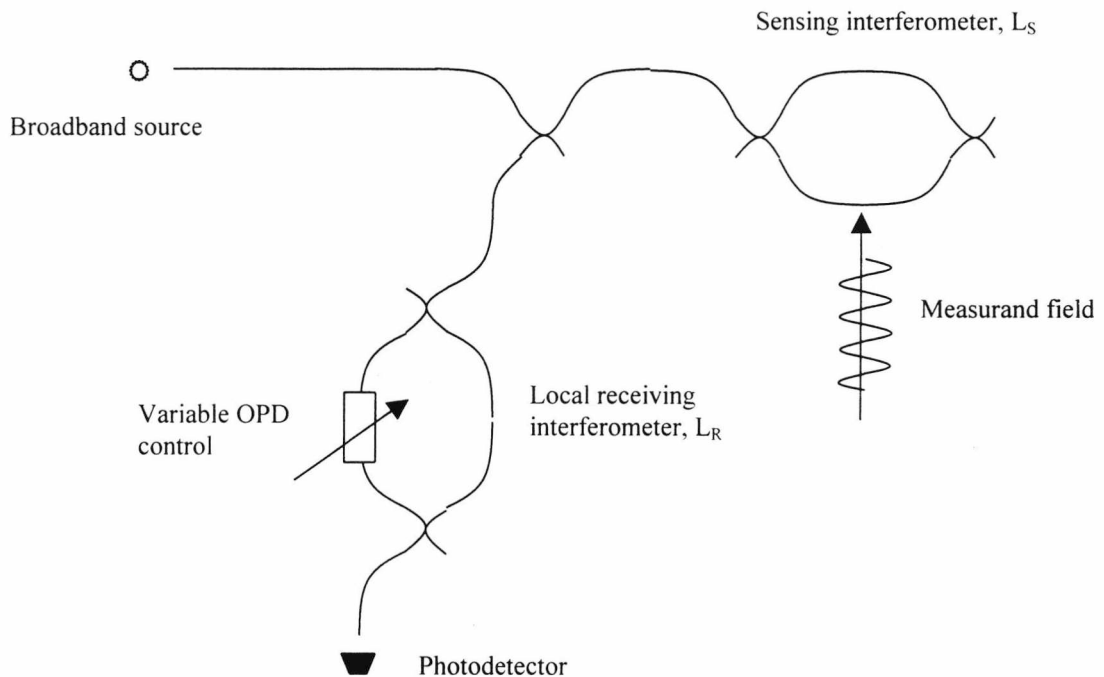
Figure 1.9 Tandem interferometer arrangement for low–coherence interferometry.

The sensing interferometer has an OPD (= L_S) greater than the source coherence length and no fringes are produced. Consider what happens as the OPD (= L_R) of the local receiving interferometer is scanned. When L_R is zero, then interference fringes are observed. As L_R is increased beyond the source coherence length, the fringes disappear. As L_R is increased further to approach L_S, then interference is possible. When the condition $|L_R - L_S| < l_C$, the source coherence length, then fringes are again observed. Therefore fringe visibility shows a local maximum when the OPDs of the sensing and receiving interferometers match. It is then relatively straightforward to measure the OPD of the sensing interferometer separately in order to recover the measurand. The exact derivation of the tandem interferometer transfer function can be found in [14]. A tandem low-coherence interferometer transfer function is given in figure 1.10.

Interference
Intensity

$|L_R - L_S| = 0$ $L_R = 0$ $|L_R - L_S| = 0$
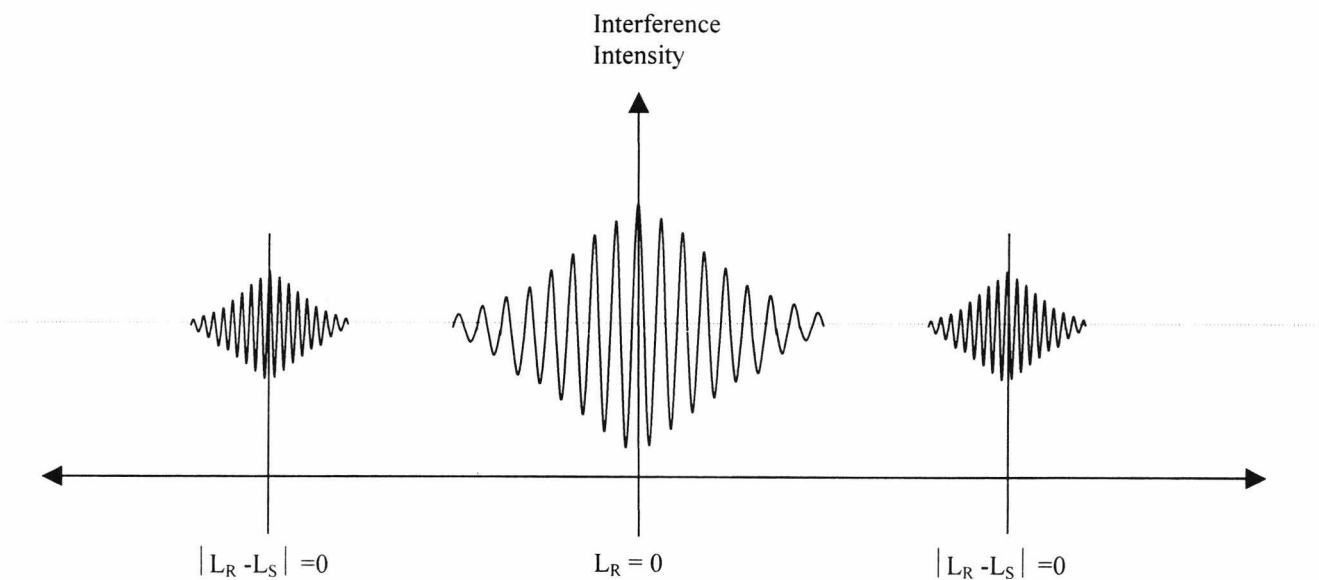
Figure 1.10 Tandem low-coherence interferometer transfer function

Practical schemes differ in the means used to scan the OPD and to analyse the interferograms produced. Path length scanning can use mechanical translation of the mirror in one arm of a bulk optic receiving interferometer [14].

For simple applications, analysis of the data need only be the identification of the central fringe. Higher performance can be achieved by capturing the complete interferogram and then using Fourier transform techniques to find the OPD [15]

1.4. Phase Recovery

In the two-beam interferometers discussed previously, the signal recorded by the detector takes the form of equations 1.4 and 1.5, i.e:

$$I_1 = I_0\left(1 + V\cos(\phi_a - \phi_B)\right) \tag{1.4}$$

$$I_1 = I_0\left(1 - V\cos(\phi_a - \phi_B)\right) \tag{1.5}$$

where ϕ_A and ϕ_B are the phases of the signal and reference beam. Figure 1.11 shows that the amplitude of the output intensity change for a given phase change is greatest where the transfer function is steepest, i.e. at position A rather than position B.
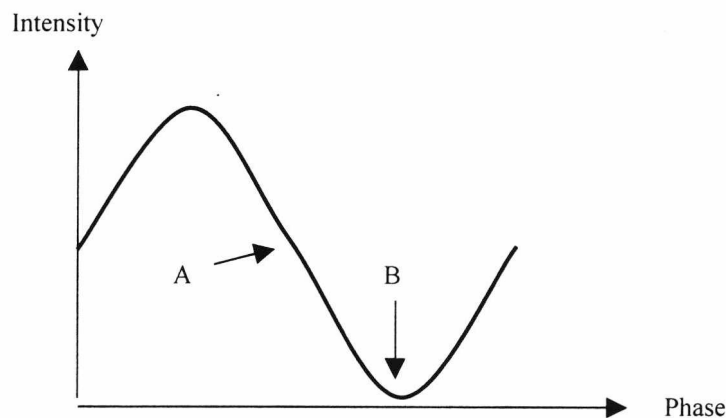
Figure 1.11 Quadrature point (A) of two-beam interferometer transfer function.

The position of greatest sensitivity corresponds to the so-called quadrature condition, where $\phi_A - \phi_B = \pi/4 + N\pi$, N being an integer. In a practical interferometer, slowly varying changes in ϕ_B are inevitable due to environmental effects, so that the phase sensitivity of the interferometer continually drifts.

Homodyne techniques depend on controlling ϕ_B to maintain the quadrature position. This technique actively controls the phase in the reference arm of the interferometer by using a piezoelectric cylinder to stretch the fibre and hence compensate for environmentally induced phase differences [16]. An electronic servo loop applies a voltage to the cylinder to maintain the phase at a fixed value. If the bandwidth of the servo loop is wide enough to encompass the measurand bandwidth, then the voltage changes applied to the piezo cylinder to maintain the interferometer at quadrature follow the measurand.

As an alternative to modulating the reference arm optical path length, it is possible instead to modulate the source wavelength, as $\phi_A - \phi_B = 2\pi L/\lambda$, where L is the OPD. This technique has been used with diode laser sources [17], where the wavelength can be modulated over a limited range by controlling the injection current [18]. Thus an arrangement can be constructed in which the feedback loop operates on the diode current rather than on an explicit phase modulator.

Heterodyne schemes represent an alternative to homodyne ones. Here, a frequency shift is applied to the reference beam to produce a signal of the form

$$I = I_0[1 + V\cos(\phi_A - \phi_B + \omega t)] \tag{1.6}$$

producing a phase modulated carrier, which can be demodulated by a phase-locked loop or frequency discriminator. To produce the frequency shift, fibre pigtailed optic components such as acousto-optic Bragg cells can be used. Alternatives involve using periodic frequency shifts, e.g. using a piezoelectric fibre stretcher or by wavelength modulation of a diode laser by controlling its current in an unbalanced interferometer [18]. Integrated optic phase shifters are also suitable. Both acousto-optic Bragg cells and an integrated optic phase shifter are used in this thesis. The use of a heterodyne interrogation technique is discussed more extensively in Chapter 3 of this thesis.

1.5   Fibre Bragg Gratings.

Fibre Bragg Gratings (FBGs) take the form of a periodic refractive index modulation in the core of an optical fibre. The grating can be written into the fibre core by the interference pattern formed by coherent intersecting beams from an ultraviolet laser [24,25], as a spatial modulation in the fibre refractive index, with a period of Λ. The refractive index profile $n(z)$ along the longitudinal (z) axis of the fibre is given by :

$$n(z) = n_{core} + \delta n \left[1 + \cos\left(\frac{2\pi z}{\Lambda} \right) \right] \qquad (1.7)$$

where n_{core} is the refractive index of the fibre core, δn is the amplitude of the refractive index modulation and Λ is the perturbation period. The grating peak wavelength reflectivity λ_B is given by the Bragg condition, and is $\lambda_B = 2n\Lambda$. The periodic refractive index variation in the fibre core gives rise to a highly wavelength selective structure which can be used as a sensor [26], as environmentally-induced variations in the grating period (e.g. due to strain, pressure, temperature) shift the reflectivity peak of the grating. The manufacture and properties of FBGs are described more fully in chapter 2. For the moment, the essential features of FBGs are that they can be easily multiplexed onto the same fibre due to their wavelength selectivity. Figure 1.12 below shows a schematic representation of the refractive index variation in the fibre core and the resultant wavelength response of the grating. $R(\lambda)$ is the grating reflectivity as a function of wavelength. The depth and period of the refractive index variation have been exaggerated for sake of clarity.
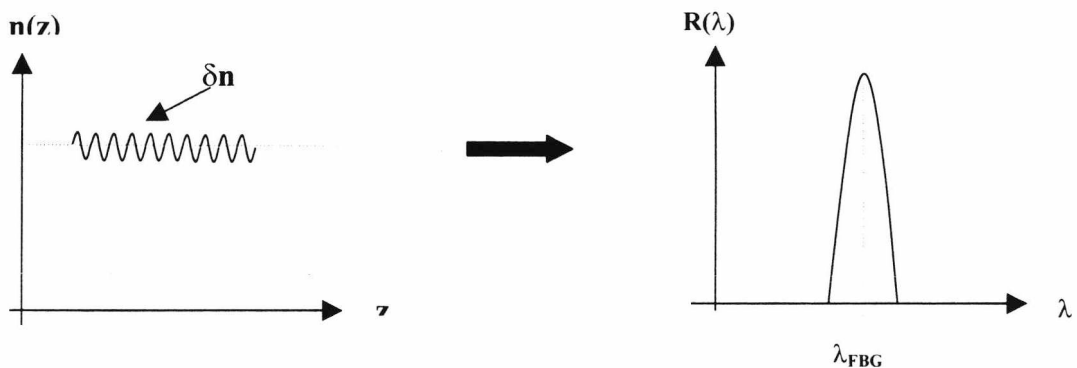
Figure 1.12 Fibre core refractive index variation and resultant wavelength response of fibre Bragg grating.

1.6.   Multiplexing Techniques for optical fibre sensors

In many situations, the decisive reason for using optical sensors is that it is possible to multiplex a set of sensing elements into a single measurement system. The principal techniques will be mentioned here and discussed more fully in subsequent chapters where appropriate.

(i) **Time division**: The sensing elements are deployed along a single or multiple fibre-optic downlead such that when they are illuminated by a pulsed optical source, the returning pulses reach the common detector at distinct times, from which the individual sensor can be identified and information about the measurand recovered. This technique was used to demonstrate the feasibility of the first optical fibre hydrophone array [19], and is discussed in more detail in chapter 6 of this thesis.

(ii) **Wavelength division**: Each sensor contains a spectrally-selective element, such as a FBG, so that the signal from each sensor occupies a unique wavelength range. Thus by wavelength demultiplexing at the detector, the sensors can be identified [27]. This approach is used in this thesis to interrogate an array of FBG's and also an array of erbium-fibre lasers. The fibre lasers are discussed much more extensively in chapter 6 of this thesis.

(iii) **Frequency division**: Heterodyne processing is employed, where each sensor uses a different carrier frequency. Thus demodulation is achieved electronically [20] by having bandpass filters centred around the carrier frequency of each sensor. This approach is discussed more fully in Chapter 6 of this thesis in a review of multiplexing techniques for optical fibre hydrophones.

(iv) **Coherence division**: The sensors are illuminated by a low-coherence source. Each sensor has a different optical path difference (OPD), where all sensor OPD's are greater than the source coherence length, and differ from each other by more than the coherence length. By using a tandem interferometer arrangement and scanning the OPD in the receiving interferometer it is possible to derive sequential interferograms corresponding to each of the sensing interferometers [21].

(v) Spatial Division: In arrays where the optical sensors are distributed along a single fibre the possibility exists of a breakage in the fibre which could render the whole sensor network inoperative. Hence physically separating the sensors onto individual optical fibres can provide protection against fibre breakage and also makes replacement of individual sensors simpler [22].

The ability of optical fibre sensors to be readily multiplexed is illustrated by reference to [22,23]. In [22], a combined time and spatial division multiplexed array of 8 fibre Bragg gratings was constructed, the gratings operating at 830 nm. This array was used to measure both static strain as well as temperature. The experimental arrangement discussed in [22] is complex and will not be reproduced here. Instead results from the sensor array will be quoted to illustrate the measurement abilities of a multiplexed array of FBGs. Table 1.2 below gives the results obtained from [22].

Parameter	Noise Limited resolution (30Hz measurement bandwidth)	Measurement range	Range to resolution ratio
Strain	1.2 microstrain	1.5 millistrain	1250:1
Temperature	0.12 °C	137°C	1142:1

Table 1.2 Measurement range and resolution for a multiplexed array of FBG sensors.

Table 1.2 is not intended to be a definitive summary of the measurement capabilities of FBG sensors. Rather the intention is to provide an illustration of the measurement capabilities of an FBG sensor array by reference to previous research.

Also of interest is the ability to multiplex both interferometric and FBG sensors in the same sensor network. This is illustrated by reference to [23] , where a network of six sensors was interrogated using a frequency division multiplexing technique. Again, the experimental arrangement is complex and will not be reproduced here. Two of the sensors consisted of FBGs (used to measure static strain); one of the sensors was an all-fibre Michelson interferometer and the remaining three sensors were Fabry-Perot cavities. The three F-P cavities and the Michelson interferometer were used to measure

strain. The experimental aim of [23] was to demonstrate that different types of optical sensors could be multiplexed in the same optical network. The experimental results obtained from [23] are summarized in table 1.3 below.

	Fabry-Perot	Michelson Interferometer	FBG
Strain/displacement resolution	0.019 nm	0.019 nm	0.19 μɛ
Strain/displacement range	30 μm	63 μm	6.3 mɛ
Range to resolution	1.5×10^6	3.3×10^6	3.3×10^4

Table 1.3 Results summary for multiplexed array of FBG and interferometric sensors.

As discussed previously, Table 1.3 is not intended to be a definitive summary of the measurement capabilities of multiplexed sensor arrays. Rather the intention is to provide an illustration of the measurement capabilities of multiplexed arrays by reference to previous research. Table 1.3 illustrates that interferometric sensors can measure very small displacements (and strains) and therefore may be of interest in the applications discussed later in this thesis.

1.7   Summary.

The aim of this introductary chapter is to give a brief overview of optical sensing techniques and acoustic sensing as well as to give a summary of the aims of this thesis. The concepts introduced here are expanded on more fully in the following chapter where fibre Bragg gratings and their interaction with an acoustic field are discussed. Also included in the following chapter is a review of the coupling of acoustic waves to optical fibres, with a discussion of other devices which rely on acoustic waves in fibre for their operation. The medical aspects of acoustic sensing are also expanded on, with a discussion of the uncertainties involved in accurate determinations of ultrasonic field parameters.

References :

1. DAKIN, J., CULSHAW, B., 'Optical Fiber Sensors: Principles and Components', Vol. 1, Artech, Boston, 1988.

2. LEFEVRE, H.C.: 'Single-mode fibre fractional wave devices and polarization controllers.' Electronics Letters, 16, 1980, pp. 778 – 786.

3. ANDERSON, D., JONES, J.D.C.: 'Optothermal frequency and power modulation of laser diodes', Journal of Modern Optics, 39, pp 1837-1842, 1992.

4. LEFEVRE, H. 'The Fibre Optic Gyroscope', Artech House, Boston, 1993.

5. SMITH, R. B. 'Fibre optic gyroscopes: a bibliography of published literature', Proc. SPIE, 1585 pp 464-503, 1991.

6. AKHAVAN, L. P., WAYTE, A.P., BERWICK, M., JONES, J.D.C., JACKSON, D.A.: 'A pseudo-reciprocal fibre optic Faraday rotation sensor.', Optics Communications, 59, pp 173-6, 1986.

7. Born, M. and Wolf, E., 'Principles of Optics' (6th ed.), Pergamon, Oxford, 1986.

8. BEARD, P.C. and MILLS, T.N.: 'Extrinsic optical-fiber ultrasound sensor using a thin polymer film as a low-finesse Fabry-Perot interferometer', Applied Optics, Feb. 1996, **35**, No. 4, pp. 663-675.

9. HENDERSON, P. J., RAO Y. J., JACKSON, D. A., ZHANG, L. AND BENNION, I.: 'Simultaneous multi-parameter monitoring using a serial fibre Fabry-Perot array with low coherence and wavelength domain detection', Measurement Science and Technology, 9, pp. 1837-1843, 1998.

10. KERSEY, A.D., JACKSON, D.A. AND CORKE, M.: 'A simple fibre Fabry-Pérot sensor', Optics Communications, 45, pp. 71-73, 1983.

11. BUCARO, J.A., DARDY, H.D., CAROME, E.F.: 'Fibre-optic hydrophone', J. Acoust. Soc. Amer., 1977, **62**, pp. 1302-1304.

12. BOSSELMANN, T., ULRICH, R.: 'High-accuracy position-sensing with fiber-coupled white-light interferometers' 2nd International Conference on Optical Fibre Sensors, Stuttgart, pp. 361-364, 1984.

13. LEFEVRE, H C.: 'White Light Interferometry in Optical Fiber Sensors', 7th International Conference on Optical Fibre Sensors (Institution of Radio and Electronic Engineers, Australia), Sydney, Eds S. Rashleigh, J. Love and S. Poole, pp. 345-351, 1990.

14. RAO, Y.J., JACKSON, D.A.: 'Recent progress in fibre-optic low-coherence interferometry', Measurement Science and Technology, 7, pp 981-999, 1996.

15. FLAVIN, D. A., MCBRIDE, R. AND JONES, J. D. C.: 'Interferometric fibre optic sensing based on modulation of group delay and first order dispersion: application to strain temperature measurand' Journal of Lightwave Technology, 13, pp. 1314-1317, 1995.

16. JACKSON, D.A., PRIEST, R., DANDRIDGE, A., TVETEN, A.B.: 'Elimination of drift in a single-mode optical fibre interferometer using a piezo-electrically stretched coiled fibre', Applied Optics, 19, pp. 2926-2929, 1980.

17. JACKSON, D.A., KERSEY, A.D., CORKE, M., JONES, J.D.C.: 'Pseudo-heterodyne detection scheme for optical interferometers', Electronics Letters, 18, pp. 1081-1083, 1982.

18. DANDRIDGE, A., GOLDBERG, L.: 'Current induced frequency modulation in diode lasers', Electronics Letters, 18, pp. 302-304, 1982.

19. DAKIN, J., WADE, C.A., HENNING, M.L.: 'Novel optical fibre hydrophone array using a single laser source and detector', Electronics Letters, 20, pp. 53-54, 1984.

20. DANDRIDGE, A., TVETEN, A.B., KERSEY, A.D., YUREK, A.M.: 'Multiplexing of interferometric sensors using phase generated carrier techniques', Journal of Lightwave Technology, Vol. LT-5, No. 7, pp. 947-52, 1987.

21. FARAHI, F., NEWSON, T.P., JONES, J.D.C., JACKSON, D.A.: 'Coherence multiplexing of a remote fibre optic Fabry-Perot sensor system', Optics. Communications, 65, pp. 319-21, 1988.

22. RIBEIRO, A.B.L.,   RAO,Y., ZHANG, L., BENNION, I.,   JACKSON, D.A.: 'Time and spatial multiplexing tree topology for fiber-optic Bragg grating sensors with interferometric wavelength shift detection.', Applied Optics, 35, No.13, May 1996, pp 2267-2273.

23. JACKSON, D.A., McGARRITY, C.: 'A Network for large numbers of Interferometric Sensors and Fiber Bragg Gratings with High Resolution and Extended Range', Journal of Lightwave Technolgy, 16, No. 1, Jan. 1998, pp 54-65.

24. BENNION, I., WILLIAMS, J.A.R., ZHANG, L., SUGDEN, K., DORAN, N.J.: 'UV-written in-fibre Bragg gratings', Optical and Quantum Electronics, 1998, **28**, pp. 93-135.

25. ARCHAMBAULT, J-L., REEKIE, L., St. J. RUSSELL, P.: '100% reflectivity Bragg Reflector produced in Optical Fibres by single excimer laser pulses.' Electronics Letters, 4th Mar. 1993, 29, No. 5, pp. 453-455.

26. RAO. Y.: 'Fiber Bragg Grating Sensors: Principles and Applications', in 'Optical Fiber Sensor Technology', 1998, Vol. 2, Chapman and Hall, London.

27. KERSEY, A.D.: 'Interrogation and Multiplexing techniques for Fiber Bragg grating strain sensors', Proc. SPIE, Vol. 2071, pp. 30-48.

Chapter 2

Acoustic and Ultrasonic Sensing Techniques.

2.1 Interaction of an acoustic field with an optical fibre.

The periodic pressure and hence strain variation caused by the propagation of acoustic waves through an optically transparent medium results in changes in the optical properties of the material. The first and most obvious effect is that due to dimensional changes. A physical length change will give rise to changes in the optical path length and hence the optical phase of any light passing through the material will be affected. Another important effect is the photoelastic effect. Mechanical strains in the optical medium, silica in the case of an optical fibre, give rise to changes in the refractive index. This can be expressed mathematically as follows [1], in the compressed notation for isotropic solids.

$$\Delta\left(\frac{1}{n^2}\right)_i = \sum_{i=1}^{6} p_{ij}.\varepsilon_j \tag{2.1}$$

Here n is the refractive index, p_{ij} are the photoelastic or Pockels coefficients and ε_j are the strains in the material. For anisotropic or crystalline materials, the photoelastic coefficients take the form of a 4th rank tensor with 81 components. For isotropic materials such as silica, the analysis is considerably simplified, and the 4th rank tensor reduces to 2 independent coefficients. A secondary effect of the strain-induced change in refractive index is to alter the fibre birefringence. At low acoustic frequencies where the acoustic wavelength is significantly greater than the fibre diameter, the induced strains in the fibre are uniform across the fibre cross-section, and the birefringence is unaffected. However, as the acoustic frequency increases and the wavelength approaches or becomes less than the fibre diameter, the strains induced in the fibre will become increasingly anisotropic [1]. The anisotropic strain field gives rise to anisotropic changes in the core refractive index. Hence the two orthogonally polarized

nearly degenerate HE_{11} eigenmodes of the fibre experience different phase shifts and the polarization state of the light travelling down the fibre core is affected. This effect has been successfully exploited in the construction of a distributed ultrasonic optical fibre sensor [2,3] for frequencies ranging from a few hundred kHz up to several tens of MHz, and is also exploited in the construction of acousto-optic fibre frequency shifters, which are discussed shortly.

A third effect occurs when the material is in the form of a waveguide, the most obvious example of this being an optical fibre. Changes in the fibre core cross-sectional area have an effect on the waveguide propagation constant β and hence the phase of the optical signal. It can be shown [4] that this effect is negligible by comparison with the dimensional and photoelastic changes and will be ignored in any subsequent analysis. For a fibre of length l, the optical phase delay ϕ relative to free space propagation is given by :-

$$\phi = \omega \, l/v \tag{2.2}$$

where ω is the optical frequency and v is the optical phase velocity in the fibre. When v and l are changed, the corresponding fractional change in phase along the fibre is given by :-

$$(\Delta\phi)/\phi = [(\Delta l)/l] - [(\Delta v)/v] = \varepsilon_z + (\Delta n)/n \tag{2.3}$$

It can be shown [4] that for a fibre subjected to axial strain ε_z and radial strain ε_r $(= \varepsilon_x = \varepsilon_y = \Delta r/r)$, where r is the fibre radius, the magnitude of the relative optical phase shift is given by :-

$$\frac{\Delta\phi}{\phi} = \varepsilon_z - \frac{n^2}{2}[(p_{11} + p_{12})\varepsilon_r + p_{12}\varepsilon_z] \tag{2.4}$$

where p_{11}, p_{12} are the Pockel's coefficients for silica. The analysis given previously is extended later in this chapter where a description of the interaction of a FBG with a time-varying pressure field is given. It is also useful to discuss the interaction of other devices with acoustic fields. One particular type of device that relies on the interaction of an acoustic wave with an optical fibre is an acousto-optic fibre frequency shifter and it it this type of device that is discussed next.

2.1.1   Acousto-optic frequency shifters.

The main elements of a acousto-optic fibre frequency shifter are an optical fibre which in its unperturbed state supports two initially orthogonal optical modes and a means of inducing a travelling perturbation in the fibre in such a way that in the perturbed state optical power can be efficiently transferred between the modes. The travelling perturbation is an acoustic wave generated on the free fibre by an ultrasonic transducer as shown in fig 2.1, taken from [5]. Travelling acoustic waves on a fibre (or rod) broadly fall into three categories : longitudinal, flexural and torsional. In the case of figure 2.1, a travelling wave was acoustically induced on the fibre which effectively gave rise to coupling between the previously orthogonal fibre modes.
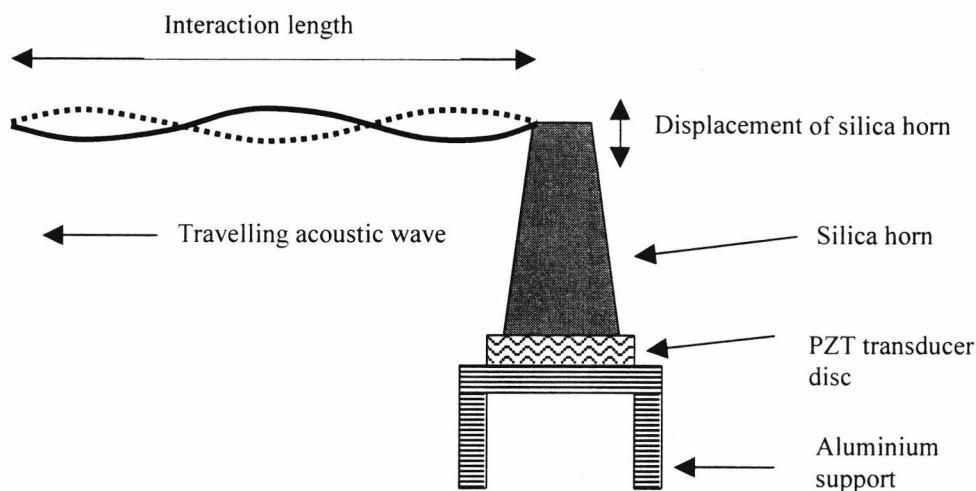
Figure 2.1 – Acoustically induced travelling wave in optical fibre.

The fibre used in the experiment of [5] was a highly birefringent fibre. Acoustic excitation was provided by a disc composed of the piezoelectric material lead zirconate titanate (PZT). The acoustic energy from the transducer was transmitted to the fibre by a silica horn which also served to mechanically increase the acoustic excitation amplitude. In figure 2.1, the maximum coupling between the orthogonal optical modes occurs when the spatial period of the acoustically-induced fibre perturbation matches the beat length between the modes. The net result of the travelling perturbation in the

fibre is to cause a frequency shift in the light coupled between the modes. This can be expressed as, from [5]:-

$$\Delta\omega = \omega_2 - \omega_1 = \Omega(\beta_2 - \beta_1) \tag{2.5}$$

where $\omega 1$, $\omega 2$ are the optical frequencies associated with each fibre mode, Ω is the angular frequency of the acoustic perturbation and β_1, β_2 are the fibre mode propagation constants. Altering the acoustic drive frequency allowed the mode coupling to be optimised by ensuring that the acoustic wavelength matched the fibre mode-mode beat length. This was found to occur at approximately 3.2 MHz, hence giving rise to an optical frequency shift at this frequency. As the acoustically-induced stress distribution travels along the fibre the phase of the coupled light is advanced or retarded depending on whether it was initially on the fast or slow axis of the fibre and also depending on the relative directions of optical and acoustic propagation. The proportion of the initial optical power that is frequency shifted depends on the interaction length and also on the acoustic amplitude. An important prerequisite for effective mode-mode coupling due to the travelling acoustic wave is that there must be some degree of intrinsic fibre birefringence. If this were not the case then there would be no effective coupling, as there needs to be birefringence present in the fibre for this effect to occur. This phenomenon has also been demonstrated in single mode fibre [6]. Here bend-induced birefringence in ordinary single-mode fibre was induced by coiling the fibre around a hollow aluminium cylinder, the cylinder being acoustically excited by a piezoelectric transducer on the top of the cylinder. Linearly polarised light launched into one of the fibre axes was acoustically coupled into the orthogonal axis and frequency shifted. These devices can also function as tunable filters, switches and modulators. When they are used as single-sideband frequency shifters, mode convertors and filters are necessary to separate the residual carrier from the shifted signal and give a single-mode output.

The acoustic interaction length of fibre used in the experiment shown in figure 2.1 was approximately 600 mm stripped of its plastic buffer coating, bounded by lengths of unstripped fibre. The lengths of unstripped fibre bounding the acoustic interaction length were found to act as acoustic absorbers. This suggests that any form of

discontinuity in the fibre or will serve to suppress the travelling acoustic waves and that simply having some form of coating on the fibre will function as an acoustic absorber. This observation is of use later in Chapter 4 when suppression of travelling acoustic waves in the fibre is discussed with regard to using fibre Bragg gratings as acoustic sensors. As FBGs are investigated in this thesis with an aim towards constructing a practical ultrasonic sensor it is worth describing their manufacture and properties in some detail, as well as their interaction with a time-varying pressure field.

2.2   Fibre Bragg Gratings.

Fibre Bragg Gratings (FBGs) take the form of a periodic refractive index modulation in the core of an optical fibre. The first gratings were formed by the standing-wave interference pattern generated by an argon-ion laser in the germanosilicate core of a telecommunications fibre [7]. Permanent, very narrowband Bragg reflection gratings of around 1m in length were formed after several minutes exposure. Although this excited significant interest at the time, little further research was performed until it was reported by Meltz *et al.* [8] in 1989 that gratings could be written by two-beam holographic exposure through the side of a standard telecommunications fibre using UV radiation from a pulsed excimer laser. This had significant advantages over the previous work in that the writing efficiency was substantially enhanced due to the use of a shorter wavelength and that the grating reflection wavelength could be chosen by simply altering the angle between the incident beams. Alternatively a silica phase mask can be used. These two methods of grating fabrication are described briefly later in this chapter. However, it is worth noting that not all photosensitive fibres are doped with germanium oxide. Even though photosensitivity was first observed in germania core fibres by Hill *et al*, it has been demonstrated that FBG's can be successfully fabricated in, for example, polymer fibres [9] and also phosphosilicate fibres [10], demonstrating that the presence of germania is not an essential prerequisite for photosensitivity (and FBG formation). The physical mechanisms of photosensitivity in both germania-doped and non germania-doped fibres are complex [11,12] and will not be discussed further in this thesis. However, most models proposed [13] in order to explain fibre photosensitivity are based on the types of UV absorbing defects which exist in germanosilicate glass.

2.2.1   Manufacture and Properties of Fibre Bragg Gratings.

Figure 2.2 depicts the inscription of a FBG into the core of a germanosilicate core fibre by transverse two-beam interference. The grating is photoinduced as a spatial modulation in the density and hence refractive index with a period of $\Lambda = \lambda_{UV} / 2\sin(\theta / 2)$, where θ, λ are as shown. The refractive index profile along the longitudinal (z) axis of the fibre is given by :

$$n(z) = n_{core} + \delta n\left[1 + \cos\left(\frac{2\pi z}{\Lambda}\right)\right] \tag{2.6}$$

where n_{core} is the refractive index of the fibre core, δn is the amplitude of the refractive index modulation and Λ is the perturbation period. The grating peak wavelength reflectivity λ_B is given by the Bragg condition, and is $\lambda_B = 2n\Lambda$.

$$\Lambda = \lambda_{UV} / 2\sin(\theta / 2)$$
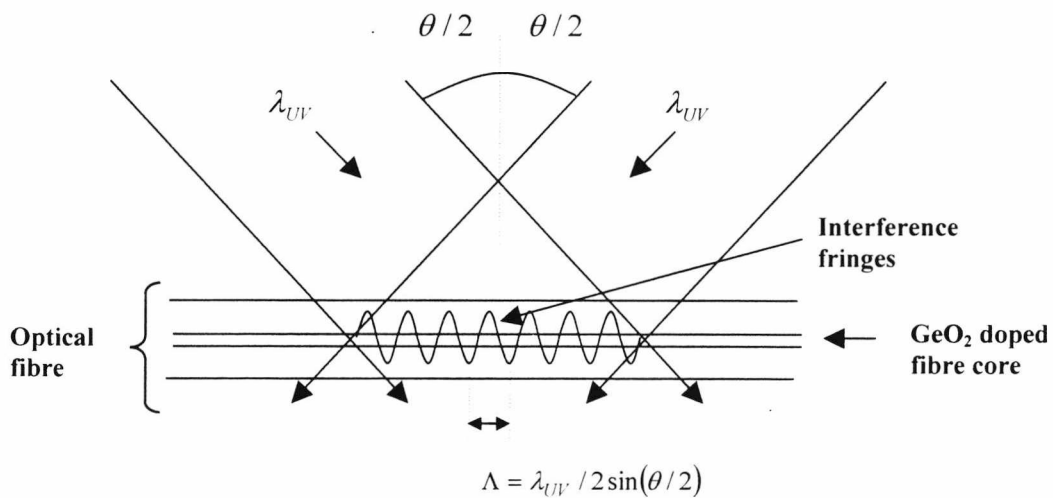
Figure 2.2 – Inscription of a periodic grating in the core of a photosensitive germanosilicate optical fibre by two interfering UV beams of wavelength λ_{UV}.

The phase mask technique [14] for writing FBGs is shown in figure 2.3. The phase mask consists of a one-dimensional surface relief pattern of period Λ_{PM} chemically etched

into a fused silica substrate, with the depth of the corrugations being $d = \lambda_{UV} / 2(n_{s(UV)} - 1)$, where $n_{s(UV)}$ is the refractive index of the fibre core at λ_{UV}. The grating is written with a period $\Lambda = \Lambda_{PM} / 2$ by the interference between the +1 and −1 diffracted orders of the phase mask. The main disadvantage of this technique is that a separate phase mask is needed for each of the desired FBG wavelengths. However this is offset by the high degree of reproducibility of the gratings. Some degree of control over the grating wavelength is also available by stretching the grating during the writing process. When the fibre tension is relaxed following exposure, the induced periodic refractive index variation compresses and alters the peak wavelength. This concludes the overview of the structure and manufacture of FBGs.
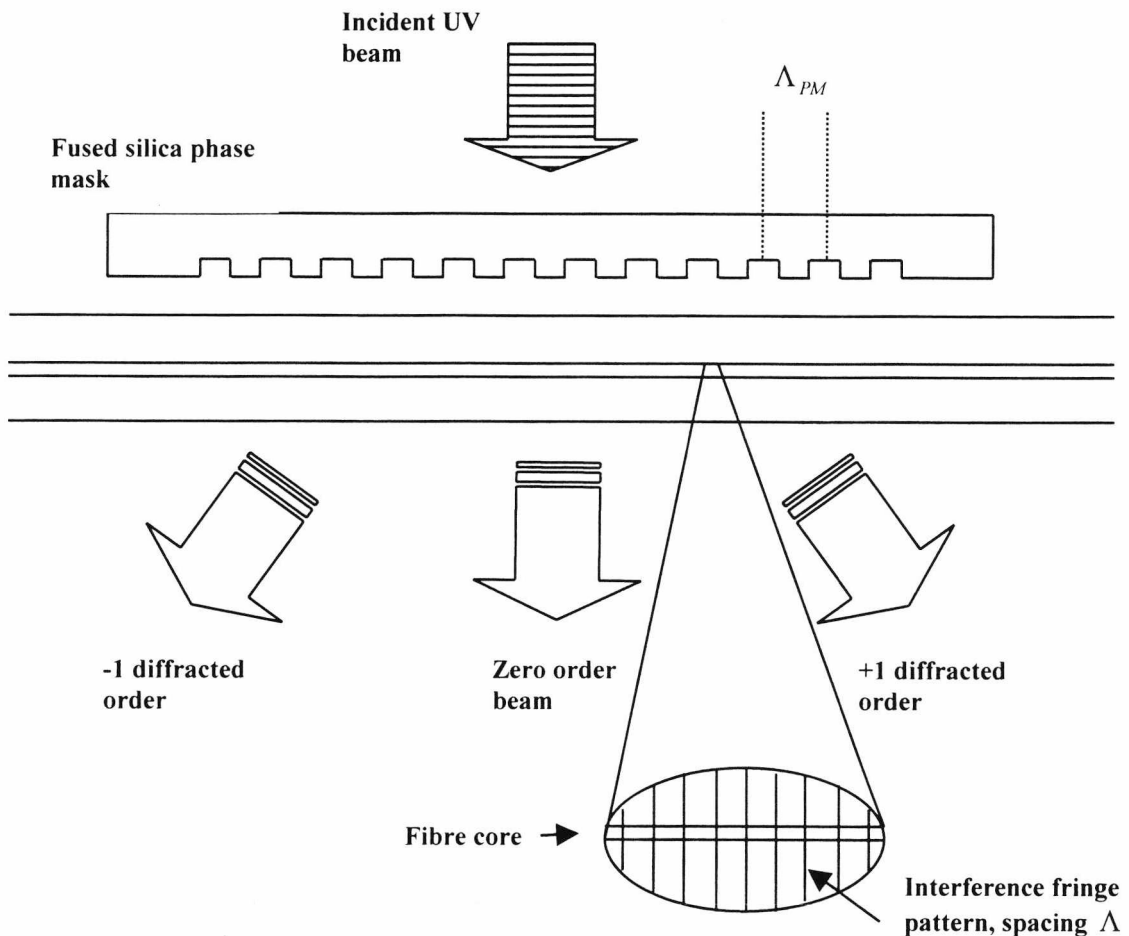
Figure 2.3 – FBG inscription by UV exposure through a silica phase mask.

2.2.2 Mathematical Description of a FBG.

In order to usefully describe the wavelength response of a FBG and its subsequent variation as a function of external factors some degree of mathematical modelling is called for. The most commonly used technique for modelling the grating response is based on coupled mode theory. This model uses a pair of first–order differential equations to describe the amplitudes of the incident and reflected travelling modes in the fibre core. The FBG provides a coupling mechanism between the two modes so that energy can be transferred from the incident to the reflected mode. The full solution of these equations is well documented elsewhere [15,16] and will not be attempted here as it is not strictly relevant to the aims of this thesis. Instead, important derivations will be quoted and referenced in order to elucidate points of interest and relevance to the experimental results. The following important results arise from the solution to the coupled-mode equations. The grating reflectance $R(L, \lambda)$ as a function of grating length and wavelength is given by :

$$R(L, \lambda) = \frac{\kappa^2 \sinh^2(SL)}{\delta\beta^2 \sinh^2(SL) + S^2 \cosh^2(SL)} \qquad \text{for } \kappa^2 > \delta\beta^2 \qquad (2.7)$$

$$R(L, \lambda) = \frac{\kappa^2 \sin^2(QL)}{\delta\beta^2 + \kappa^2 \cos^2(QL)} \qquad \text{for } \kappa^2 < \delta\beta^2 \qquad (2.8)$$

where L is the grating length, κ is the mode coupling coefficient, $\beta = n_{eff} / \lambda$ is the mode propagation constant, n_{eff} is the effective refractive index, $\delta\beta = \beta - (\pi p / \Lambda)$, $S = (\kappa^2 - \delta\beta^2)^{1/2}$ and $Q = (\delta\beta^2 - \kappa^2)^{1/2} = iS$. The maximum grating reflectivity is given when $\delta\beta = \beta - (\pi p / \Lambda) = 0$, i.e when the Bragg condition is met, namely $p\lambda = 2n_{eff} \Lambda \equiv \lambda_B$, where $p = 1$ for the fundamental Bragg order. In this case, equation 2.2 is considerably simplified and the peak reflectivity R_{max} is given by :

$$R_{max} = \tanh^2(\kappa L) \qquad (2.9)$$

Equation 2.9 gives $R_{max} \approx 58\%$ for $\kappa L = 1$, 93% for $\kappa L = 2$ and 99% for $\kappa L = 3$. An approximate expression for the Full Width Half Maximum (FWHM) bandwidth is given by:

$$\Delta\lambda_{FWHM} \approx \lambda_B s \left[\left(\frac{\delta n}{2 n_{core}} \right)^2 + \left(\frac{\Lambda}{L} \right)^2 \right]^{\frac{1}{2}} \tag{2.10}$$

where $s \approx 1$ for strong gratings with near 100% reflectivity, and $s \approx 0.5$ for weak gratings. The coupling constant κ is proportional to the depth of the refractive index modulation, and is given by :

$$\kappa = \frac{\pi \delta n}{\lambda_B} \eta \tag{2.11}$$

where η is the fraction of the fibre mode power contained within the fibre core. Assuming that the grating is uniformly written throughout the core, η can be approximated by $\eta \approx 1 - V^{-2}$, where V is the V value of the fibre and for a single mode fibre is given by the first zero of the first-order Bessel function, approximately equal to 2.405. The following section describes the response of a FBG to an external pressure field, for both static and time-varying pressures.

2.2.3   Wavelength response of a FBG to external factors.

2.2.3.1   FBG wavelength-pressure response.

As one of the aims of this thesis is to explore the response of a FBG to a time varying pressure field some analysis of the FBG is required. This analysis is based on the methods of [4]. A pressure change ΔP on the fibre will give rise to a refractive index change via the photoelastic effect and both axial and radial dimensional changes. This can be expressed as follows for a FBG of peak wavelength reflectivity λ_{FBG} and periodicity Λ in a fibre core of refractive index n subject to an isotropic pressure field P:

$$\frac{\Delta\lambda_{FBG}}{\lambda_{FBG}} = \frac{\Delta(n\Lambda)}{n\Lambda} = \left[\frac{1}{\Lambda} \frac{\partial\Lambda}{\partial P} + \frac{1}{n} \frac{\partial n}{\partial P} \right] \Delta P \tag{2.12}$$

Given a strain ε and a corresponding stress σ, it is useful to first calculate the pressure sensitivity of a bare optical fibre length L, core diameter D, refractive index n, Young's modulus E and Poisson's ratio μ in an isotropic pressure field P. As the field is isotropic there are no shear components and the stress σ and strain ε can be written as three component vectors.

$$\sigma = \begin{bmatrix} -P \\ -P \\ -P \end{bmatrix} \qquad \varepsilon = \begin{bmatrix} \varepsilon_x \\ \varepsilon_y \\ \varepsilon_z \end{bmatrix} = \begin{bmatrix} -P(1-2\mu)/E \\ -P(1-2\mu)/E \\ -P(1-2\mu)/E \end{bmatrix} \qquad (2.13)$$

Assume that light with a free-space propagation constant k_0 is propagating through the fibre as a single mode with a propagation constant β. The phase of the light after going through the fibre section length L is therefore $\phi = \beta L$. Straining the fibre will cause the phase at the fibre output to shift by:

$$\Delta\phi = \beta\Delta L + L\Delta\beta \qquad (2.14)$$

The first term in equation 2.14 above represents the effects of the physical length change. This can be written as :

$$\beta\Delta L = \beta\varepsilon_z L = -\beta(1-2\mu)LP/E \qquad (2.15)$$

The second term in 2.14 effectively has two separate components. The first is the strain-optic effect whereby the strain changes the refractive index of the fibre core. The second component is due to the change in the fibre diameter due to the applied strain. This can be expressed as follows:

$$L\Delta\beta = L\frac{\partial\beta}{\partial n}\Delta n + L\frac{\partial\beta}{\partial D}\Delta D \qquad (2.16)$$

The value of β can be written as $n_{eff}k_0$, where the effective refractive index n_{eff} lies between the core and clad refractive indices. Since these indices differ by of the order of 1% a good approximation is $\beta = n_{eff}k_0$. Therefore:

$$\partial\beta/\partial n = k_0 \qquad (2.17)$$

The strain-optic effect appears as a change in the optical indicatrix i.e.

$$\Delta\left(\frac{1}{n^2}\right)_i = \sum_{j=1}^{6} p_{ij}\varepsilon_j \qquad (2.18)$$

With no shear strain $\varepsilon_4 = \varepsilon_5 = \varepsilon_6 = 0$. Hence only the $i,j=1,2,3$ elements of the strain-optic tensor for a homogeneous isotropic material need be considered. Hence:

$$P_{ij} = \begin{bmatrix} p_{11} & p_{12} & p_{12} \\ p_{12} & p_{11} & p_{12} \\ p_{12} & p_{12} & p_{11} \end{bmatrix} \qquad (2.19)$$

The change in the optical indicatrix is therefore given by:

$$\Delta\left(\frac{1}{n^2}\right)_{x,y,z} = -p_{11}P(1-2\mu)/E - 2p_{12}P(1-2\mu)/E \qquad (2.20)$$
$$= -(P/E)(1-2\mu)(p_{11}+2p_{12})$$

Light propagating in the z-direction along the fibre axis sees a change in index of :

$$\Delta n = -\frac{1}{2}n^3(P/E)(1-2\mu)(2p_{12}+p_{11}) \qquad (2.21)$$

The last term in equation 2.16 represents the change in the waveguide mode propagation constant due to a change in fibre diameter. The derivation of the magnitude of this effect is lengthy and can be found in [4]. However, this effect is negligible by comparison with the length changes and the changes due to the photoelastic effect and can be neglected. Combining the previous derivations gives the following results for the changes in physical length and the refractive index.

$$\frac{\Delta L}{L} = -\frac{(1-2\mu)P}{E} \qquad (2.22)$$

$$\frac{\Delta n}{n} = n^2\frac{P}{2E}(1-2\mu)(2p_{12}+p_{11}) \qquad (2.23)$$

As a result of $\Delta L/L = \Delta\Lambda/\Lambda$, the terms for the periodicity-pressure and index-pressure variation can be written as:

$$\frac{1}{\Lambda}\frac{\partial\Lambda}{\partial P} = -\frac{(1-2\mu)}{E} \tag{2.24}$$

and

$$\frac{1}{n}\frac{\partial n}{\partial P} = \frac{n^2}{2E}(1-2\mu)(2p_{12} + p_{11}) \tag{2.25}$$

Hence the wavelength-pressure sensitivity for the FBG is given by :

$$\Delta\lambda_B = \lambda_B\left[-\frac{(1-2\mu)}{E} + \frac{n^2}{2E}(1-2\mu)(2p_{12} + p_{11})\right]\Delta P \tag{2.26}$$

For time-varying pressures where the acoustic wavelength is significantly greater than the fibre diameter the FBG response will be given by (2.26) multiplied by a time-dependent term of the form $\sin(\omega_A t)$, where ω_A is the acoustic frequency. The acoustic wavelength is important in that for large wavelengths the acoustic pressure gradient across the fibre diameter is small and the fibre can be assumed to be subjected to a uniform hydrostatic pressure field. When the acoustic wavelength is comparable to the fibre diameter significant pressure gradients will exist across the fibre diameter which can significantly affect the fibre response [1]. In this thesis the maximum acoustic frequency examined was 1.911 MHz, corresponding to an acoustic wavelength of 0.75 mm (in water). Hence the acoustic wavelength is still significantly greater than the fibre diameter. The inertial behaviour of the fibre is also important. At lower frequencies, the fibre behaves in an unconstrained manner and both the length and pressure-induced photoelastic changes are significant. However, as the acoustic frequency increases towards the MHz region, the fibre inertial response becomes increasingly constrained, as the inertia of the fibre itself prevents the fibre from undergoing longitudinal changes at the acoustic excitation frequency. Hence the term given by equation (2.22) becomes less significant with increasing frequency and the photoelastic term given in equation

(2.23) becomes   predominant. Therefore for high (~MHz) excitation frequencies the FBG wavelength response will be approximated by equation (2.27).

$$\Delta \lambda_B \approx \lambda_B \left[\frac{n^2}{2E} (1 - 2\mu)(2p_{12} + p_{11}) \right] \Delta P \sin(\omega_A t) \tag{2.27}$$

2.2.3.2   FBG wavelength-strain response.

The wavelength shift $\Delta \lambda_{BS}$ for an applied longitudinal strain $\Delta \varepsilon$ is given by :

$$\Delta \lambda_{BS} = \lambda_B (1 - \rho_\alpha) \Delta \varepsilon \tag{2.28}$$

where ρ_α is the photoelastic coefficient of the fibre, derived previously in the wavelength-pressure analysis for a FBG.

2.2.3.3   FBG wavelength-temperature response.

For a temperature change of ΔT , the wavelength shift $\Delta \lambda_{BT}$ is given by :

$$\Delta \lambda_{BT} = \lambda_B (1 + \xi) \Delta T \tag{2.29}$$

where ξ is the fibre thermo-optic coefficient. Table 2.1 below summarises the strain, temperature and pressure sensitivities of FBGs with different wavelengths [17].

FBG Wavelength (nm)	Strain Sensitivity, pm/µε	Temp. sensitivity, pm/°C	Pressure sensitivity, nm/Pa
830	~0.64	~6.8	-1.93×10^{-9}
1300	~1.00	~10	-3.02×10^{-9}
1550	~1.20	~13	-3.60×10^{-9}

Table 2.1 Strain, temperature and pressure sensitivity of FBG sensors with different wavelengths.

This concludes the discussion of the properties of FBGs. The next section provides a summary of currently available medical ultrasonic detectors.

2.3 Medical Aspects of Ultrasonic Sensing.

Determination of the FBG response and sensitivity to the periodic strain induced by an ultrasonic field potentially provides an effective in-vivo means of assessing the acoustic field strength (and temperature) during certain therapeutic applications of ultrasound. These applications take several forms; one important technique involves the application of a high-power (several watts or tens of watts) of focussed ultrasonic energy to the treatment of surgically intractable tumours. The high intensity of the focussed beam gives rise to heating effects and can kill malignant tissue if the heating is sufficiently prolonged. Pulsed ultrasonic beams from a lithotripter [18] can be used to shatter kidney and bladder stones without the need for potentially invasive surgical techniques and their associated risks. Areas of uncertainty in the above therapies are the exact acoustic pressure exerted by the action of the ultrasonic field on both the diseased and surrounding healthy tissues, as well as the tissue temperatures. Often the spatial distribution of the ultrasonic field in the body is based on theoretical models of some complexity, which coupled with the heterogeneous nature of tissues may give rise to significant uncertainties in the efficacy of the treatment as well as its safety [19]. Reliable in-vivo determination of the beam profile is important from the obvious point of view of focussing the beam exclusively on diseased instead of healthy tissue. Measurement of the transducer efficiency is required for determination of the ultrasound exposure rate and hence the induced tissue temperature rise [19]. Accurate beam profile measurements are needed to enable correct focussing of the ultrasonic beam. Current measurement techniques are electrical in nature, involving the use of either piezoelectric polymers or ceramics [20] to give useful information about the acoustic field strength. Alternatively, thermistors coated with acoustically absorbing materials have been used to measure both temperature and the acoustic field strength using the rate of temperature rise [21]. The disadvantages of electrically based measurement techniques are the inherent susceptibility to damage by the high acoustic pressures generated at the focal point, as well as lack of immunity to electrical pickup from the transducer driver. The smallest element size available in PVDF hydrophones is around 0.5 mm for a needle hydrophone [20], which may limit the ability of the sensor to resolve highly focussed beams. A number of fibre-optic hydrophones have

been constructed for medical applications. These are discussed later in this chapter where results for the pressure sensitivity are given and compared with that of a typical piezoelectric PVDF hydrophone.

2.3.1   Sensors currently used in Medical Applications.

Sensors currently used in therapeutic medical applications consist of piezoelectric materials, either in the form of a ceramic such as lead zirconate titanate (PZT), or more commonly in the form of a piezoelectric polymer such as polyvinylidene difluoride (PVDF), the latter offering a superior acoustic impedance match to water (biological tissues being ~70% water, except for bone) and hence an increased sensitivity. However, calibrated sensors based on these materials suffer from a number of disadvantages. Being composed of either a polymer or a ceramic they are therefore susceptible to mechanical damage in a high power ultrasonic beam, as well as having dimensions comparable to or greater than the acoustic wavelength. The sensor size is important in terms of minimising the perturbation of the beam and the measurement uncertainties arising from this. A large sensor can also give rise to heating effects caused by acoustic absorbtion in the sensor itself, which can obviously invalidate any temperature readings.   Also, being electrically based, it is difficult to shield the sensor from spurious pickup, which again creates measurement uncertainties. The magnitude of these uncertainties is illustrated in [22], where different measurements of the same ultrasonic transducer were performed by separate research groups using different forms of ultrasonic detector. A discussion of this study is given overleaf.

Knowledge of the acoustic output parameters of medical diagnostic ultrasound equipment is of basic importance for the safety of the patient. Over the years, an appropriate and generally accepted basis has been developed for common acoustic output measurements. Such measurements are performed in water, and PVDF hydrophones are mainly used as the basic measurement tools. The quantities generally considered to be most important are:-

- The time-averaged ultrasonic power,
- The time-averaged ultrasonic intensity, which is the power divided by the beam cross-sectional area.
- The positive and negative peak value of the acoustic pressure in the ultrasonic field.

Reference [22] gives details of an inter-comparison between measurements obtained using different types of hydrophone to illustrate that even for a fixed hydrophone output power there are still significant differences between different ultrasonic measurement techniques. The results of this comparison study are summarized here to illustrate the degree of variability that exists even in widely accepted methods of measuring the parameters of ultrasonic transducers. Measurements were performed by different investigators at different laboratories with the same ultrasonic transducer but with different measuring devices, consisting mainly of PVDF film hydrophones. Details of the measurement instruments are given below. Measurement 2 is of interest as this was performed with a fibre-optic probe hydrophone which will be discussed later in this chapter.

Measurement 1.
The hydrophone measurements alternately involved two PVDF hydrophones of 25 mm foil thickness; a membrane-type (GEC-Marconi coplanar Y-33-7603) and a needle-type hydrophone, both 0.5 mm in diameter.

Measurement 2.
All quantities were measured using the fiberoptic probe hydrophone developed in [23].

Measurement 3.

The hydrophone was a 0.6 mm diameter, 28 µm film thickness PVDF needle type.

Measurement 4.

All quantities were measured using a bilaminar GEC-Marconi membrane hydrophone of type Y-34-3598, (as used in experimental measurements in later chapters). This hydrophone has a 25 µm PVDF film thickness and 0.5 mm diameter sensitive area.

Measurement 5.

All quantities were measured using a PVDF needle-type hydrophone 0.4 mm in diameter with a 9-µm film thickness.

Measurement 6.

The hydrophone measurements alternately involved two needle-type hydrophones, the first 0.6 mm in diameter and with 28-µm PVDF film thickness, the second being 0.15 mm in diameter and with 9-µm PVDF thickness.

Measurement 7.

Measurements were carried out using a 0.2-mm square spot, 25-µm thickness PVDF hydrophone. The output beam area was determined with a needle hydrophone 0.6 mm in diameter, 28-µm PVDF film thickness.

Measurement 8.

The hydrophone consisted of a PVDF element with a thickness of 6 µm and a diameter of 0.5 mm. The active element was glued on a brass backing and mounted in the center of a cone made of epoxy.

The results from these separate measurements are tabulated overleaf in table 2.2.

Measurement	Power (mW)	Pressure (Mpa)	Average Intensity (mW/cm2	Average Peak Intensity (mW/cm2)	Measured Frequency (MHz)
1	5.9 ± 0.3	1.69 ± 0.20	7.8 ± 1.6	79 ± 16	3.30 ± 0.1
2	9.0 ± 2.5	2.20 ± 0.15	12.5 ± 4.5	125 ± 20	3.30 ± 0.1
3	5.7 ± 1.3	1.50 ± 0.20	7.3 ± 1.7	74 ± 10	3.27 ± 0.06
4	5.3 ± 1.0	1.78 ± 0.18	8.4 ± 1.8	90 ± 14	3.29 ± 0.03
5	3.8 ± 1.4	1.53 ± 0.27	7.6 ± 3.4	72 ± 27	3.31 ± 0.3
6	6.0 ± 0.5	1.68 ± 0.19	7.6 ± 1.6	92 ± 26	3.33 ± 0.07
7	5.7 ± 0.4	1.94 ± 0.10	11.3 ± 1.0	93 ± 8	3.30 ± 0.1
8	5.9 ± 0.2	2.86 ± 0.48	13.2 ± 1.9	176 ± 60	3.27 ± 0.2
Mean	5.84	1.84	9.61	92.5	3.30

Table 2.2   Results of comparison study for separate measurements on the same ultrasonic transducer.

Eight separate and independent measurements were obtained by different investigators of the main parameters of interest of a 3.5-MHz diagnostic imaging medical ultrasonic transducer in water at room temperature. The majority of results turned out to agree with one another within the estimated measurement uncertainties, which were roughly of the order of ± 10% to ± 30% from [22]. The intercomparison study demonstrates that correct ultrasonic measurements are subject to a high degree of variability even when measuring the same ultrasonic transducer. In addition, it should be noted that a relatively low-intensity field in the low megahertz range was involved here and that high-frequency or strongly shocked (such as from a lithotripter) fields can be much more difficult to measure accurately.

2.4   Potential advantages of a FBG ultrasonic sensor.

The development of a small, flexible, quasi-distributed sensor based purely on optical techniques could potentially allow a more accurate determination of therapeutic parameters of interest, namely ultrasonic field intensity, and temperature, which currently available hydrophones are unable to measure. A sensor based on FBG's would have the following advantages:-

- The sensor dimensions could, with suitable engineering, be less than the acoustic wavelength. The importance of this is discussed in [24], where it is shown that probes with a diameter comparable to the acoustic wavelength cause significant distortions of the ultrasonic field and hence give rise to measurement errors. A small sensor would also be minimally invasive in terms of being introduced into the body, hence minimising the risk of any surgical trauma.

- The purely optical nature of the sensor would avoid any problems of electrical pickup and interference, giving more accurate measurements and hence maximising the therapeutic effectiveness.

- The wavelength selectivity of a FBG allows several sensors to be integrated on the same length of optical fibre, allowing a quasi-distributed sensor array to be constructed using wavelength division multiplexing (WDM) techniques [25] This would allow more accurate determination of the field profile. Multiplexing an array of electrically based sensors creates problems of sensor cross-talk and also gives a bigger sensor.

- The effects of temperature and the ultrasonic field on the FBG occupy different frequency regimes; temperature effects of the order of a few Hz, dynamic ultrasonically-induced strains of the order of several MHz. Hence the two effects can, in principle, be measured simultaneously by the same sensor or sensor array.

Chapter 4 of this thesis is devoted to exploring the potential of in-fibre Bragg gratings as ultrasonic sensors. As described previously, the FBG consists of a periodic variation of the core refractive index, giving rise to a narrow bandwidth reflective device. Ultrasonically (or temperature) induced strains in the FBG are transduced into a wavelength shift as the period of the refractive index variation is changed. This encoding of the measurand into a wavelength shift allows absolute strain measurements to be performed using low-coherence interrogation techniques. The length of the FBG can be from several cm down to submillimetre size, ideally a few mm or less for a minimally invasive sensor. The FBG wavelength selectivity has obvious implications

for constructing a quasi-distributed sensor array using wavelength-division multiplexing techniques. This approach is examined in chapter 4 in an attempt to construct a quasi-distributed sensor for in-vivo medical sensing.

2.5   Other optically-based medical ultrasound sensors.

2.5.1   Low-Finesse Optical Cavities.

The applicability of low-finesse optical cavities as acoustic sensors is also investigated in this thesis. Cavities based on the interaction of a thin ($\sim$50 μm) polymer film with an ultrasonic field provide a promising route towards constructing a sensitive point acoustic sensor with a number of potential medical and engineering applications [26]. The acoustic field causes changes in the cavity length and hence the cavity transfer function is affected. This change in transfer function can then be examined interferometrically to determine the acoustic field parameters. Careful consideration of the materials used in constructing the cavity can give rise to significant enhancement in acoustic detection sensitivity for extrinsic (external to the fibre) cavity sensors. As with the FBG based sensor, interrogation of these sensors can be based on low-coherence interferometric techniques. Previous research into the use of a low-finesse optical cavity is discussed more extensively in Chapter 5, where experimental results from the low-coherence interrogation of a low finesse cavity are compared and contrasted with the results of a previous study as well as with the results of the FBG investigations of chapter 4. The results from this previous study of low-finesse cavities as ultrasound sensors is summarised in table 2.3, along with the results from fibre-tip based optical hydrophones which are discussed next.

2.5.2   Fibre tip based optical hydrophones.

In this approach the hydrophone consists of a cleaved fibre tip which is coated with one or several hard dielectric optical layers of alternating refractive indexes. If an ultrasonic wave is incident on the fibre tip the coating is deformed and the thickness and the refractive index of the optical layers is changed by the photoelastic effect, resulting in a modification to the backreflected intensity from the dielectric layers. A secondary effect arises from the change in reflectivity at the fluid/sensor interface, where the ultrasonic pressure changes the refractive index of the fluid in front of the sensor. This approach of using a bare uncoated fibre tip has been investigated in [23, 27]. Here the sensor relies for its operation purely on the change in reflectivity at the fluid/sensor interface, where the ultrasonic pressure changes the refractive index of the fluid in front of the sensor. The construction of a multilayer sensor [28] is illustrated below in figure 2.4, and is an extension of the simple uncoated fibre tip approach described in [23,27].
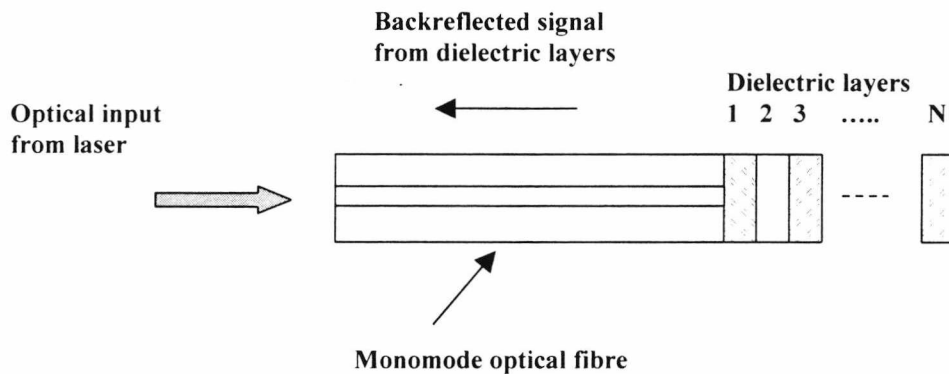
Figure 2.4   Dielectric fibre-tip medical ultrasonic sensor.

This approach has been investigated in [28], where 15 alternating layers of Nb_2O_5 (refractive index $n = 2.3$) and SiO_2 ($n = 1.48$) were sputtered onto the end of a cleaved optical fibre. The sensor was interrogated simply by using a HeNe laser of ~12mW optical power. The backreflected intensity from the dielectric layers was incident on a photodetector and the resultant ultrasonically induced changes in optical intensity were measured. The experimental aims of [28] were to investigate the ability of a multilayer dielectric sensor to measure the high-intensity shock waves generated by a lithotripter.

A lithotripter is a device designed to produce an ultrasonic shock wave of the order of several 10's of Mpa. No attempt was made in [28] to assess the feasibility of using the multilayer hydrophone to determine the acoustic field parameters of a typical medical ultrasonic transducer. This is because the sensor has a relatively low pressure detection sensitivity, with a minimum detectable ultrasonic pressure of the order of 10kPa. This low sensitivity is due to the high Young's modulus of the dielectric layers, which makes the dielectric film layer resistant to any pressure-induced changes in their optical properties. However, the results of [23] suggest that a fibre tip hydrophone is able to provide useful measurements of ultrasonic field parameters. Table 2.3 below summarises the characteristics of both low-finesse and fibre-tip approaches towards constructing an ultrasonic sensor. Also included for comparison purposes are the characteristics of a typical PVDF hydrophone.

Medical ultrasound optical sensor type	Minimum detectable pressure $Pa/\sqrt{Hz}$
Extrinsic polymer film cavity [Ref 26]	~ 2 Pa (f = 0 to 25 MHz).
Uncoated fibre tip hydrophone [Ref 23,27]	~1 MPa (f = 0 to 10 MHz).
Multilayer fibre tip hydrophone [Ref 28]	~10 kPa (f = 0 to 10 MHz).
0.5mm diameter PVDF bilaminar membrane. Model Y-34-3698. (From Chapters 4,5 of this thesis)	~1.3 Pa (f = 1.911 MHz)

Table 2.3 Summary of pressure sensitivities for other types of optically-based medical ultrasound sensors.

2.5.3   Medical ultrasonic sensors based on optical fibre birefringence changes.

Medical sensors based on fibre birefringence changes have not been developed to the same extent as the fibre-tip and low-finesse sensors discussed previously. Some research [29,30,31] has examined the feasibility of constructing a broad-band fibre ultrasonic sensor. The studies of [29,30,31] were concerned only with comparing the theoretically calculated birefringence changes with those observed experimentally. No attempt or discussion was undertaken towards any potential medical applications. However, one particular study [32] has demonstrated the feasibility of constructing a

sensor based on ultrasonically induced fibre birefringence changes, for measuring the output parameters of a focussed ultrasonic transducer. The length of sensing fibre used in [32] (~5cm) precludes its use as an in-vivo point sensor. Again, the study of [32] was not concerned with the construction of an in-vivo medical sensor. The aim instead was to measure the spatial beam profile of a focussed ultrasonic transducer. The sensor of [32] was found to give some indication of the beam profile but its large size compared to other forms of optical sensor discussed previously precluded its use for any point measurements.

2.6 Optical Acoustic Hydrophones

Optical acoustic hydrophones differ from the medical sensors discussed previously in that the frequency range of interest is of the order of 20Hz – 20kHz i.e. audible frequencies. The development of optical fibre hydrophone technology has been driven primarily by military applications, namely sonar systems for ship and submarine detection.   The basic principle involved is to incorporate a sensing length of optical fibre into one arm of an interferometer [33], as shown in figure 2.5. The Nd:YAG laser provides a high power (several 10's of milliwatts) and long coherence length (~few km) source. The sensitivity can be enhanced by having several tens or even hundreds of meters of fibre in the sensing coil, depending on the source coherence length. A path imbalance exceeding the source coherence length will not give rise to interference.
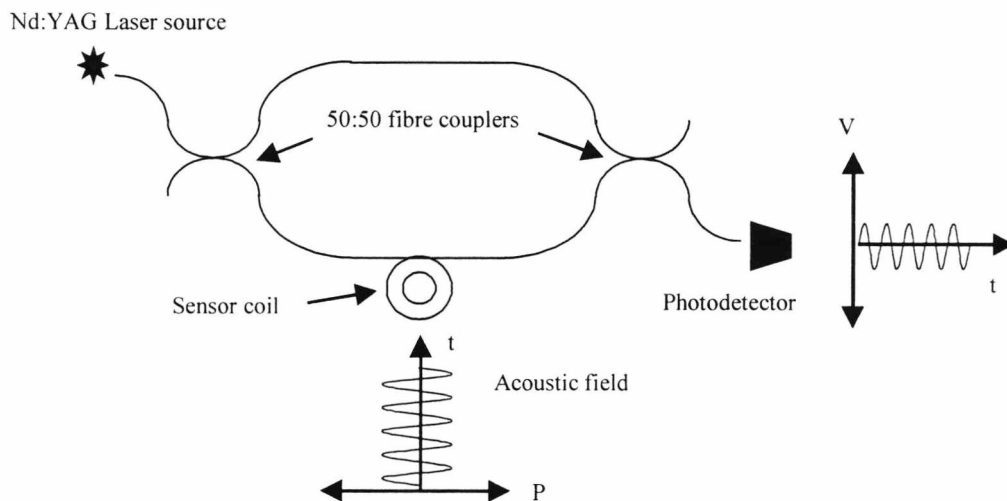
Figure 2.5 – Optical hydrophone based around a Mach-Zehnder   interferometer

Acoustic fields incident on the sensing fibre coil give rise to phase changes in the optical signal as discussed previously in this chapter. The relative phase difference between the sensing and the reference arm of the interferometer manifests itself as an intensity change at the interferometer output, readily detectable by a suitable photodetector. Mandrel based optical fibre interferometric hydrophones [33] can give acoustic detection sensitivities far in excess of those achievable with conventional piezoelectric devices, but have an upper frequency response of kHz or a few tens of

kHz at best. This upper frequency response as well as the size of the sensor coil (several cm) obviously precludes their use in medical applications where small size (preferably submillimetre) and high frequency response (upwards of hundreds of kHz) are necessary. The figure of merit used in characterizing interferometric hydrophone systems is the sensitivity relative to Deep Sea State Zero (DSSO). This is the noise floor experienced in the quietest parts of the deep ocean, and in terms of acoustic pressure is –80 dB relative to 1 Pascal /$\sqrt{Hz}$ @ 1kHz, or 10^{-4} Nm^{-2} @ 1 kHz. The type of system outlined in figure 2.5 can easily achieve an acoustic detection sensitivity equal to or even in excess of DSSO. These types of hydrophone systems are discussed more extensively in Chapter 6 of this thesis, where the results from previous research are compared with a multiplexed array of in-fibre erbium lasers. A recent and exciting development in the field of optical sensing involves the use of single-mode in-fibre grating based erbium laser cavities. The narrow linewidth of single-mode lasers lends itself to interferometric interrogation techniques [34] that can potentially provide acoustic detection sensitivities approaching or even exceeding the DSSO figure of merit. An array of FBG lasers is interrogated interferometrically to convert the strain-induced frequency shift in the laser to a phase and hence intensity change in the interferometer output. This technique is examined experimentally in some detail in Chapter 6 of this thesis, with particular emphasis on identifying the primary noise sources in the system and various techniques for minimising these sources where possible. A more detailed discussion of optical hydrophones is also given in chapter 6, with comparisons of the detection sensitivities of different types of optical acoustic hydrophones.

2.7   Summary.

The brief overview given in this chapter illustrates that optical fibres can be used to construct ultrasonic and acoustic sensors based on a number of construction and interrogation techniques. Some of the ideas discussed here will be expanded more fully in following chapters where FBGs, single-mode Er^{3+} FBG lasers and low-finesse, low coherence interferometric cavities are examined both theoretically and experimentally to determine their applicability as :-

1. Ultrasonic sensors in the case of the FBGs and low-finesse cavities with a view to potential medical applications.
2. A multiplexed array of acoustic sensors in the case of the erbium fibre lasers.

References :

1. YUXING, Z. and SCEATS, M.G.: ' Theory of Acoustic Sensing using Optical Fibres', International Journal of Optoelectronics, 1991, **6**, Nos.1/2 pp. 101-116.

2. FLAX, L., COLE, J.H., DE PAULA, R.P and BUCARO, J.A.: ' Acoustically induced birefringence in optical fibers', Journal of the Optical Society of America, 1982, **72**, No.9, pp. 1159-1162.

3. DE PAULA, R.P., FLAX, L., COLE, J.H., and BUCARO, J.A.: 'Single _mode Fiber Ultrasonic Sensor' IEEE Journal of Quantum Electronics, Apr. 1982, Vol. QE-18, No.4, pp. 680-682.

4. HOCKER, G.B.: 'Fiber-optic sensing of pressure and temperature', Applied Optics, May 1979, 18, No. 9, pp. 1445-1448.

5. BERWICK, M, PANNELL, C.N., RUSSELL P. ST. J, JACKSON, D.A.: 'Demonstration of birefringent optical fibre frequency shifter employing torsional acoustic waves', Electronics Letters, 27, No.9, pp 713-715, 1991.

6. JI, J., UTTAM, D., CULSHAW, B.: 'Acousto-optic frequency shifting in ordinary single-mode fibre', Electronics Letters, 22, No.21, pp 1141-1143, 1986.

7. HILL, K.O., FUJII, Y., JOHNSON, D.C, KAWASAKI, B.S. "Photosensitivity in optical fiber waveguides,: application to reflection filter fabrication", Applied Physics Letters, **32**, pp.647-649, 1978.

8. MELTZ, G., MOREY, W., GLENN, W.H., "Formation of Bragg Gratings in optical fibres by a transverse holographic method.", Optics Letters, **14**, No. 15, 823-825.

9. XIONG, Z., PENG, G.D., WU, B., CHU P.L., "Highly Tunable Bragg Gratings in Single mode Polymer Optical Fibres", IEEE Photonics Technology Letters, Vol.11, No.3, pp.352-354, March 1999.

10. CANNING, J., PASMAN, R., SCEATS, M.G., KRUG, P.A., "Photosensitisation of weak phosphosilicate fibre Bragg gratings", Proceedings of Conference on Photosensitivity and Quadratic Non-Linearity in Glass Waveguides, Optical Society of America, Portland, Oregon, USA, p86-89, (1995).

11. FRIEBELE, E.J., GRISCOM, D.L., "Colour centres in glass optical fibre waveguides", Materials Research Society Symposium Proceedings, 61, pp 319-330, 1986.

12. YUEN, M.J., "Ultraviolet absorption studies of germanium silicate glasses", Applied Optics, 21, pp 136-148, 1982.

13. HAND, D.P., RUSSELL, P. St.. J., "Photoinduced refractive-index changes in germanosilicate fibres", Optics Letters, 15(2), pp 144-146, 1990.

14. HANDEREK, V.A., "Fibre Gratings: Principles, fabrication and properties" Optical Fibre Sensor Technology, Vol.2, 1998, Chapman and Hall.

15. SOLINAS, D.G., MARTIN DE STERKE, C., SIPE, J.E., "Coupled-mode equations for deep nonlinear gratings", Optics Communications, 111, 15th Sep. 1994, pp 105-110.

16. BOO-GYOUN, K., CAMIRE, E., "Comparison between the matrix method and the coupled-wave method in the analysis of Bragg reflector structures.", Journal of the Optical Society of America, 9, No.1, Jan 1992, pp 132-136.

17. RAO. Y.: 'Fiber Bragg Grating Sensors: Principles and Applications', in 'Optical Fiber Sensor Technology', 1998, Vol. 2, Chapman and Hall, London.

18. COLEMAN, A. J. and SAUNDERS, J.E.: ' A review of the physical properties and biological effects of the high amplitude acoustic fields used in extracorporeal lithotripsy', Ultrasonics, 1993, 31, No. 2, pp. 75-82.

19. HAND, J.W.: 'Control of Ultrasound Hyperthermia Treatment', Ultrasonics, 1992, 30, No. 2, pp. 125-127.

20. PRESTON, R.C., BACON, D.R., LIVETT, A.J and RAJENDRAN, K.: 'PVDF membrane hydrophone performance properties and their relevance to the measurement of the acoustic output of medical ultrasonic equipment.' J.Phys.E: Sci.Instrum., 1983, 16, pp. 786-796.

21. MARTIN, C.J., and LAW, A.N.R.: 'Design of thermistor probes for measurement of ultrasound intensity distributions', Ultrasonics, March 1983, pp. 85-90.

22. BEISSNER, K., 'Intercomparison of acoustic output measurements of a diagnostic ultrasound device.', Ultrasound in Medicine & Biology', Vol. 25, No. 4, pp. 629–636, 1999.

23. STAUDENRAUS, J. and EISENMENGER, W.: 'Fibre-optic probe hydrophone for ultrasonic and shock-wave measurements in water', Ultrasonics, 1993, 31, No. 4, pp. 267-273.

24. HYNYNEN, K. and EDWARDS, D.K.: ' Temperature measurements during ultrasound hyperthermia', Med. Physics, Jul/Aug. 1989, 16, No.4, pp. 618-626.

25. KERSEY, A.D.: 'Interrogation and Multiplexing techniques for Fiber Bragg grating strain sensors', Proc. SPIE, Vol. 2071, pp. 30-48.

26. BEARD, P.C. and MILLS, T.N.: 'Extrinsic optical-fiber ultrasound sensor using a thin polymer film as a low-finesse Fabry-Perot interferometer', Applied Optics, Feb. 1996, 35, No. 4, pp. 663-675.

27. KOCH, Ch., LUDWIG, G. and MOLKENSTRUCK, W.: ' Calibration of an interferometric fiber tip sensor for ultrasound detection.', Ultrasonics, 1997, 35, 297-303.

28. KOCH, Ch..: 'Coated fiber-optic hydrophone for ultrasonic measurement.', Ultrasonics, 1996, 34, 687-689.

29. DE PAULA, R.P., COLE, J.H., and BUCARO, J.A.: 'Broad-Band Ultrasonic Sensor Based on Induced Optical Phase Shifts in Single-Mode Fibers', Journal of Lightwave Technology, Vol. LT-1, No. 2, Jun. 1983, pp. 390-393.

30. BUCARO, J.A., DARDY, H.D. and CAROME, E.F.: 'Fibre-optic hydrophone', J. Acoust. Soc. Amer., 1977, 62, pp. 1302-1304.

31. COLE, J.H., JOHNSON, R.L. and BHUTA, P.G.: 'Fiber-optic detection of sound', J. Acoust. Soc. Amer., 1977, 62, pp. 1136-1138.

32. CHAN, H. L. W., CHIANG, K.S., PRICE, D.C., GARDNER, J.L., and BRINCH, J.: 'Use of a fibre-optic hydrophone in measuring acoustic parameters of high-power hyperthermia transducers.', Phys. Med. Biol., 1989, 34, No. 11, pp. 1609-1622.

33. NASH, P.: 'Review of interferometric optical hydrophone technology', IEE Proc. Radar, Sonar Navig., 143, No. 3, Jun. 1996. pp. 204-209.

34. KOO, K.P. and KERSEY, A.D.: 'Bragg Grating-Based Laser Sensor Systems with Interferometric Interrogation and Wavelength Division Multiplexing.', Journal of Lightwave Technology, Jul. 1995.

Chapter 3

Interferometric Interrogation of the FBG.

3.1 Introduction.

The field of optical sensing has seen a marked increase in recent years in the use of FBG's to sense a wide range of parameters such as strain, pressure, temperature, acoustic field strength and (with suitable coatings) magnetic fields [1,2]. As the measurand of interest is encoded as a wavelength shift in the FBG peak reflectivity it seems obvious that some form of wavelength-dependent interrogation method is called for. The primary advantage of having the measurand encoded as a wavelength change instead of an amplitude change is that it is far easier to make absolute measurements of wavelength than it is of amplitude, amplitude-based measurements being subject to the effects of noise, equipment calibration uncertainties and drift. For quasi-static measurands such as temperature, strain and pressure a commercially available tunable optical filter such as a fibre Fabry-Perot can be used to scan over the wavelength range of interest. For dynamic measurands such as sonic and ultrasonically-induced strains the scanning rate (~100Hz maximum) of commercially available filters is too low to allow the FBG response to be measured. As interferometers are devices whose optical outputs are functions of wavelength it seems sensible to investigate the feasibility of using an interferometer as a means of interrogating the FBG for the measurement of dynamic strains at high frequencies.

3.2   Two–Beam Interferometer Transfer Function

The output amplitude of a two beam interferometers is given by the sum of the amplitudes of the two separate beams in the interferometer arms, possibly with some degree of phase shift between the arms. Typical interferometers of this type are Mach-Zehnder and Michelson interferometers; a fibre-based Mach-Zehnder interferometer is shown in figure 3.1.
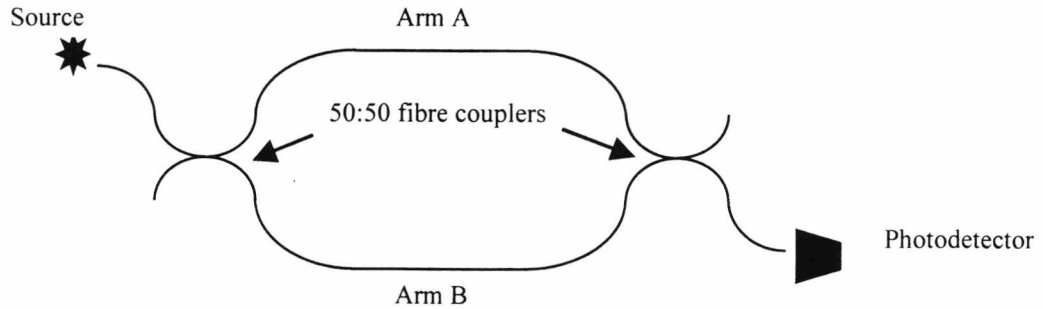
Figure 3.1 – Fibre-based Mach-Zehnder interferometer.

Expressing the electric field amplitudes of the optical signal in each arm of the interferometer in complex notation gives, assuming that the incident electric field is split evenly between the two arms:

$$E_A = \frac{E_0}{\sqrt{2}}\exp\left[i\left(\omega t - kz + \phi_A + \Phi\right)\right] \tag{3.1}$$

$$E_B = \frac{E_0}{\sqrt{2}}\exp\left[i\left(\omega t - kz + \phi_B\right)\right] \tag{3.2}$$

Where E_o is the incident electric field amplitude, ω is the angular frequency of the optical wave of wavevector k propagating in the z direction. ϕ_A, ϕ_B are slowly varying environmentally-induced phase shifts in arms A,B of the interferometer and Φ is the static phase difference between the arms. The environmental phase shifts can be due to mechanical movements from vibration, or from temperature changes, for example. The electric field amplitude E_D at the photodetector is given by :

$$E_D = \frac{1}{\sqrt{2}}\left(E_A + E_B\right) \tag{3.3}$$

Hence the optical intensity I_D at the photodetector is proportional to the time-average of the square of the incident electric field intensity i.e

$$I_D \propto \frac{1}{2}\left\langle \left(E_A + E_B\right)\cdot\left(E_A + E_B\right)^* \right\rangle \tag{3.4}$$

where * denotes complex conjugation and $\langle \; \rangle$ denotes time-averaging.

Expanding equation (3.4) gives :-

$$I_D \propto \frac{1}{2}\left\langle E_A^2 + E_A E_B^* + E_B^2 + E_A^* E_B \right\rangle \tag{3.5}$$

where E_A^*, E_B^* denote the complex conjugates of E_A, E_B. Assuming a 50:50 coupling ratio gives $E_A^2 = E_B^2 = E_0^2 / 2$. Expanding $E_A E_B^*, E_A^* E_B$ in terms of complex exponentials gives the following expressions :-

$$\left\langle E_A E_B^* \right\rangle = \frac{\left\langle E_0^2 \right\rangle}{2} \exp[i(\omega t - kz + \phi_A + \Phi) - i(\omega t - kz + \phi_B)] = \frac{\left\langle E_0^2 \right\rangle}{2} \exp(i(\phi_A - \phi_B + \Phi)) \tag{3.6}$$

$$\left\langle E_A^* E_B \right\rangle = \frac{\left\langle E_0^2 \right\rangle}{2} \exp[i(\omega t - kz + \phi_B) - i(\omega t - kz + \phi_A + \Phi)] = \frac{\left\langle E_0^2 \right\rangle}{2} \exp(i(\phi_B - \phi_A - \Phi)) \tag{3.7}$$

Using the trigonometric identity $2\cos(x) = \exp(ix) + \exp(-ix)$ with $x = (\phi_A - \phi_B + \Phi)$ gives, combining (3.6) and (3.7) :-

$$E_A E_B^* + E_A^* E_B = E_0^2 \cos(\phi_A - \phi_B + \Phi) \tag{3.8}$$

Substituting from equations (3.1), (3.2) and (3.8) and simplifying gives:

$$I_D \propto \frac{1}{2}\left[2\left\langle E_0^2 \right\rangle + \left\langle E_0^2 \right\rangle \cos(\phi_A - \phi_B + \Phi)\right] = \frac{1}{2}\left\langle E_0^2 \right\rangle[1 + \cos(\phi(t) + \Phi)] \tag{3.9}$$

where $\phi(t) = \phi_A - \phi_B$. Simplifying further and using $\left\langle E_0^2 \right\rangle = I_0$ gives the final expression (equation 3.10) for the output intensity I_D at the photodetector, assuming no optical losses and a 50:50 splitting ratio in the couplers:

$$I_D = \frac{I_0}{2}[1 + \cos(\phi(t) + \Phi)] \tag{3.10}$$

In situations where the splitting ratio is unequal the transfer function is given by:

$$I_D = \frac{I_0}{2}[1 + V\cos(\phi(t) + \Phi)] \qquad V = \frac{I_{MAX} - I_{MIN}}{I_{MAX} + I_{MIN}} \tag{3.11}$$

where V is the interference fringe visibility, I_{MAX}, I_{MIN} are the maximum and minimum values of the output intensity. The static phase difference Φ is determined by the optical path difference L ($= nL_{PHYSICAL}$) between the arms of the interferometer, and is given by (at the FBG peak wavelength):

$$\Phi = \frac{2\pi L}{\lambda_{FBG}} \tag{3.12}$$

Of particular interest and relevance to optical sensing is the interferometer response to a low-coherence source such as a superluminescent diode (SLD). This is shown below in figure 3.2
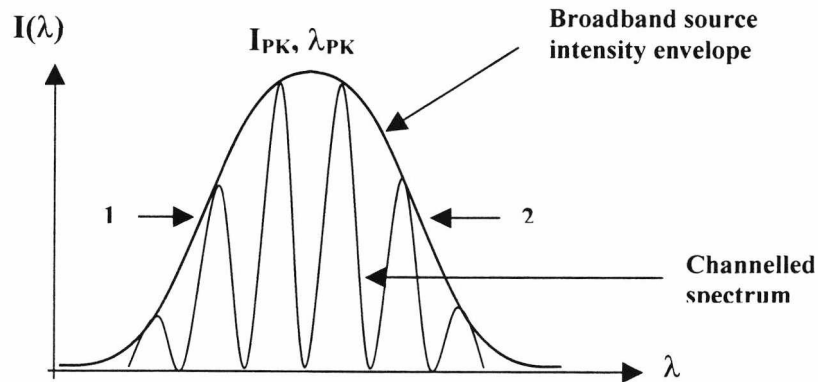
Figure 3.2 – Channeled spectrum from a low-coherence source.

From figure 3.2, the source full width half maximum (FWHM) between points 1,2 is typically 20-25 nm for a source at a peak wavelength λ_{PK} of 830 nm, although obviously there will be some variation between different devices. The spectral profile of an SLD as a function of frequency v is often approximated by equation 3.13 for ease of use. However, the spectral profile of an SLD is more accurately represented by a Voigt function [9].

$$I(v) = \frac{1}{(2\pi)^{\frac{1}{2}}\Delta v} \exp- \left(\frac{(v_0 - v)^2}{2\Delta v^2} \right) \tag{3.13}$$

Δv is a measure of the SLD bandwidth (= FWHM) and v_0 is the centre frequency. The fringe visibility $V(L)$ of the above intensity profile when the SLD is passed through an interferometer is given by:

$$V(L) = \exp- 2\left(\frac{\pi L \Delta v}{c}\right)^2 \tag{3.14}$$

where c is the velocity of light and L is the optical path difference. Optical power into a single-mode optical fibre can be in excess of 10 mW for more recent devices (see www.superlum.ru). The static channelled spectrum shown in figure 3.2 can be modulated by changing the optical path difference in one of the interferometer arms by use of a suitable optical device [3]. A discussion of the advantages of this approach forms the basis of subsequent sections

3.3 Optical Interrogation Techniques:

3.3.1 Periodicity and dynamic range of an interferometric sensor.

The previous analysis for the fibre Mach-Zehnder shows that the interferometer transfer function varies with a periodicity of 2π radians, equivalent to an optical path length difference of λ. If the interferometer is to be used as a sensor and the output is to be a unique function of optical path length change then the unambiguous operational range will be limited to $\lambda/2$. This is because the phase sensitivity ($dI_{OUT}/d\Phi$) is a periodic function, and will be at a maximum where the gradient of the interferometer transfer function is a maximum. For a cosine transfer function this will be at $\Phi = \pm n\pi \pm \pi/2$, ($n$=0,1,2). This is known as the quadrature position and over a small range of phase shifts around this position the phase sensitivity will be approximately linear. For sensor applications it is obviously useful to have constant linear sensitivity. The phase difference between the interferometer arms will be arbitrary due to environmental influences and the difficulty of constructing an interferometer with zero path imbalance. Hence any displacement measurements made when the system is switched on are made relative to an unspecified optical path difference. If reproducible measurements are to be made then the optical path length of at least one of the arms must be invariant. Even if this could be achieved without difficulty, then some method of counting both the number of interference fringes and also the direction of the fringe movement would be needed to ascertain the displacement over a range greater than $\lambda/2$. The inherent difficulties and ambiguities of a simple interferometric approach with a

laser source implies that some alternative method of signal processing is required if unambiguous and accurate measurements are needed.

3.3.2 Heterodyne Techniques for FBG interrogation

If the channelled spectrum described previously is swept across the FBG then the output from the interferometer will be intensity modulated at a frequency determined by the spectrum sweep rate and a carrier frequency will be generated. If in turn the FBG is acoustically modulated the this will have the effect of modulating the carrier phase, giving rise to heterodyning of the FBG signal with the carrier [4]. This technique is illustrated in the following series of figures for a Mach-Zehnder interferometer (see figure 3.3) illuminated by a broadband source. Included in one arm of the interferometer is an optical phase (or frequency modulator) electrically driven at a frequency ω_C. The resultant channelled spectrum from the interferometer is incident on a fibre Bragg grating of peak wavelength λ_B. The backreflected light from the FBG is incident on a photodetector. C1, C2 and C3 are 50:50 fibre couplers.
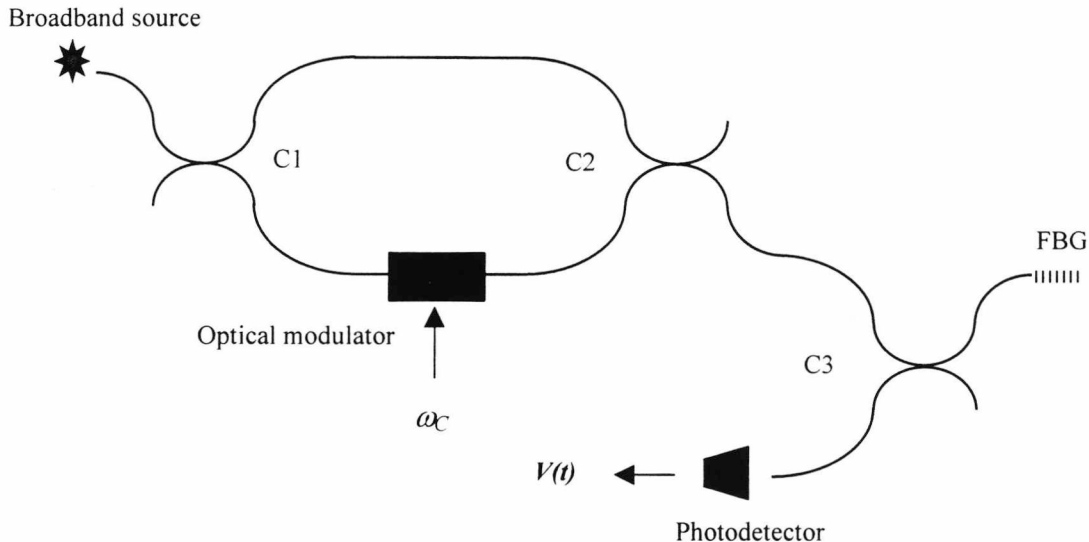
Figure 3.3 – FBG illuminated by output of phase modulated Mach-Zehnder interferometer connected to a broadband source.

An alternative optical interrogation topology to the one shown in figure 3.3 is where the positions of the source and photodetector are swapped over. This creates no difference in the intensity of the backreflected signal from the FBG incident on the photodetector

and the two topologies are therefore effectively equivalent in terms of detection sensitivity. This is because in the spectral domain the system can be modelled by multiplying the source spectrum by the spectral transfer functions of the interferometer and grating – clearly it does not matter in what order the multiplication is carried out.

Consider now the following series of figures for situations based on figure 3.3 where both the optical modulator and FBG are unmodulated (figure 3.4); where only the optical modulator is being driven (figure 3.5) and finally where both the optical modulator is being electrically driven and the FBG is being dynamically strained at a frequency ω_B (figure 3.6). The parameter of interest in all three of these situations is the time-dependent photodetector output signal $V(t)$. Figure 3.4 shows the static channelled spectrum from the interferometer incident on the FBG. As neither the channelled spectrum or the FBG peak wavelength have any time dependence the photodetector output $V(t)$ is a constant function of time.
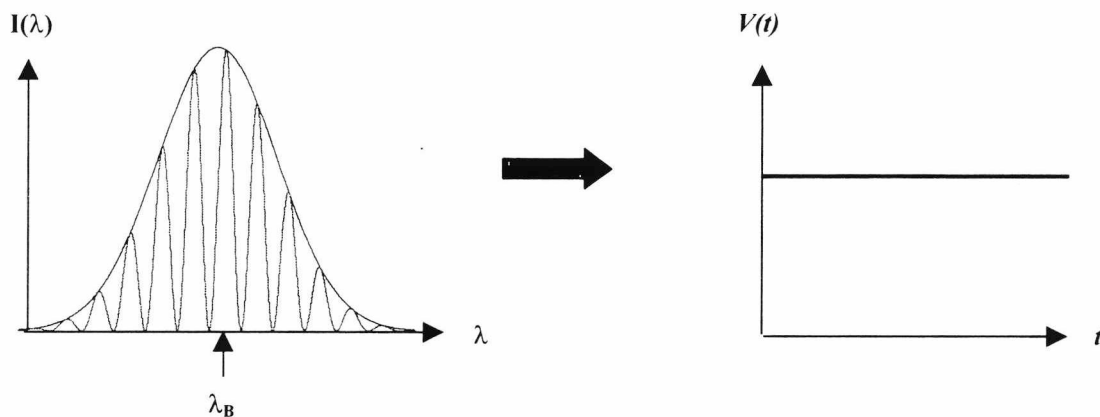
Figure 3.4   Static channelled spectrum incident on unstrained FBG

With the optical modulator sinusoidally driven at a frequency ω_C the channelled spectrum is swept across the FBG at the same frequency as the modulator driving frequency. Hence the peaks and troughs of the channelled spectrum will give rise to a time-dependent illumination of the FBG and the backreflected light from the FBG and the photodetector output voltage will show the same time dependence. (Fig 3.5) overleaf.
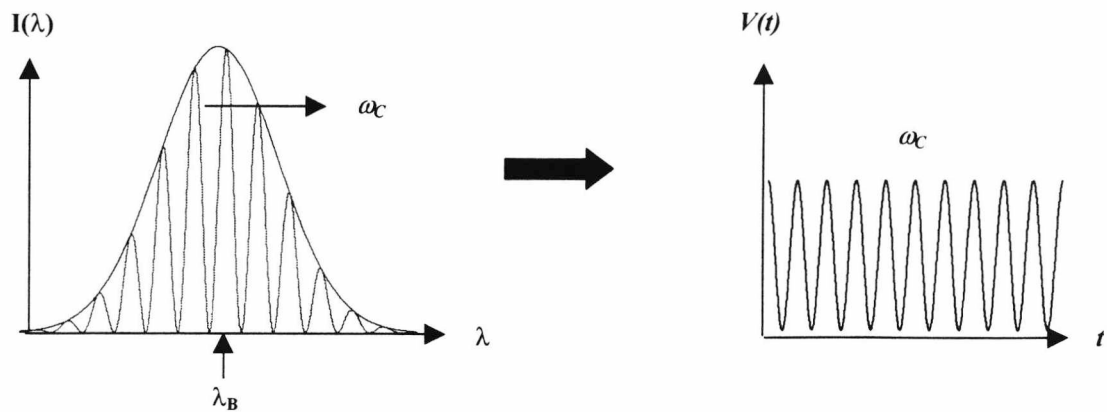
Figure 3.5   Swept channelled spectrum incident on unstrained FBG.

The combination of a swept channelled spectrum and dynamically strained FBG is shown in figure 3.6. The effect of the dynamic strain on the FBG is to effectively shift the FBG peak reflectivity at the dynamic strain frequency ω_B. This adds an extra frequency modulation to the carrier signal generated by the optical modulator. This effect is known as heterodyning. The output signal from the photodetector is now a function of both ω_C and ω_B. The magnitude of the dynamic strain induced shift of the FBG peak wavelength and the resultant form of $V(t)$ shown in figure 3.6 have been exaggerated for the sake of clarity.
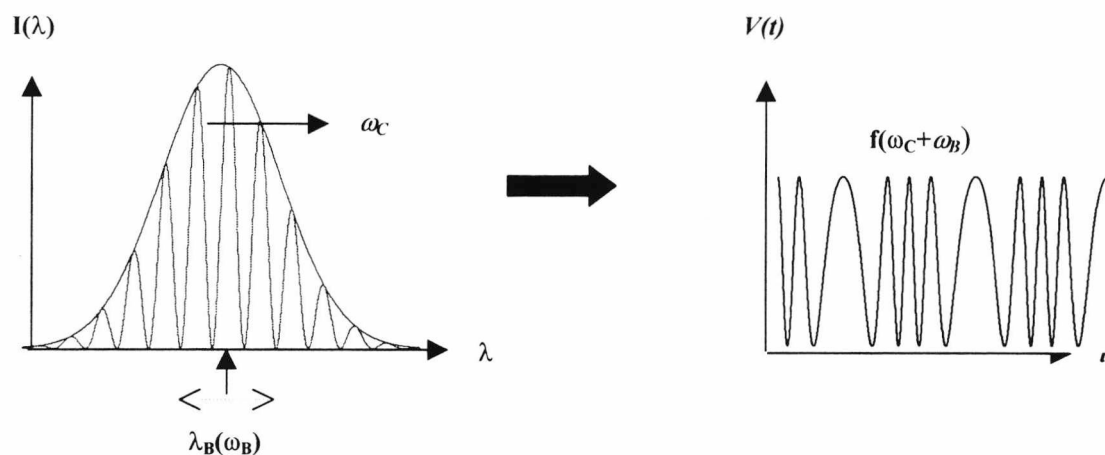
Figure 3.6   Swept channelled spectrum with dynamically strained FBG

A Fourier analysis of the photodetector output signal (Appendix A) demonstrates that the dynamic strain signal from the FBG is represented by an infinite series of Bessel functions. This is illustrated schematically in figure 3.7.
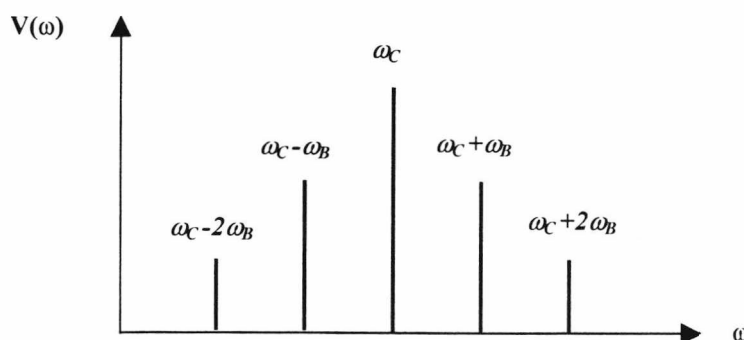
Figure 3.7   Frequency spectrum of photodetector output voltage for swept channelled spectrum with dynamically strained FBG.

For sake of clarity only two of the sidebands have been shown on figure 3.7, which is effectively the frequency spectrum shown on an (electrical) spectrum analyser with the input signal being the photodetector output voltage. As will be shown shortly, for small wavelength shifts in the FBG peak only the first two sidebands at $\omega_C \pm \omega_B$ will be measurable, the higher order sidebands being negligible.

Heterodyning is an attractive method of signal recovery for a number of reasons. The first is that the phase detection sensitivity is constant and does not depend on the arbitrary environmentally-induced phase shifts discussed previously and the need to operate the interferometer at quadrature. Also the dynamic range is much larger, as the signal of interest is encoded as a phase shift on a carrier frequency rather than an amplitude change in the interferometer output, which is effectively limited to an unambiguous displacement range of $\lambda/2$. Either the phase or the frequency of the optical signal in the fibre can be modulated to generate a carrier. Phase modulation can be achieved by using a lithium niobate (LiNbO$_3$) optical phase modulator, or by warpping a fibre coil around a PZT cylinder. Lithium niobate is an electro-optic material whose refractive index and hence optical path length is a function of the applied electric field strength. If the applied voltage to the device is linearly ramped the optical path length will also change linearly. Obviously the voltage ramp cannot be continued indefinitely and so the voltage must at some point return to zero.
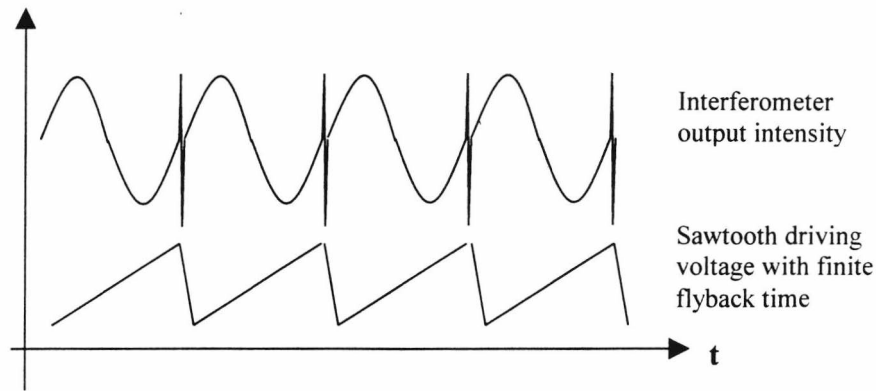
Figure 3.7   Effect of ramping phase modulator on interferometer output.

Repeating the process gives rise to a sawtooth waveform. The sawtooth voltage is set so as to give an effective 2π phase change in the modulator and hence theinterferometer output. This is illustrated in figure 3.7. The finite flyback time of the sawtooth wave causes discontinuities in the interferometer response. This method of carrier generation is known as pseudo-heterodyne or sometimes as serrodyne modulation. An alternative method of carrier generation uses a acousto-optic Bragg cell to provide true heterodyne modulation without the discontinuities associated with the lithium niobate phase modulator. Both of these carrier generation techniques effectively give rise to the same result – a carrier frequency phase modulated by the signal of interest, in this case a dynamic strain acting on the FBG. This can be expressed as:-

$$I_{OUT} = A\big[1 + V(L)\cos\big(\omega_c t + \phi(t) + \Phi + \delta\Phi\sin\omega_s t\big)\big] \qquad (3.15)$$

where ω_c, ω_s the are carrier and signal angular frequencies, A is a constant proportional to the FBG reflectivity, $\phi(t), \delta\Phi$ are the amplitudes of the environmental and measurand-induced phase shifts respectively and Φ is the static phase difference. A periodic strain-induced wavelength change in the grating of $\delta\lambda_B$ gives rise to a phase modulation in equation 3.15 given by :

$$\delta\Phi\sin(\omega_c t) = \frac{2\pi L}{\lambda_B^2}\delta\lambda_B\sin(\omega_c t) \qquad (3.16)$$

A Fourier analysis of (3.15) (Appendix A) reveals that the spectrum of the phase modulated carrier can be expressed as the sum of an infinite series of Bessel functions, as shown below:

$$I_{OUT} = A\left[1 + V(L)\sum_{n=-\infty}^{\infty}J_n(\delta\Phi)\cos[(\omega_C + n\omega_S)t + \phi(t) + \Phi]\right] \tag{3.17}$$

For small modulation amplitudes ($\delta\Phi \ll 1$) the Bessel functions can be approximated by the following formula [5]

$$J_n(x) \approx \frac{1}{n!}\left(\frac{x}{2}\right)^n + O(x^{n+2}) \tag{3.18}$$

where $O(x^{n+2})$ denotes terms of the order of $n+2$. The carrier amplitude will therefore be given by the zeroth-order Bessel function :

$$I_{CARRIER} = AV(L)J_0(\delta\Phi) = AV(L) \tag{3.19}$$

and the amplitude of the first sideband will be:

$$I_{\omega_S} = AV(L)J_1(\delta\Phi) = A\exp-2\left(\frac{\pi L \Delta v}{c}\right)^2\left(\frac{2\pi L}{\lambda_B^2}\delta\lambda\right) \tag{3.20}$$

Maximising the above equation (Appendix B) allows the value of optical path difference L to be found which maximises the first sideband amplitude and hence the acoustic detection sensitivity. This condition is satisfied when :

$$L = \frac{c}{2\pi\Delta v} \tag{3.21}$$

and for a FBG of ~0.2nm FWHM at 820 nm peak reflectivity is approximately equal to 500 microns.

3.4   Factors influencing the FBG detection sensitivity.

3.4.1 Optical detectors and detector responsivity.

Optical detectors can be broadly divided into those with and without internal gain mechanisms independent of any external electronic amplification circuitry. Detectors without internal gain are those consisting of a *p-n* or sometimes *p-i-n*   (p-intrinsic-n) junction which simply produce a current due to the photovoltaic effect when light is incident on the semiconductor junction. Active devices are those such as photomultiplier tubes and avalanche photodiodes (APDs). Photomultipliers were not used in this thesis due to the ready availability of commercially built Si APD's. An APD is essentially a *p-n* or *p-i-n* diode operated at a high reverse bias. At such a high bias, the free carriers (electrons and holes) in the depletion region are accelerated to high speeds. Such a carrier with high kinetic energy can excite an electron in the valence band to the conduction band and therefore create an electron and a hole. This one-carrier -> three-carrier process is called an impact ionization process or avalanche process. As a result, the initial photocurrent current is amplified; in a Si APD this amplification factor can be as high as 100-200 in commercially available detectors. The detector responsivity will be a function of optical wavelength [6]. In this thesis, the wavelengths of interest are ~820 nm; ~1280 nm and ~1550 nm from the various optical sources used in the experimental work. The type of material used in the detector will differ depending on the optical wavelength to be detected. For ~820 nm the material with the optimum responsivity is Si; for longer wavelengths either Ge or InGaAs based detectors are used. In this thesis a silicon (APD) was used at 820 nm. For longer wavelengths PIN InGaAs diodes coupled to a transimpedance (current to voltage) amplifier were used. The responsivity $R(\lambda)$ in a given wavelength interval $d\lambda$ can be defined as [6] :

$$R(\lambda) \cdot d\lambda = \frac{GeneratedPhotocurrent\ (A)}{IncidentOpticalPower\ (W)} = \frac{e\lambda n(\lambda) \cdot d\lambda}{hc} \qquad (3.22)$$

where e is the charge on an electron, $n(\lambda) \cdot d\lambda$ is the quantum efficiency at wavelength λ and h, c are Planck's constant and the velocity of light respectively. The generated photocurrent i_{PH} for an optical power P_{OPT} over the wavelength interval $d\lambda$ is

simply given by $P_{OPT} * R(\lambda) \cdot d\lambda$. Typical values of $R(\lambda)$ at the wavelengths of interest are ~0.5-0.6 for Si detectors at 820 nm and ~0.9 to 0.95 for InGaAs PIN diodes at 1280 and 1550 nm. For an active photodetector such as a APD where amplification of the initial photocurrent takes place within the device the value of $R(\lambda)$ can be significantly higher.

3.4.2 Photodetector shot noise.

Any optical detector will have associated noise, a particularly important noise source being the optical shot noise [6] due to the Poisson statistical fluctuation in the number of photogenerated electrons in the material of the detector. An expression [7] for the rms value of this noise current in a measurement bandwidth B Hz is given below:

$$ i_{RMS} = \left(\overline{i^2}\right)^{\frac{1}{2}} = \left(2ei_{PH}B\right)^{\frac{1}{2}} \tag{3.23} $$

where i_{PH} is the detector photocurrent as defined previously. For a typical optical power of $1\mu W$ and a measurement bandwidth of 1kHz, the shot noise will be of the order of $1.3*10^{-11}$ A for a detector responsivity of 0.5. The noise spectral density is flat, hence shot noise is classified as 'white' noise. Of particular interest is the variation of the photocurrent/shot noise ratio as the optical power increases. This can be derived from (3.23) and is simply proportional to $P_{OPT}^{0.5}$. Hence as the optical power increases the effects of shot noise become less significant and the signal to noise ratio will be increased, assuming that the detection system is shot-noise limited. In practice this fundamental limit is difficult to achieve due to the presence of other noise sources.

3.4.3 Thermal (Johnson) noise.

Momentary asymmetries in the charge distribution in a conductor due to the random thermal movement of electrons will give rise to a fluctuating noise voltage. As there are a very large number of electrons and their movement is statistically uncorrelated the central limit theorem [5] demonstrates that the thermal noise voltage has a Gaussian amplitude distribution with a zero mean value. The frequency distribution is flat, hence Johnson noise is also classified as 'white' noise. The open circuit rms value of this

noise voltage is given by [6,7] as :

$$\left(e_n\right)_{RMS} = \left(\overline{e_n^2}\right)^{1/2} = \left(4kTRB\right)^{1/2} \tag{3.24}$$

where k is Boltzmann's constant, T is the absolute temperature, R is the resistance of the conductor in ohms and B is the measurement bandwidth in Hz. For a 10 kΩ resistor at room temperature will have an open-circuit rms voltage of around 1.3 μV in a 10 kHz measurement bandwidth, which is a considerable noise voltage. This noise source is of particular importance in the design of electronic amplifiers used to amplify the small photocurrents from a photodetector. The resistive part of any impedance in the amplifier circuit generates Johnson noise which can be amplified in successive stages of the amplifier. Johnson noise is a fundamental noise source and can be minimised by careful circuit design.

3.4.4 1/f noise (flicker noise)

In addition to the shot and Johnson noise another noise source must be accounted for at low frequencies. This is the 1/f noise or 'flicker' noise, where the noise amplitude has a 1/f dependence with frequency. At higher frequencies this noise is insignificant by comparison with other noise sources. However, 1/f noise can be significant for measurements in the 100's of Hz range and below. This noise source is a function of both the material and construction of the device. Carbon based resistors in particular exhibit a high level of 1/f noise. A typical value of 1/f noise for a carbon-based resistor is ~0.1 to ~3.0 μV/Volt [8] measured over one decade of frequency.

3.4.5 Amplifier noise and signal to noise ratio (SNR).

Although not a fundamental noise source the net result of all of the previously discussed noise sources is an increase in the output noise of the amplifier. In practice the signal to noise ratio (SNR) will be determined by the values of the above noise sources and the amplifier construction in general – APD or *p-i-n* diode based, for example, or whether the amplifier is a current to voltage (transimpedance) amplifier or some other type. In terms of the rms signal and noise voltages and powers, the SNR can be expressed as:

$$SNR = 20 \log_{10}\left(\frac{V_S}{V_n}\right) \text{ (dBV)} = 10 \log_{10}\left(\frac{P_S}{P_n}\right) \text{ (dB)} \qquad (3.25)$$

The above expressions for SNR will be bandwidth dependent. This is of particular importance in the detection of narrow band signals as in the case of the phase-modulated carrier discussed previously. Here the modulating signal of interest appears as a narrow sideband. The SNR can be increased in this particular case by the simple process of reducing the detection system bandwidth.

3.4.6   Fringe Visibility

The ideal fringe visibility will be equal to one only for an interferometer with an equal optical intensity and polarisation state in each interferometer arm. Where the optical intensity or polarisation state differs between each arm of the interferometer the fringe visibility will be less than 1. This will be unavoidable in fibre interferometers where changes in fibre birefringence due to environmental influences will affect the optical polarisation states in the interferometer.

3.5   Summary

The use of heterodyne signal processing techniques allows the effects of environmentally-induced interferometer drift to be accounted for, as the measurand is encoded as a phase shift on a carrier at a significantly higher frequency (10's of MHz) than the slowly varying environmental drifts. The dynamic range is high, as the measurand of interest is not limited to a $\lambda/2$ wavelength shift as in the simple interferometric interrogation scheme discussed previously. In the next chapter, both a heterodyne and a psuedo-heterodyne scheme are discussed and examined experimentally as a means of providing FBG interrogation at ultrasonic frequencies.

References :

1.   JACKSON, D.A., "Recent Progress in monomode fibre-optic sensors", Measurement Science and Technology, **5**, 194, pp. 621-638.

2.   RAO, Y-J., "Fiber Bragg grating sensors: Principles and applications.", Optical Fiber Sensor Technology, Vol. 2, Chapman and Hall, 1998, Edited K.T.V. Grattan, B.T.Meggitt.

3.   MEGGITT, B.T., BOYLE, W.J.O., GRATTAN, K.T.V., BARUCH, A.E., PALMER, A.W., "Heterodyne processing scheme for low coherence interferometric sensor systems", IEE Proceedings-J, Vol. 138, No. 6, Dec. 1991, pp. 393-395.

4.   BETTS, J. A., "Signal processing, modulation and noise", London, English Universities Press, 1970.

5.   BOAS, M.L., "Mathematical Methods in the Physical Sciences", 2nd ed. Imprint: New York, Wiley, 1983.

6.   YARIV, A.: 'Optical Electronics', 4th Edition, Imprint: Philadelphia, London, Saunders College Pub., 1991.

7.   DE SA, A., "Principles of Electronic Instrumentation", Imprint: London, Edward Arnold, 1981.

8.   HOROWITZ, P., HILL, W., "The Art of Electronics", Imprint: Cambridge, New York, Cambridge University Press, 1980.

9.   ARMSTRONG, B. H.: 'Spectrum Line Profiles: The Voigt Function.' J. Quant. Spectrosc. Radiat. Transfer, **7**, pp. 61-88, 1967.

Chapter 4

Experimental Results from a FBG acoustic Sensor

4.1 Experimental Arrangements

4.1.1 Pseudo-heterodyne system.

Two separate systems were investigated as a means of interrogating the FBG. A psuedo-heterodyne [1] system based around an unbalanced fibre Mach-Zehnder (courtesy of Dr. N. Fisher, UKC Optics Group) and a lithium niobate phase modulator was used to interrogate a FBG at a wavelength of 820nm. A second system constructed by the author of this thesis (fig 4.2), used an acousto-optic Bragg cell to provide true heterodyne carrier generation by effectively shifting the frequency of the optical signal. The wavelength here was centred around 1280 nm, again from an SLD. The pseudo-heterodyne system with an 820 nm SLD is shown below in figure 4.1.
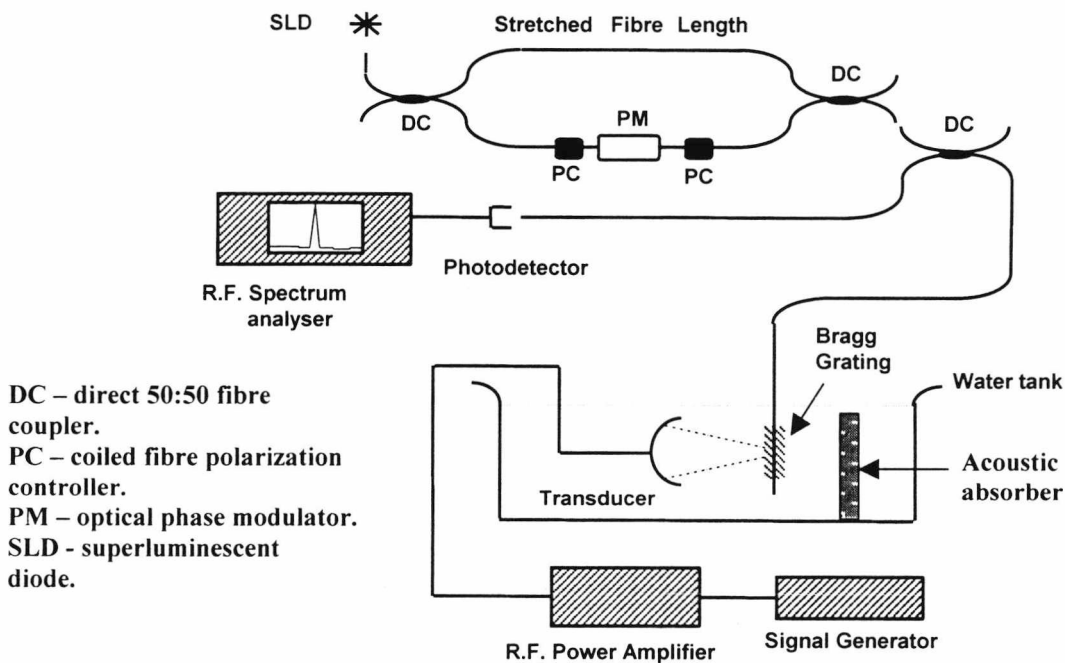
Figure 4.1 – Psuedo-heterodyne interferometric interrogation system for ultrasonically modulated FBG

4.1.2 Equipment details.

The broadband source consisted of a fibre-pigtailed superluminescent diode model SLD38-HP with an optical power into single-mode fibre of ~5 mW. The diode peak wavelength was 820 nm with a full-width half maximum of 22nm. The diode was maintained at a constant temperature by virtue of being mounted on a Peltier solid-state cooler. This acted to prevent any thermal runaway of the diode and also, more importantly, provided wavelength stabilisation, as the diode peak wavelength is a function of the diode operating temperature. This diode was a commercially available unit. Current control of the diode and of the Peltier cooler was provided by two laboratory constant-current sources which were able to provide up to 500mA diode forward current and ~1.5A stabilised Peltier cooler current. The phase modulator was a lithium niobate device with an insertion loss of < 2dB and an active phase modulator length of ~5 cm, although this figure is at best approximate and was estimated from the device external dimensions. In practice a detailed measurement of the active lithium niobate region was unnecessary, as the uncertainty that this introduced into the optical path difference between the interferometer arms could be compensated for by stretching one fibre arm of the interferometer with a linear translation stage. The phase modulator was driven by a sawtooth wave at 10 MHz from a function generator (not shown in figure 4.1 for sake of clarity), the optimum voltage for a 2π interferometer phase shift being approximately 2.5 volts. All fibre used in interconnecting the optical arrangement was single-mode fibre, the fibre being optimised for single-mode operation at a wavelength of ~820 nm.

The optical path imbalance could be varied to maximise the phase modulation of the carrier by stretching one arm of the interferometer with a linear translation stage. The length of fibre between the fixed ends was approximately two metres. As the fibre can undergo ~10 millistrain before breaking, this allowed a maximum optical path imbalance of around 2 cm to be obtained, although in practice this was found to be unnecessary. Of particular importance in building the interferometer was the need to ensure that all fibre lengths were measured accurately so that the point of zero path imbalance lay within the range obtainable by stretching one of the fibre arms. The polarization controllers (PC) were simple coiled birefringence based controllers where

the coil radius was such that the phase retardation between the polarization eigenstates was either 90° (a quarter wave plate) or 180° (a half-wave plate). In practice the controllers consisted of three identical discs, the central disc functioning as a half-wave plate by the simple expedient of having two turns of fibre. Twisting the discs in a plane perpendicular to the longitudinal fibre axis created stress-induced birefringence allowing the polarisation state to be adjusted and the fringe visibility to be maximised. At the start of each experimental session some adjustment was always found to be necessary due to environmental effects. The controller before the phase modulator (PM) enabled the polarisation dependence of the modulator to be accounted for. The direct couplers (DC) were nominally 50:50 couplers with a flat coupling ratio over the spectral width of the SLD. The fibre Bragg grating was a 5mm long grating with a peak reflectivity of ~90% at 820 nm, the FWHM of the grating being ~0.2 nm. This grating was provided by Aston University. The FBG was mounted on an x-y-z translation stage (not shown in figure 4.1 for sake of clarity) to allow its position to be scanned along the spatially varying ultrasonic field. The back-reflected light from the FBG was incident on a photodetector, which consisted of a commercially available silicon avalanche photodiode (APD) module from Hamamatsu Electronics with an integral amplifier stage. The APD output signal was examined on a RF spectrum analyser to allow the signal characteristics to be determined. To allow acoustic energy transfer to the FBG and to more accurately simulate the conditions inside the body both the FBG and ultrasonic transducer were immersed in a tank of water. This was also necessary to allow correct functioning and cooling of the transducer. To prevent the formation of any acoustic standing waves in the tank an acoustic absorber consisting of a section of mineral wool was placed at the back of the tank. This was to prevent any potential distortion of the ultrasonic field profile. The ultrasonic transducer consisted of a spherical section concave focussing transducer with a radius of 30 mm and a focal length of 80 mm intended primarily for medical applications, the resonant frequency of this transducer being 1.911 MHz, the maximum acoustic output power being ~40 watts. Transducer excitation was provided by a second signal generator coupled to a RF power amplifier. The electrical power requirements of the transducer were considerably greater (~50-100W) than could be provided by the signal generator alone. The transducer conversion efficiency was ~30%, hence an electrical power to the transducer

of 10W gave an acoustic output power of ~3W. Accurate measurements of the ultrasonic pressure were provided by a calibrated polyvinylidene difluoride (PVDF) [2] hydrophone with an active area of 0.5 mm^2, allowing a comparison between the FBG response and the true acoustic pressure.

4.1.3 Heterodyne system.

A second interrogation system using an acousto-optic Bragg cell and an unbalanced Mach-Zehnder interferometer was constructed. This system is shown below in figure 4.2.
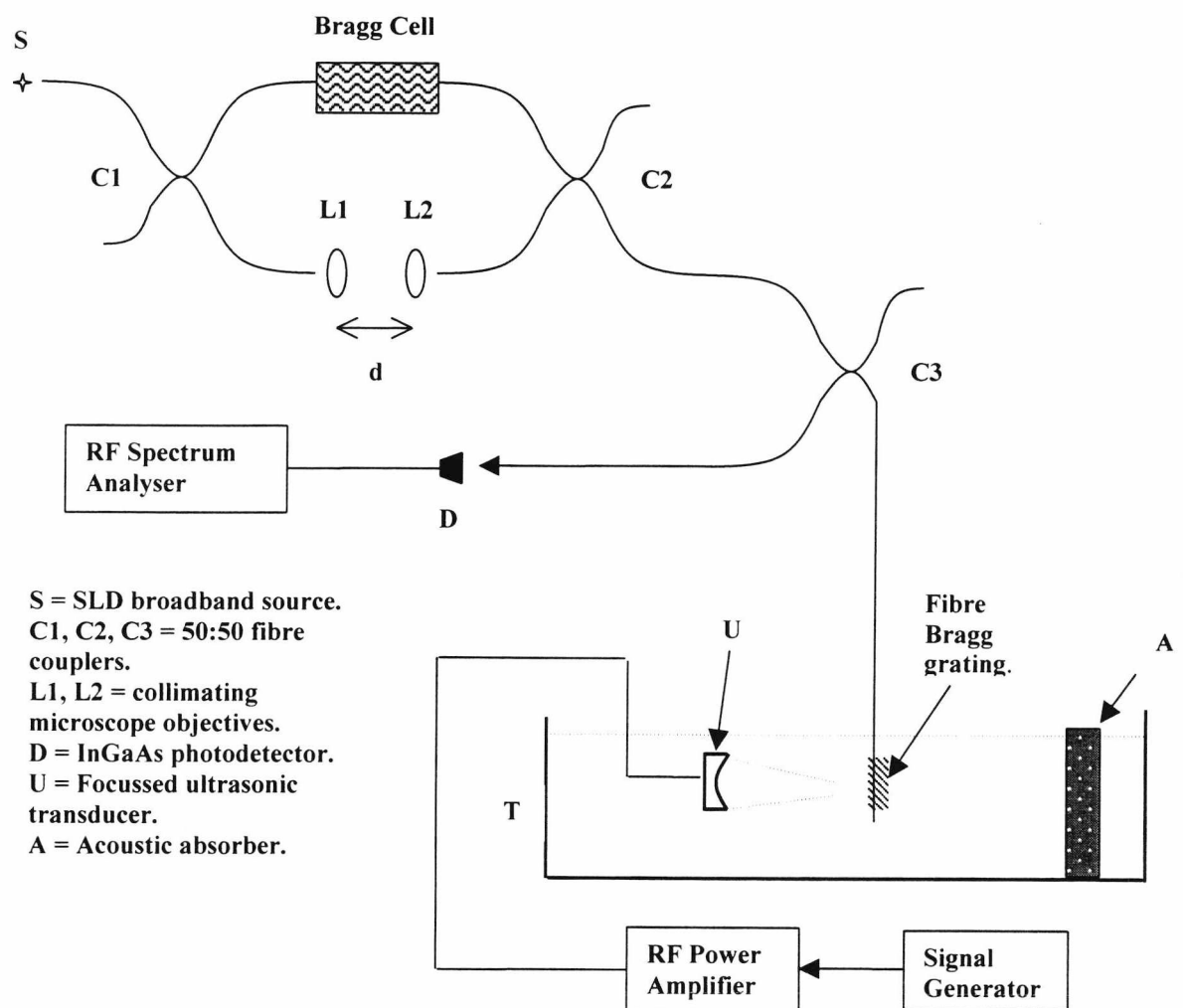
Figure 4.2 Heterodyne interrogation system for ultrasonically modulated Bragg grating.

In the experimental arrangement of figure 4.2, S is a fibre-pigtailed superluminescent diode source type SLD56-HP, with a full width half maximum of ~42 nm at an output power of a maximum of 10 mW into single-mode fibre at a peak wavelength of 1280 nm. C1, C2, C3 are all commercially available fibre taper couplers optimised to have the correct 50:50 splitting ratio at the system peak operating wavelength of 1280 nm. The Bragg cell was a commercially available acousto-optic fibre pigtailed frequency shifter unit (M040-8J-F2S from manufacturers Gooch and Housego) which is able to provide a high diffraction efficiency at the operating wavelength, giving an insertion loss of less than 2.4 dB from the manufacturers specifications. The Bragg cell operates at 80 MHz and for this particular model gives a frequency downshift, although the direction of the frequency shift provided by the Bragg cell will not affect the experimental results in any way. L1, L2 are collimating 10× microscope objectives to allow the light emerging from the bare fibre end to be re-coupled into the other fibre forming part of the interferometer air gap. Lens L2 was mounted on a linear translation stage to allow the distance d between the objectives to be changed. This is to compensate for the unknown optical path length of the Bragg cell and also to allow the interferometer optical path difference to be optimised to maximise the phase modulated carrier signal from the grating. The FBG was a 5 mm long grating which had a peak reflectivity wavelength of 1280 nm with a FWHM of ~0.25 nm. The fibre Bragg grating sensor is mounted on an x-y-z translation stage (not shown for sake of clarity), which allowed the sensor to be scanned across the ultrasonic field spatial distribution. Also included in the water tank behind the sensor was an acoustic absorbing material (mineral wool) to absorb any power from the ultrasonic transducer to prevent the formation of standing waves in the water tank, which could potentially interfere with any experimental results. The ultrasonic transducer, signal generator, RF power amplifier and spectrum analyser were identical to that of figure 4.1.

The Bragg cell allows for true heterodyning as the optical signal in one of the fibre arms is continuously frequency modulated to provide the carrier, the modulation frequency being 80 MHz in this case. As with the psuedo-heterodyne system, a means of adjusting the optical path difference to maximise the carrier phase modulation was provided. This consisted of an adjustable air gap in one of the interferometer arms, the

Optical detection was provided by a commercially available InGaAs p-i-n diode with a transimpedance amplifier stage, providing high optical detection sensitivity at the SLD peak wavelength. Polarisation control was again provided by two coiled birefringent polarization controllers, one before and one after the Bragg cell. The FBG mounting arrangements were identical to those of the psuedo-heterodyne system, as were the ultrasonic transducer and calibrated hydrophone mounting arrangements. Signal demodulation and analysis was again provided by an RF spectrum analyser. In practice obtaining results from this system proved difficult and time-consuming due to the unforeseen need to re-align the objective lenses between each experimental session due to thermal expansion of the steel optical workbench. A system found to be aligned during one experimental session was found to be completely out of alignment at the beginning of the next session. As the output from one fibre is being re-focussed onto an area approximately 5 microns in diameter (the fibre core width of the other fibre in the air gap), it is unsurprising that alignment was found to be difficult. Hence the results quoted in this chapter have been obtained from the psuedo-heterodyne system, which needed no re-alignment between experimental sessions. However, the effort involved in building the system was not wasted, as the heterodyne experimental arrangement was used in a later experiment involving the investigation of low-finesse Fabry-Perot cavities (chapter 5).

4.2 Properties of a focussed ultrasonic transducer.

4.2.1 Acoustic Intensity and Pressure.

Before describing the characteristics of a focussed ultrasound transducer it is useful to have some background information relating quantities such as pressure, intensity and acoustic velocity. For a plane wave in water (or any other fluid) of density ρ_0, the instantaneous pressure p is given by [3]:-

$$p = \rho_0 vu \qquad (4.1)$$

where u is the particle velocity. The quantity $\rho_0 v$ is often called the specific acoustic impedance, denoted by Z. The acoustic velocity v is a liquid is given by the standard relationship $v = (K/\rho_0)^{0.5}$ [3] , where K is the bulk modulus of elasticity ($2.05*10^9$ Pa for water) and the density ρ_0 at 293 K is 0.998×10^3 kgm^{-3}. This gives an acoustic velocity of 1.433×10^3 ms^{-1}. More useful relationships are those between the acoustic intensity and the acoustic pressure, the acoustic intensity being defined as the average rate of energy flow through a unit area normal to the wave propagation direction. For a plane wave, the intensity I in Wm^{-2} is given by [3] :

$$I = \frac{p^2}{2\rho_0 v} = \frac{p^2}{2Z} \qquad (4.2)$$

Using the figure for acoustic velocity from above and the resonant frequency of the transducer (1.911 MHz) gives an acoustic wavelength λ in water of 0.75mm.

4.2.2 Acoustic attenuation.

As the acoustic wave propagates through the fluid some energy dissipation will take place due to viscous forces. From [3], an expression for the pressure attenuation as a function of distance z is given by :

$$p(z) = p(0)\exp-(2\alpha z), \qquad \alpha = \frac{\eta \omega^2}{2v^3 \rho_0} \qquad (4.3)$$

where η is the coefficient of viscosity ($1*10^{-3}$ Nsm^{-2} for water) and ω is the angular frequency of the acoustic wave. Calculating the quantity $2\alpha z$ for a frequency of 2 MHz and a distance of 10 cm in water gives $2\alpha z \approx 0.00136$. Hence the ultrasonic attenuation in water is negligible for the maximum frequency considered in the thesis.

4.2.3 Spatial field profile of a focussed ultrasonic medical transducer.

The spatial dependence of the acoustic field strength of a focussed transducer will depend on a number of factors. The first and most obvious factor will be the transducer radius of curvature and hence the focal length. Also important will be the resonant frequency of the transducer itself, which in turn determines the acoustic wavelength (in water, in this case). A typical spherical transducer of radius a is shown schematically below in figure 4.3. (from [3,4])
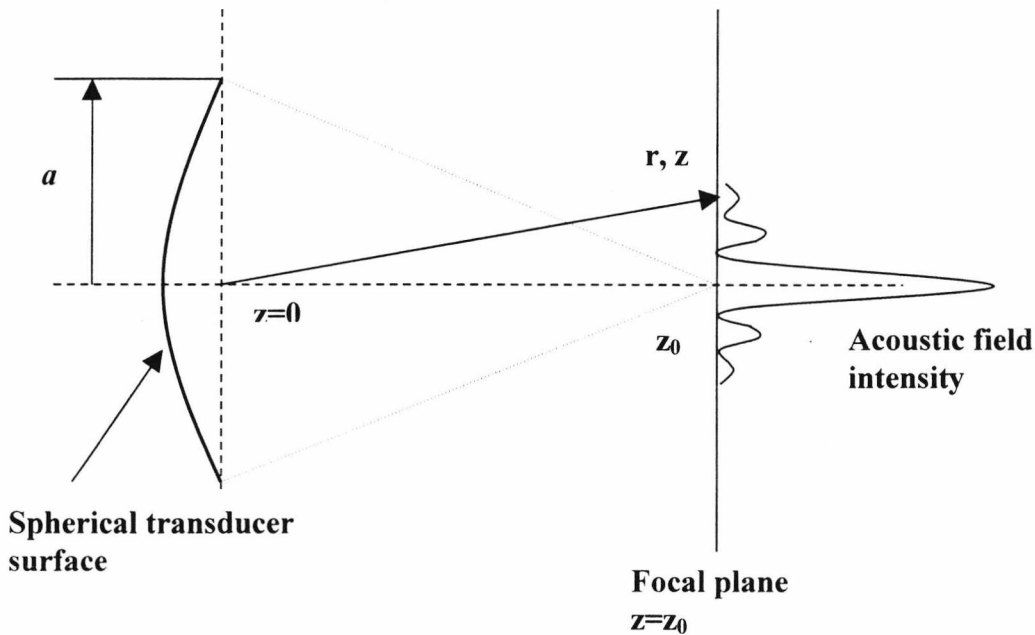
Figure 4.3 – Spatial field profile at distance r, z from a focussed spherical ultrasonic transducer of radius a in the focal plane $z = z_0$.

The acoustic field intensity in the focal plane $z = z_0$ can be described by the following mathematical expression [3,4]:-

$$\frac{I(r,z_0)}{I(0)} = \left(\frac{\pi a^2}{z_0 \lambda}\right)^2 \left(jinc\left(\frac{2\pi r a}{\lambda z_0}\right)\right)^2 \tag{4.4}$$

where $jinc(x) = J_1(x)/x$, J_1 being the first order Bessel function. The *jinc* function is analogous to the *sinc* function which appears in diffraction problems in optics. Equation (4.4) is effectively that of an Airy diffraction pattern which arises when imaging a point source with a circular lens. On figure 4.3 shown previously the sidelobe amplitudes have been exaggerated for the sake of clarity, and in reality are approximately 18 dB lower than the central peak. Hence most of the acoustic power (~84%) is concentrated in the central region. For the transducer used in these experiments, a=30 mm, z_0 = 80mm, λ = 0.75mm. Hence, the width of the central peak is given by the first zero of the first-order Bessel function. Hence, from (4.4) above,

$$\frac{2\pi r a}{\lambda z_0} = 3.832 \Rightarrow r \approx \frac{0.61 z_0 \lambda}{a} \tag{4.5}$$

for the first minimum of the field profile. This gives a central peak width of approximately 2.5 mm at the focal plane. Also of interest are the positions of the peaks of the first sidelobes. These will be determined by the maxima of the first-order Bessel function, and are given by :

$$\frac{2\pi r a}{\lambda z_0} = 5.136 \Rightarrow r \approx \frac{0.82 \lambda z_0}{a} \tag{4.6}$$

Hence the peak of the first sidelobe occurs at approximately 1.6 mm from the central peak. These results will be of importance when comparing experimental FBG-based measurements of the intensity profile with the theoretical profile.

4.2.4   Calibration of the focussed transducer.

To allow useful measurements to be obtained the ultrasonic transducer output was calibrated using a calibrated bilaminar shielded PVDF membrane hydrophone, model Y-34-3698 from GEC-Marconi. This hydrophone is designed for use in the general frequency range of 1 to 20 MHz and is shown in figure 4.4. It can be used in tap water and has excellent noise pickup immunity due to the large earth plane surrounding the active area, which in this case is $0.5mm^2$ of the piezoelectric polymer PVDF. The output voltage is directly proportional to the acoustic pressure incident on the active area.

Mounting ring and cover 75 mm diameter

Shielding 1mm width

75 ohm cable

Earthing pin

Active element 0.5 mm square
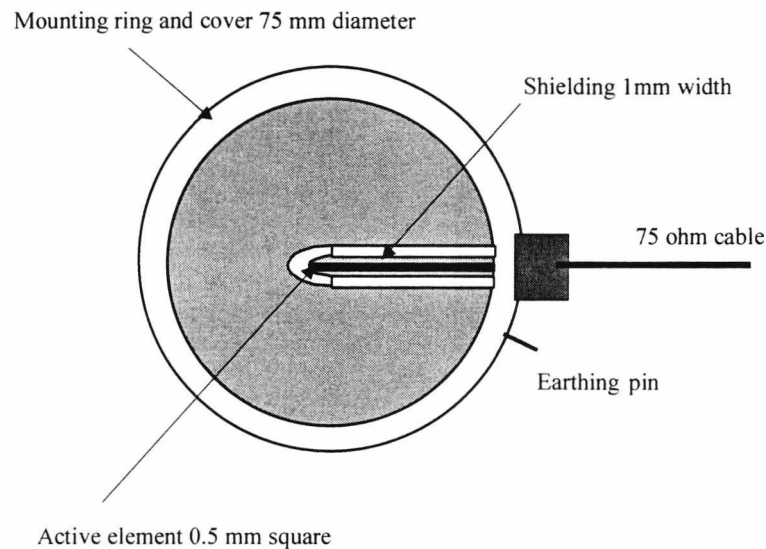
Figure 4.4 – Calibrated bilaminar shielded PVDF membrane hydrophone.

Calibration of the hydrophone was performed by the National Physical Laboratory (NPL) against a standard reference hydrophone over the frequency range 1-20 MHz. A typical pressure sensitivity for the hydrophone of figure 4.4 is ~48nV/Pa at 2 MHz, with a pressure measurement uncertainty of ± 7% from the calibration certificate. The frequency dependence of the acoustic sensitivity is minimal (± 1nV/Pa) over the frequency range 1-3 MHz. The calibrated hydrophone was used to measure the acoustic pressure at the focal point of the spherical transducer. This measured pressure was then compared with a calculation of the expected pressure to give some degree of confidence

that the hydrophone was working correctly. From a simple rearrangement of equation (4.2) , the acoustic pressure as a function of intensity is given by :

$$p = \sqrt{2\rho_0 Iv} \qquad (4.7)$$

From information supplied by Hammersmith hospital (suppliers of the spherical transducer), the transducer electrical to acoustic conversion efficiency is approximately 30%. Hence for a known electrical input power (~5.5W in this case), the acoustic output will be ~1.83W. As ~84% of the acoustic power is in the central peak, the average intensity over the focal point will be :

$$I_{av} \approx 0.84 \left(\frac{4W_{AC}}{\pi d^2} \right) \qquad (4.8)$$

where d is the central peak diameter of ~2.5 mm. Hence the acoustic intensity is ~3.73×10^5 Wm^{-2}. Converting this into a more meaningful pressure value using (4.7) above gives a pressure of ~1.03×10^7 Pa, or approximately 10 atmospheres. With the active area of the PVDF hydrophone at the focal point, the calculated pressure was 9.9 ± 0.7 atm, taking the calibration uncertainties into account. Hence the theoretical calculation of pressure is validated by the PVDF hydrophone, giving a high degree of certainty that any pressure measurements and calculations are accurate. An important use of the PVDF hydrophone was to calibrate the entire signal generator/RF amplifier/transducer system. A simple plot of acoustic pressure at the focal point as a function of the RF signal supplied to the amplifier was taken to allow the noise-limited pressure resolution of any other form of acoustic sensor to be assessed. The results of this measurement are shown in figure 4.5. The acoustic pressure at the transducer focus is a linear function of the applied RF voltage over the range 0-100 mV. Having calibrated the transducer output, the next step was to determine the ability of an FBG sensor to spatially resolve the ultrasonic field by scanning the FBG horizontally across the focal plane of the transducer using the x-y-z translation stages on the FBG mount. The FBG is positioned with its long axis (along the fibre) normal to the acoustic propagation direction.

Pressure (atm) vs RF (mV) for 1.911 MHz focussed transducer
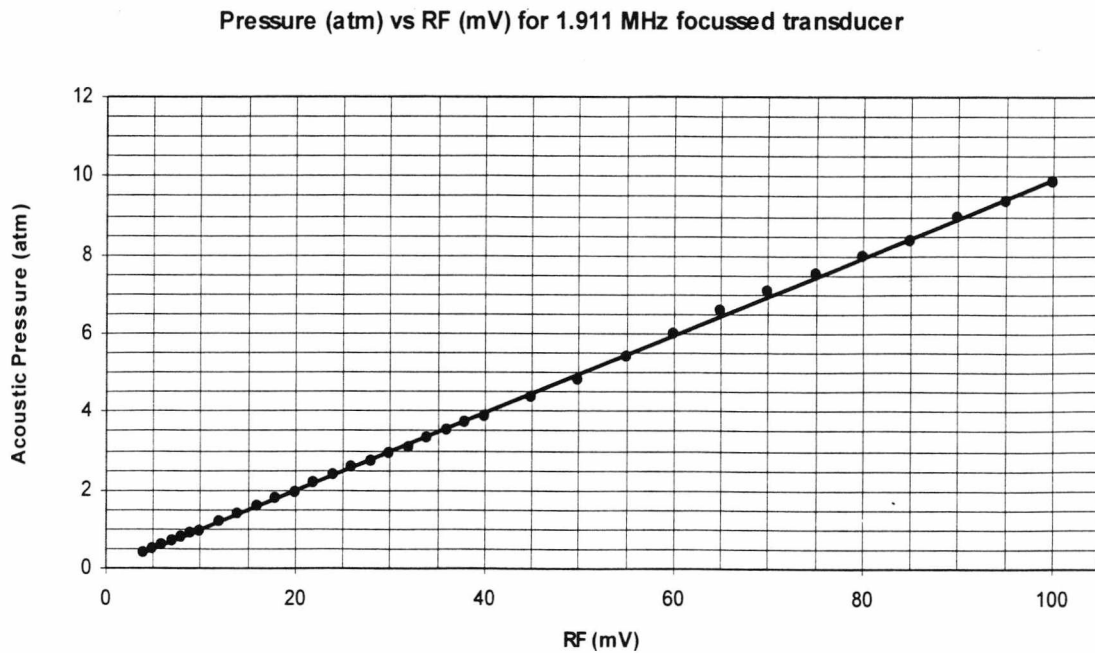
Figure 4.5 – Focal point pressure as a function of applied RF voltage.

The ultrasonic field profile obtained using the PVDF hydrophone can be seen in figure 4.6. It can be seen by comparison with figure 4.7 that the FBG field resolution is superior to that of the PVDF hydrophone by virtue of the FBG being significantly smaller than the active sensing element of the hydrophone.
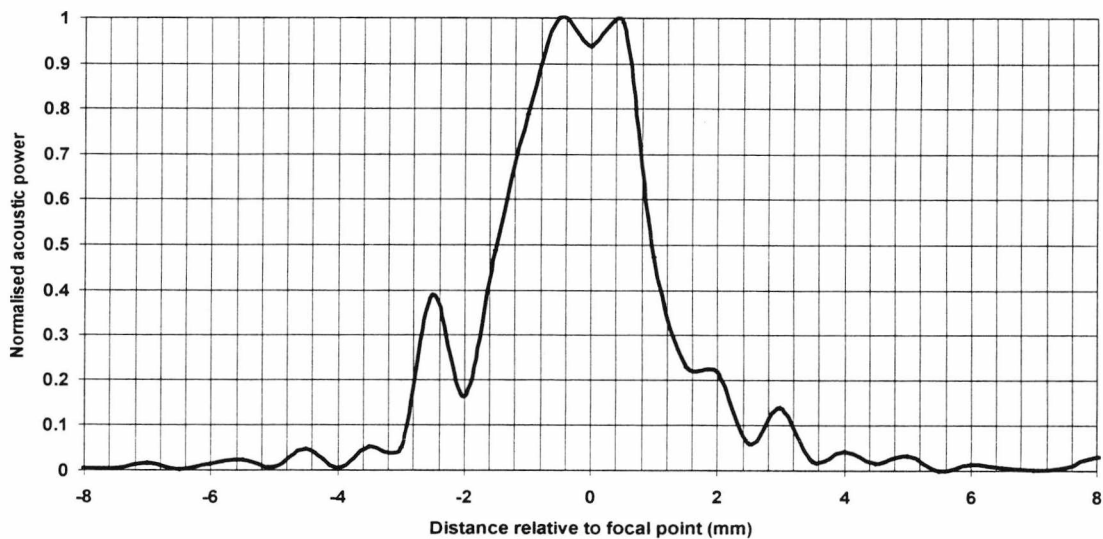
Figure 4.6 - Focussed transducer spatial field profile obtained using PVDF hydrophone

Unfortunately the PVDF hydrophone, although calibrated, it not strictly suitable for accurate field profile resolution due to the large surface area (see figure 4.4) of PVDF that surrounds the active sensing element. This large area of electrically inactive PVDF will nevertheless provide some degree of acoustic pickup which will in turn be mechanically transferred to the active sensing area. The theoretical field profile calculated with the actual transducer parameters is shown in figure 4.8 for comparison with the FBG response. It can be seen that the field profiles obtained with both the FBG sensor and the PVDF hydrophone differ markedly from the idealised distribution. This may be due to a number of factors. One obvious reason is that the transducer may have an uneven thickness, giving rise to an uneven electrical response over the spherical surface.
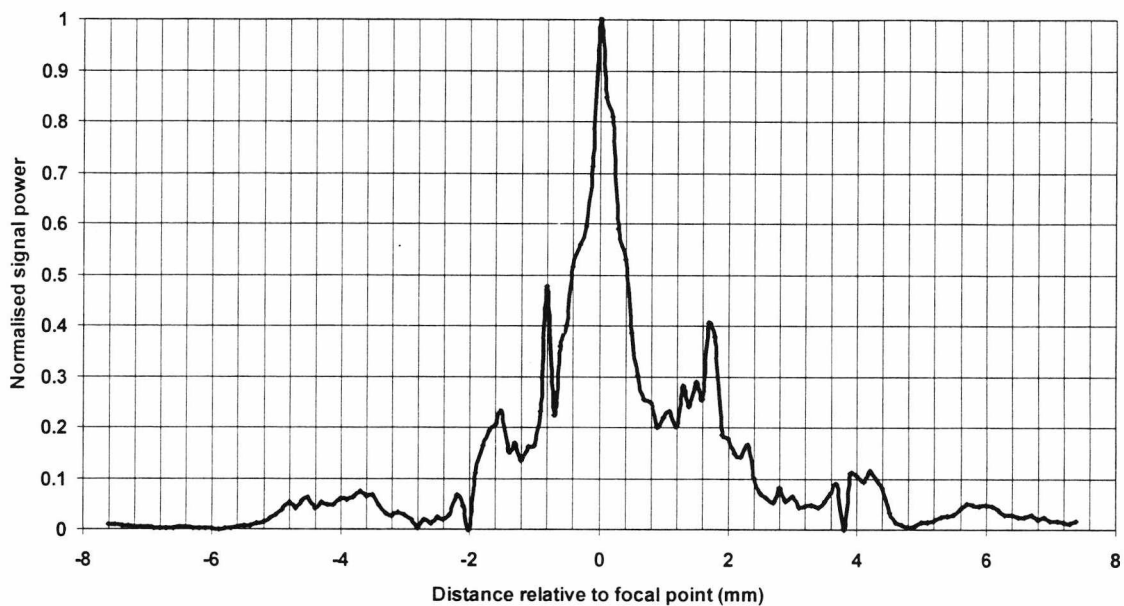
Figure 4.7 - Focussed transducer spatial field profile obtained using FBG sensor

The theoretical derivation of the idealised profile assumes an even response over the surface of the transducer for a given applied voltage, the transducer being composed of an electrically poled piezoelectric material such as lead zirconate titanate. Diffraction effects due to the circular surround holding the transducer are also a source of deviation from an idealised spatial profile. Another possible reason for an anomalous spatial field

resolution from the FBG sensor is a lack of point sensitivity due to propagation of acoustic signals along the bare length of fibre.
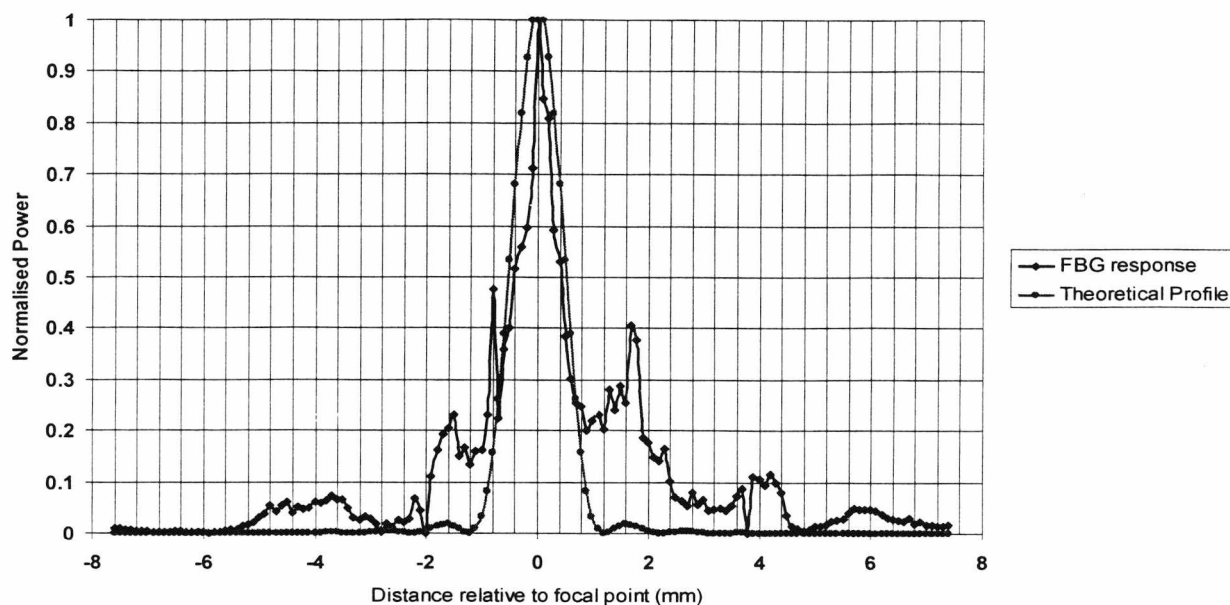
Figure 4.8 – Comparison of idealised spherical transducer spatial field profile with FBG response.

This possibility was investigated further by scanning the focal point of the acoustic transducer longitudinally along the bare length of fibre. The results of this investigation are given below in figure 4.9 which shows a typical side-band response (normalised to its carrier) with displacement, following a scan of the focal spot along the FBG/fibre. Note that the system response extends over a distance that is much *greater* than the grating length (5mm) and is *periodic*.
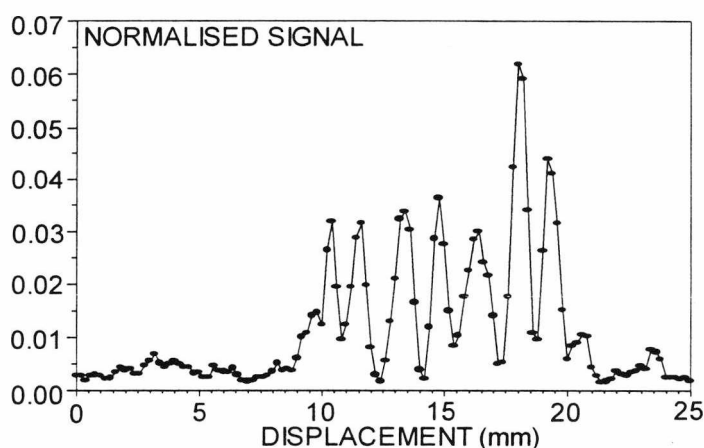
Figure 4.9 – Fibre response to longitudinal scan of acoustic focal point.

A possible explanation for the anomalous acoustic response seen in figure 4.9 is that acoustic coupling from the ultrasonic field to the optical fibre leads to the formation of compressional standing waves in the fibre. This may be due to partial back-reflections at the end of the fibre. The disturbance can extend many centimetres, and is illustrated diagramatically in figure 4.10. From figure 4.9, the average distance between successive peaks is ~1.47±0.05 mm, giving an acoustic wavelength of ~2.94±0.1 mm. It is of some interest to compare this experimentally observed acoustic wavelength with a calculated value for acoustic waves in fused silica.

Amplitude of compressional waves

Position

Acoustic field

Grating
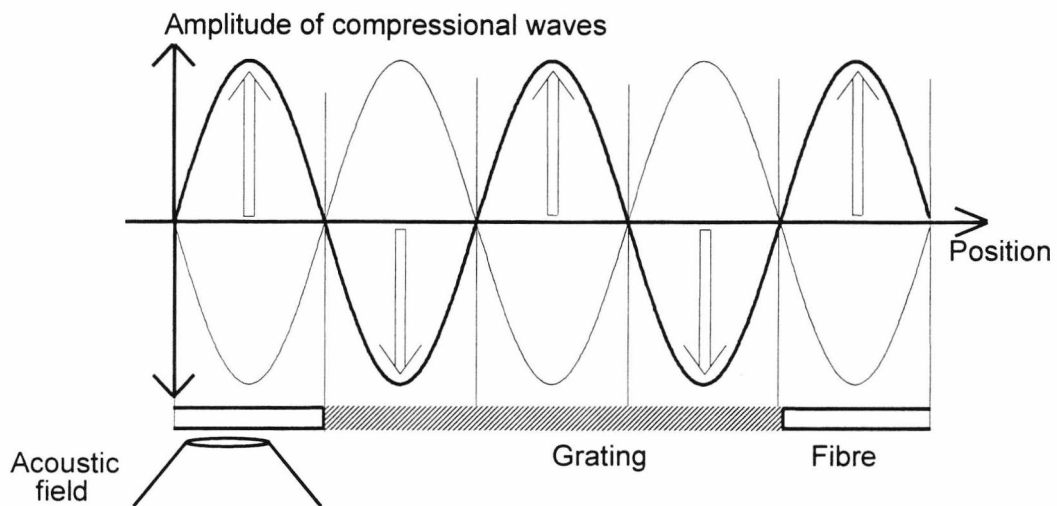
Fibre

Figure 4.10 – Formation of compressional acoustic standing waves in the fibre

From the standard relationship for the speed of sound in a solid, $v = \left(E/\rho_0\right)^{0.5}$ [3] , where E is the Young's modulus of elasticity and ρ_0 is the density. Inserting typical values for silica of 72GPa and 2.66×10^3 kgm^{-3} gives an acoustic velocity of 5.202 kms^{-1}. For an acoustic excitation frequency of 1.911 MHz this corresponds to an acoustic wavelength of ~2.72 mm. The reasonably close correspondence of the measured with the calculated acoustic wavelengths suggests that the compressional standing wave hypothesis is correct and also that the FBG alone cannot be used as a point sensor without some form of acoustic shielding of the bare fibre. Another indication that the compressional standing wave hypothesis is correct comes from the observation of a strong signal on the spectrum analyser at the acoustic excitation frequency. An obvious

source of this signal is electrical pickup from the RF amplifier. This was tested by switching off the optical source (SLD) while still providing acoustic excitation. This resulted in a significant decrease (~20dB) in the amplitude of the 1.911 MHz signal, thus confirming that the bulk of the observed signal was due to the FBG. For a pure heterodyne system, no such signal should be observed, hence some explanation for the existence of this apparently anomalous signal is required. One possible source of this signal would be amplitude modulation of the FBG reflectivity. To ensure that the response seen was due to the FBG alone, a length of bare fibre was substituted and the acoustic focal point was scanned along the fibre length. No system response was seen,
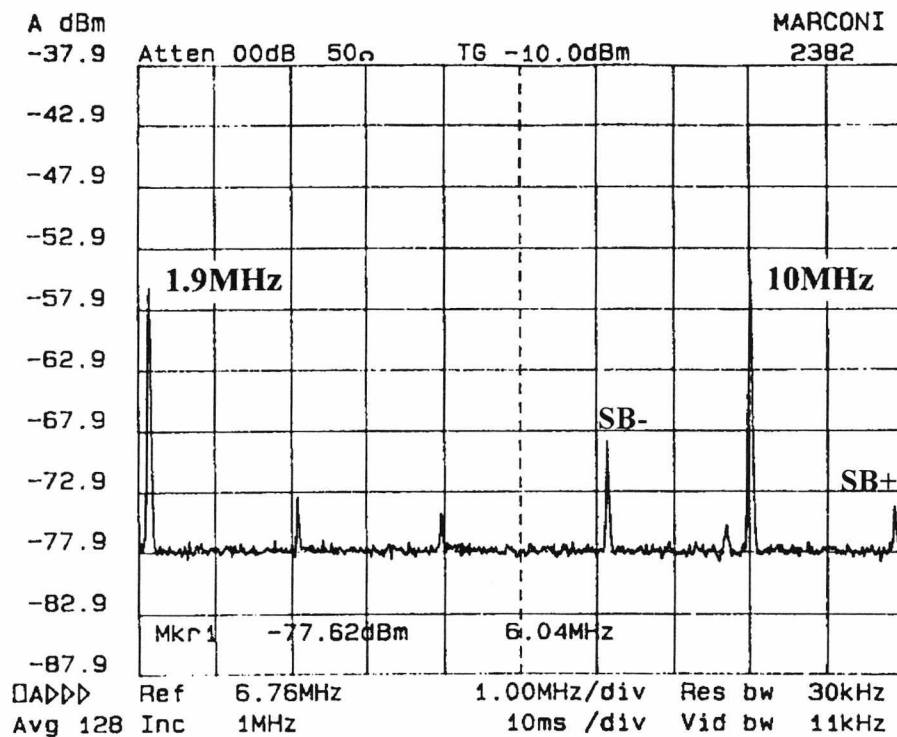
thus confirming that any signals seen stem from the FBG alone.

Figure 4.11 – Typical spectrum analyser trace for 5mm FBG modulated at 1.911 MHz.

To further validate this assumption, the FBG was illuminated directly (via a coupler) without the interferometer present. A signal at 1.911 MHz (plus additional smaller harmonics) was still observed.   Hence the 1.911 MHz signal observed using the interferometric scheme stems from an amplitude variation with, in this case, a measured modulation depth of a few per cent. This amplitude modulation would be superimposed on the heterodyne signal derived from the phase modulation of the optical carrier, and would readily give rise to the observed signal distribution, shown in figure 4.11. This is a typical spectrum analyser trace taken with a 5mm FBG being acoustically excited at 1.911 MHz. The upper and lower sidebands on the 10 MHz carrier are denoted by SB+ and SB-. Figure 4.11 also shows a significant asymmetry in the upper and lower sideband amplitudes. This is an expected consequence of amplitude modulation. This amplitude modulation could be caused by partial modulation of the grating. As previously stated, the close correspondence between the observed and calculated values of the standing acoustic wavelengths in the fibre suggests that the compressional wave hypothesis is correct. With this assumption and given a grating wavelength of ~5mm, it can be seen that at any given time parts of the grating will be in nodes of the standing wave distribution and other parts will be in antinodes and will therefore be subject to modulation by the acoustic field. For regions of the FBG contained with a node there will obviously be no wavelength shift. The optical signal from modulated sections of the FBG will pass through the unmodulated sections, which will act as spectral filters for the back-reflected light from the modulated regions of the grating. To model the effect of an amplitude modulation on the interferometric signals, the constant A in equation 4.9 below (see Appendix A for a full derivation of 4.9) may now be replaced (in the simplest case) with $A[(1-b)+b\cos(\omega t+\varphi)]$ where b is a modulation index and φ is a phase term.

$$I_{OUT} = A\left[1+V(L)\sum_{n=-\infty}^{\infty}J_n(\delta\Phi)\cos[(\omega_C+n\omega_S)t+\phi(t)+\Phi]\right]$$
(4.9)

It can be shown (after some lengthy algebra) that equation 4.9 can be solved for the upper and lower sideband powers, resulting in the following expression.

$$P_{\pm} = [AVb]^2 \cdot \left\{ J_0^2 + J_2^2 + 2J_0 J_2 \cos 2\varphi \right\} +$$
$$[2AV]^2 \cdot [1-b] \cdot \left\{ (1-b) \ J_1^2 \pm bJ_1 \cdot [J_0 + J_2] \cos \varphi \right\}$$

(4.10)

Where $P\pm$ are the upper and lower sideband powers respectively. The arguments of the Bessel functions have been omitted for the sake of clarity, but are the same in equation 4.10 as for equation 4.9. Equation 4.10 shows that the sideband amplitude is symmetric for zero interferometer path imbalance (terms higher than the zeroth-order Bessel function are equal to zero for a zero-valued argument). Equation 4.10 is plotted below in figure 4.12 for a varying path imbalance with a value of b=5% and a Bragg wavelength shift of ~1pm. A value of φ of ~80° was found to give a close correspondence with experimental measurements, shown in figure 4.13.
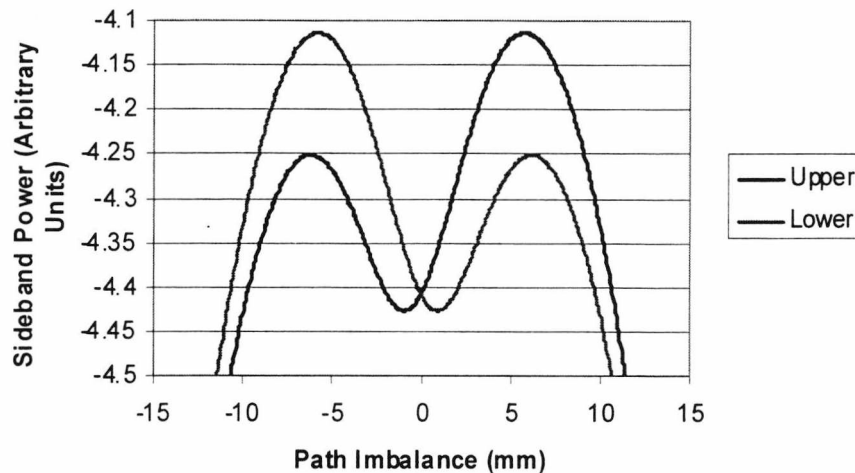
Figure 4.12 Theoretical plot of upper and lower sidebands amplitude as a function of interferometer path imbalance.

The experimental measurements are shown in figure 4.13 where the optical path difference of the psuedo-heterodyne system was varied both in a positive and negative direction. In addition, it is straight-forward to show that for a small b with a linear dependence on acoustic pressure (as was found) that the side-band magnitudes also exhibit a linear dependence with acoustic pressure. It is evident from these data that the FBG exhibits insufficient longitudinal resolution and that the sensitivity of the system is periodic and highly dependent on the position of the focal spot on the fibre. These factors thus preclude this FBG (on its own) from being used as an ultrasonic probe. The

obvious conclusion from these experimental results is that some form of shielding of the bare fibre is necessary in order to achieve point acoustic detection sensitivity and it is this aspect of using FBG's as ultrasonic sensors which is investigated next.
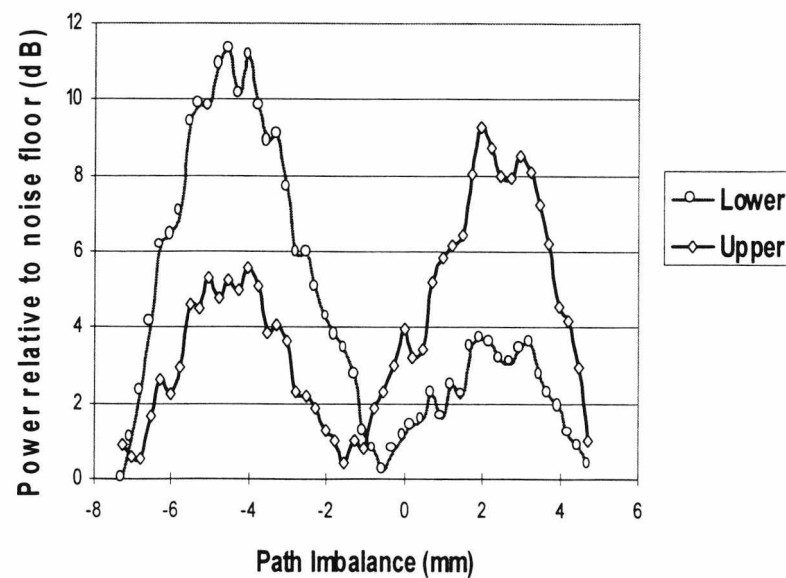
Figure 4.13 Experimental measurements of sideband amplitudes as a function of interferometer optical path difference.

4.3 Desensitisation of the bare fibre

The system discussed previously exhibits a linear response with acoustic pressure (from figure 4.5). However, as discussed earlier, it is clear from figure 4.9 that the FBG on its own cannot be used as a probe since it exhibits insufficient longitudinal resolution. It is relevant to discuss previous situations where acoustic waves have been reported in optical fibres to see if this can provide some indications as to how these waves may be suppressed. One area where acoustic waves in fibres are actually a desirable part of the device operation is in acousto-optic frequency shifters and it is these devices which are described next.

4.3.1   Acousto-optic frequency shifters.

The main elements of a fibre-optic frequency shifter are an optical fibre which in its unperturbed state supports two initially orthogonal optical modes and a means of inducing a travelling perturbation in the fibre in such a way that in the perturbed state optical power can be efficiently transferred between the modes. The travelling perturbation is an acoustic wave generated on the free fibre by an ultrasonic transducer as shown in fig 4.14, taken from [17]. Travelling acoustic waves on a fibre (or rod) broadly fall into three categories : longitudinal, flexural and torsional. In the case of figure 4.14, a torsional travelling wave was acoustically induced on the fibre which effectively gave rise to coupling between the previously orthogonal fibre modes.
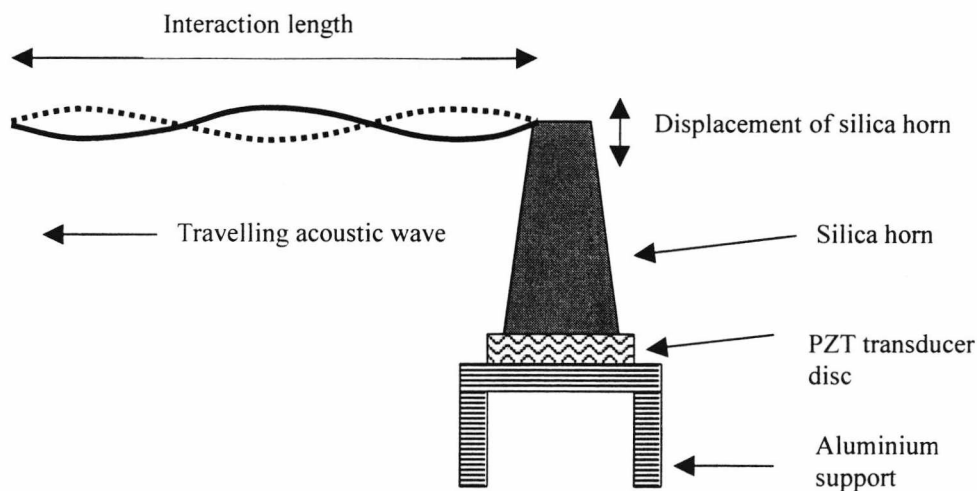
Figure 4.14 – Acoustically induced travelling wave in optical fibre.

The acoustic interaction length of fibre used in the experiment shown in figure 4.14 was approximately 600 mm stripped of its plastic buffer coating, bounded by lengths of unstripped fibre. The lengths of unstripped fibre bounding the acoustic interaction length were found to act as acoustic absorbers. This suggests that some form of discontinuity in the fibre or will serve to suppress the acoustic waves and that simply having some form of coating on the fibre will function as an acoustic absorber.

The fibre used in the experiment of [17] was a highly birefringent fibre. Acoustic excitation was provided by a disc composed of the piezoelectric material lead zirconate titanate (PZT). The acoustic energy from the transducer was transmitted to the fibre by a silica horn which also served to mechanically increase the acoustic excitation amplitude. In figure 4.14, the maximum coupling between the orthogonal optical modes occurs when the spatial period of the acoustically-induced fibre perturbation matches the beat length between the modes. The net result of the travelling perturbation in the fibre is to cause a frequency shift in the light coupled between the modes equal to the frequency. of the acoustic perturbation. Altering the acoustic drive frequency allowed the mode coupling to be optimised by ensuring that the acoustic wavelength matched the fibre mode-mode beat length. This was found to occur at approximately 3.2 MHz, hence giving rise to an optical frequency shift at this frequency. As the acoustically-induced stress distribution travels along the fibre the phase of the coupled light is advanced or retarded depending on whether it was initially on the fast or slow axis of the fibre and also depending on the relative directions of optical and acoustic propagation. The proportion of the initial optical power that is frequency shifted depends on the interaction length and also on the acoustic amplitude. An important prerequisite for effective mode-mode coupling due to the travelling acoustic wave is that there must be some degree of intrinsic fibre birefringence. This phenomenon has also been demonstrated in single mode fibre [18]. Here bend-induced birefringence in ordinary single-mode fibre was induced by coiling the fibre around a hollow aluminium cylinder, the cylinder being acoustically excited by a piezoelectric transducer on the top of the cylinder. Linearly polarised light launched into one of the fibre axes was acoustically coupled into the orthogonal axis and frequency shifted. These devices can also function as tunable filters, switches and modulators. When they are used as single-sideband frequency shifters, mode convertors and filters are necessary to separate the residual carrier from the shifted signal and give a single-mode output. Based on this discussion of acousto-optic frequency shifters, it is apparent that the longitudinal resolution of our sensor should be improved by an appropriate desensitisation of the optical fibre to the acoustical field by having some form of coating or sleeving on the fibre to suppress the acoustically-induced travelling waves. To achieve this, the fibre was initially coated with acrylic compounds (of diameters < 1mm) and various resins

(including resin mixed with tungsten powder which is known to attenuate acoustic fields [5]), but leaving a 1mm gap in the vicinity of the FBG. The acrylic resin used was a UV cured polymer used as a general-purpose laboratory optical adhesive. The second coating used was a mixture of epoxy and tungsten powder, the ratios of epoxy to tungsten being approximately 20:80 % by weight. These methods were not entirely successful. Firstly, it was evident that, although attenuated, the ultrasound could still significantly penetrate the coating, and secondly, extended periods of time under the acoustic pressures used here (which are in fact relatively small compared to some medical applications of ultrasound) resulted in the coatings being "cleaned off" the fibre.

A more successful approach for desensitisation was to jacket the fibre with PVC sleeving. Here, sleeving of outer diameter 0.88mm was used in which the internal spacing between the bare optical fibre and the sleeving was ≈50μm. A gap in the PVC allowed ≈1mm of FBG to be exposed to the acoustic field. The results of a longitudinal scan and a lateral scan of the acoustical focal spot are shown in figures 4.15 and 4.16, respectively. As may be seen, the improvements in spatial resolution are significant. In addition, by moving the 1mm gap in the PVC a few millimetres to one side of the FBG, the system response fell to near noise level indicating that the acoustic modes in the fibre were significantly attenuated by the PVC sleeving jacket. This result is encouraging if a probe containing more than one FBG multiplexed on to the same fibre is to be designed.
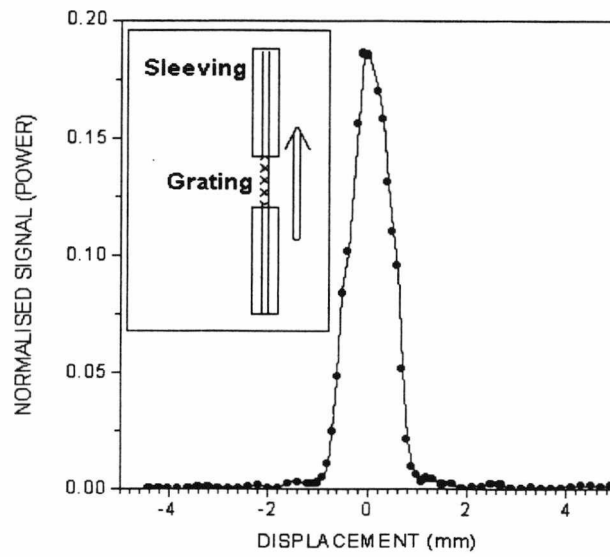
Figure 4.15 - Longitudinal scan of acoustic focus
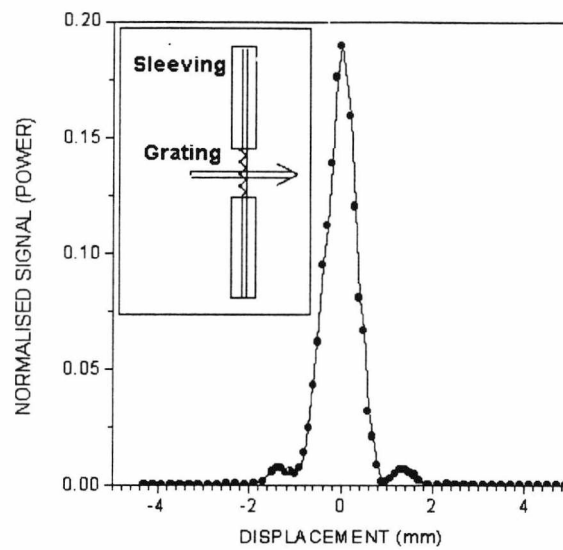
Figure 4.16 – Lateral scan of acoustic focus

This data compares favourably with the diameter of the main diffraction maximum of the transducer. Figure 4.17 shows the detected magnitude of one of the side-bands

(normalised by its corresponding carrier signal) as a function of the acoustical pressure incident on the grating.
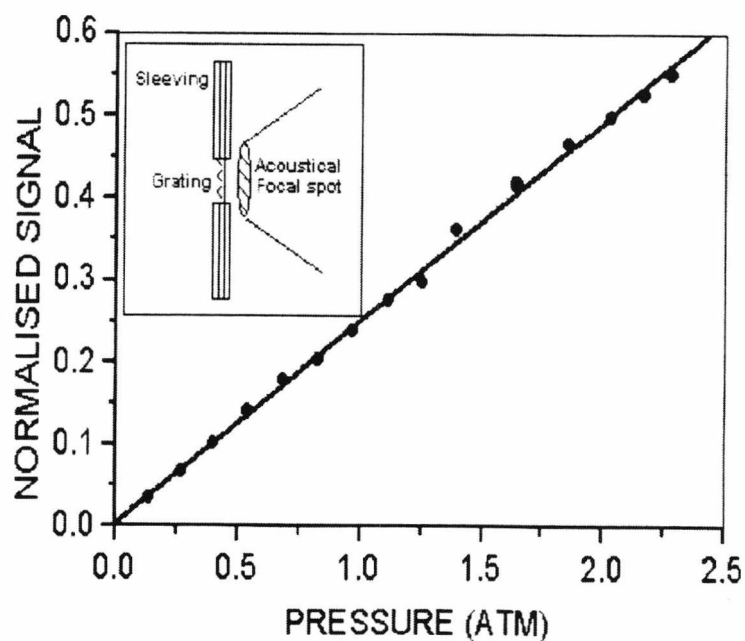
Figure 4.17 – Shielded FBG Linear response with acoustic pressure

It is evident from 4.17 that the system response is linear and (for this probe) the noise-limited pressure resolution was $\approx 4.5 \times 10^{-2}$ Atm / $\sqrt{Hz}$, (or 4500 Pa/$\sqrt{Hz}$)

4.4   Investigation of 1mm length Grating

From the previous experimental results, it is apparent that the grating length should be made smaller than half the acoustic wavelength in fused quartz in order for the grating to be subject to an approximate uniform strain. To demonstrate this, a standard 5mm long grating had small pieces of the grating removed from one end until approximately only 1mm of grating was remaining. This was achieved, (albeit crudely) by using a surgical scalpel blade and a steel rule to measure along and then cleave sections from the initially 5mm long grating. As the position of the grating had been marked on the fibre during manufacture then this was relatively simple to perform accurately. The initial grating characteristics were a reflectivity of ~ 90% and a FWHM of ~0.2 nm at a

peak wavelength reflectivity of 820 nm. As each piece was removed the system response to the ultrasonic field using the shortened grating was recorded. The most apparent effects were the dramatic decrease in the 1.911 MHz signal (which falls to RF pickup levels) along with the more symmetric side-band magnitudes. In addition, despite the expected decrease in the back-reflected light intensity as the grating is shortened, it was interesting to note that there was an initial significant increase in the side-band magnitudes. Based on the stationary wave model, it seems likely that in using long gratings, sections of the grating may well have been modulated in antiphase with each other. The interference signals originating from these sections would also have been in antiphase and so a cancelling out effect occurs. As the grating is shortened this effect lessens, resulting in the observed increase in side-band magnitude.

4.5 Combined temperature and acoustic pressure measurement

In many applications, FBGs suffer from the problem of discrimination between temperature and strain induced wavelength shifts. In this application the separation is possible due to the radically different frequency regimes of the two parameters (MHz for ultrasound induced strain and ~DC for temperature). The nominal wavelength of light reflected from an in-fibre grating is directly proportional to temperature. To measure this wavelength and hence temperature the monochromator/CCD arrangement shown in figure 4.18 was used.
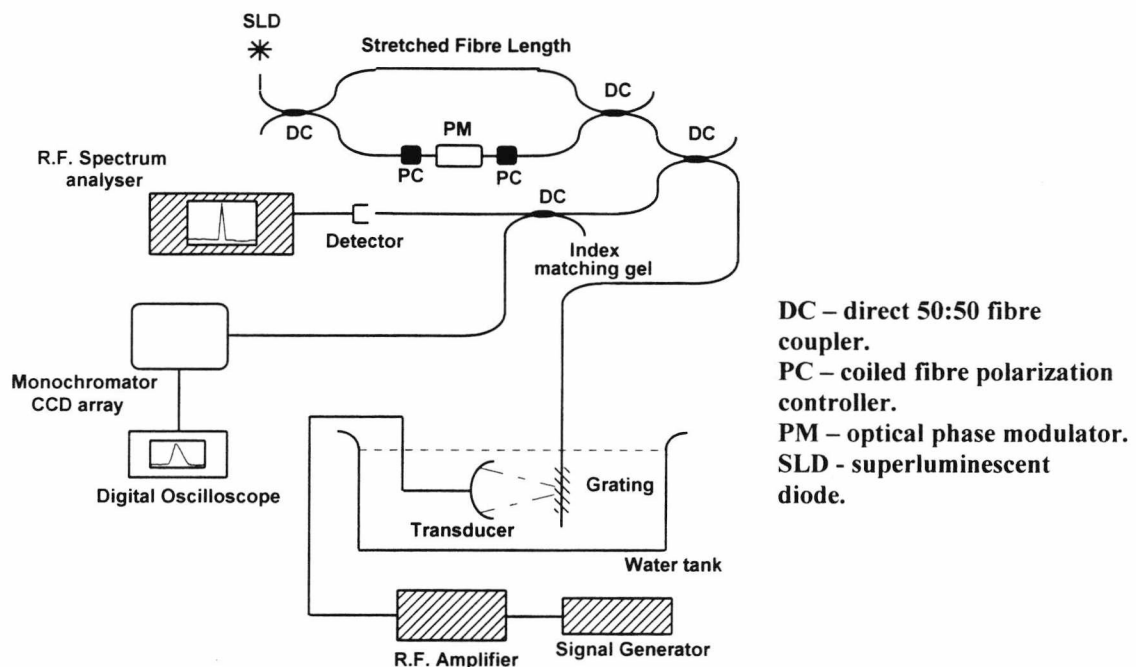
Figure 4.18 – Simultaneous measurement of temperature and acoustic pressure

The experimental arrangement of figure 4.18 is a simple modification of the initial experimental arrangement shown in figure 4.1. The pixel voltages obtained from the CCD array represent the intensity vs. wavelength profile of the FBG convolved with the intrinsic instrument broadening of the monochromator. A blazed diffraction grating with 1200 lines mm^{-1} was used, arranged so that light from the sensor grating was incident at 45°. This configuration gave an intrinsic resolution of 0.3nm, about half the width of the FBG profile. This is a relatively poor resolution compared with an optical spectrum analyser but for this application only the shifts in the peak wavelength are

important. The light was focussed onto the CCD with a 50 cm focal length lens giving a dispersion of approximately 21pm per pixel. The peak wavelength can be determined to a resolution beyond that of the CCD by employing numerical methods. In this case the raw data from the CCD was low pass filtered using Fourier techniques to remove the higher frequency noise, and then interpolated to find the wavelength of maximum intensity and hence the peak of the FBG. To find the accuracy of this system the FBG was held at constant temperature and 60 profiles from the CCD were analysed. The standard deviation of the calculated temperatures thus represents the temperature resolution and in this case was found to be ~0.2 °C. Figure 4.19 is the peak FBG wavelength dependence with temperature, clearly showing a linear relationship.
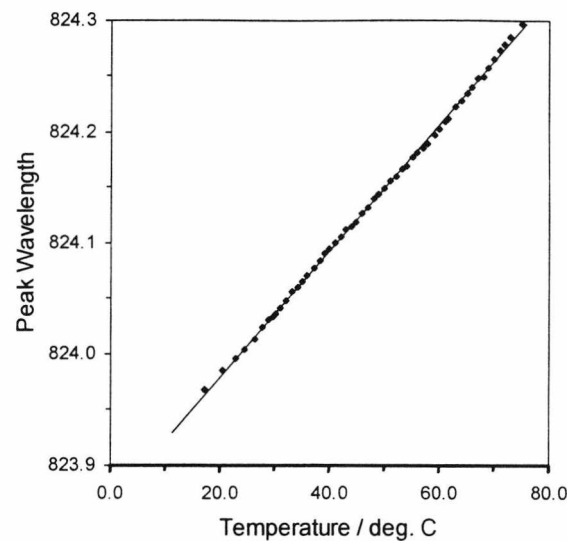
Figure 4.19 – FBG peak wavelength dependence with temperature

The r.m.s deviation from linearity of the data suggests a measurement error of ~0.4°C. It should be noted however that at the higher temperatures there was considerable fluctuation in the temperature of the oven limiting the accuracy of the thermocouple measurements to several tenths of a degree. The true temperature resolution should therefore be closer to the value of 0.2°C obtained above for the constant temperature case. The ability to simultaneously measure both temperature and acoustic pressure is of primary importance in therapeutic applications of ultrasound [6,8], specifically the

use of focussed ultrasonic beams in the hyperthermic treatment of solid tumours [7] where accurate measurements are important if the therapy is to be monitored for its effectiveness and also so that damage to healthy tissues is avoided.

4.6 Construction of a quasi-distributed ultrasonic sensor.

An obvious extension of the previous experimental results was to attempt to construct an array of FBGs and to assess the degree of cross-talk between them when the acoustic focus was scanned longitudinally along the fibre. The demultiplexing and optical detection system is shown below in figure 4.20.
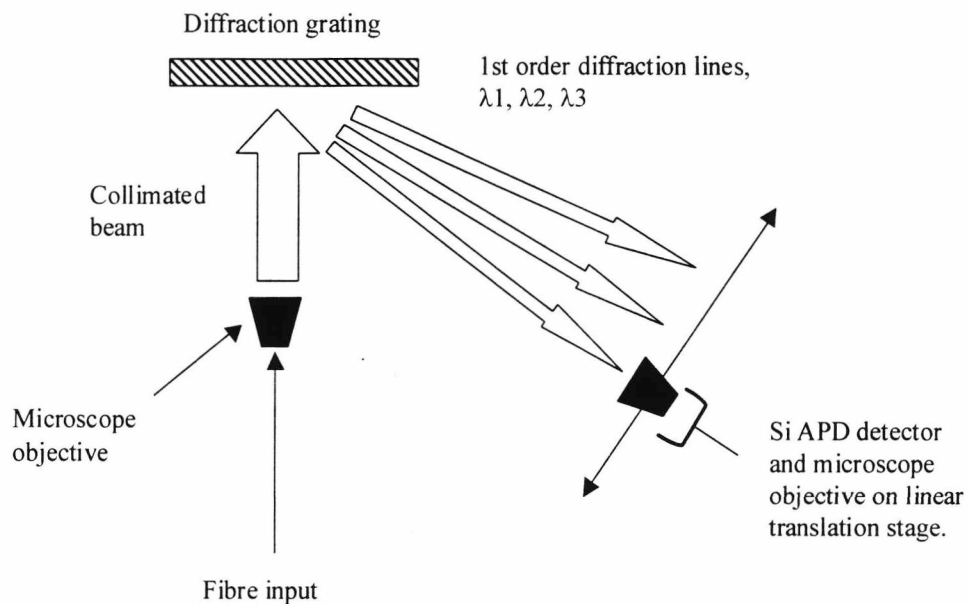
Figure 4.20 – FBG array demultiplexing system

The psuedo-heterodyne system was used to interrogate an array of 3 FBG's, the bare fibre between each grating being shielded with short lengths of the PVC tubing used in previous experiments. The array consisted of 3 separate 5mm long FBGs separated by 2 cm. Each FBG had a peak reflectivity of ~90 % at the FBG operating wavelengths of 824, 827.4 and 829 nm respectively with a FWHM of ~0.2 nm. This relatively close wavelength spacing corresponded reasonably well with the SLD peak intensity of 820 nm, hence the backreflected signals from each FBG were of similar intensities. There was no need to splice the FBGs together as they had all been written into the same piece of fibre. As the FBG array with shielding was rather fragile some form of mounting was required that would not significantly affect the acoustic field distribution and yet would be strong enough to support the array while the acoustic focus was scanned longitudinally along the fibre. The mounting arrangement used is shown below in figure 4.21.
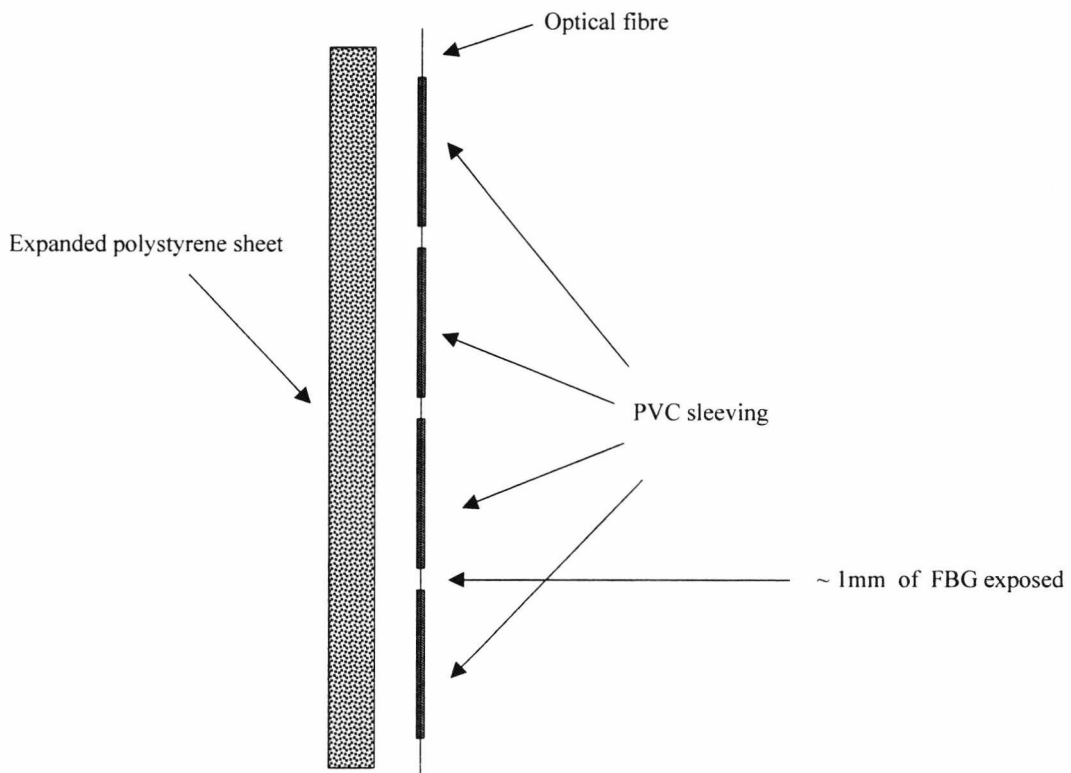
Figure 4.21 - Mounting arrangement for 3 FBG array.

The array was loosely secured to the polystyrene sheet using small loops of fine wire (not shown for sake of clarity) and the acoustic focus scanned along the array length. However, due to untimely and unrepairable failure of the RF amplifier used to drive the ultrasonic transducer it was not possible to continue this line of experimental investigation to the desired depth. With some modifications to the acoustic shielding, the array could potentially be used as a distributed medical sensor in hyperthermic applications of ultrasound.

4.7 Conclusions and further experimental work

The use of FBGs to successfully detect MHz ultrasonic fields has been demonstrated with a noise-limited pressure resolution of 4.5 kPa/√Hz. However, experimental results show conclusively and the previous discussion of travelling acoustic waves in acousto-optic fibre frequency shifters suggests that point acoustic detection sensitivity cannot be achieved without some form of acoustic shielding on the bare fibre to avoid the transmission of acoustic compressional waves from elsewhere in the fibre to the FBG. The acoustic shielding used in these experiments was relatively crude compared to the results of previous investigations [11, 12, 13]. In [12], a multilayered coating composed of a low Young's modulus silicone polymer (~ few 100 μm thickness) coated with a layer of nickel was found to be particularly effective in reducing the fibre acoustic sensitivity. This suggests that a more sophisticated quasi-distributed array could be constructed as shown below in cross-section in figure 4.22 and longitudinally in figure 4.23
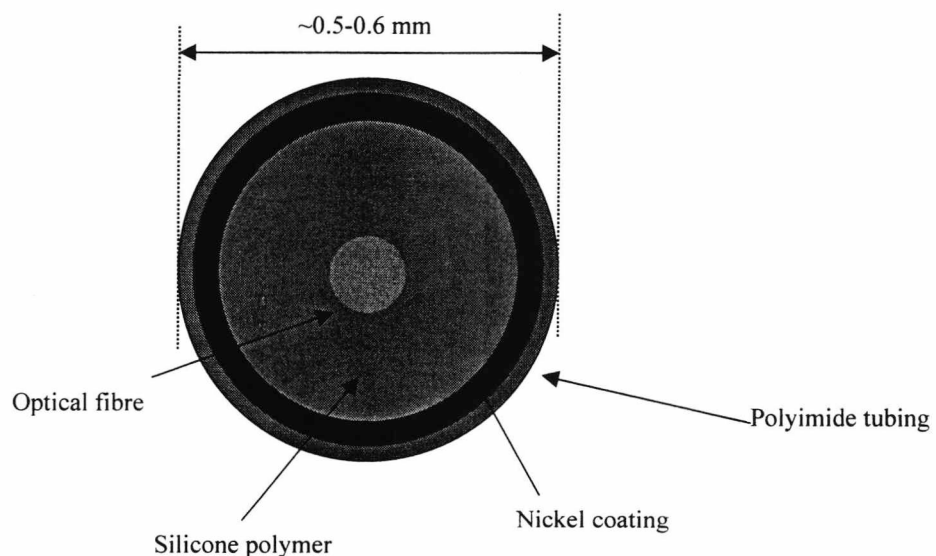
Figure 4.22 – Cross-section of improved FBG acoustic sensor array.
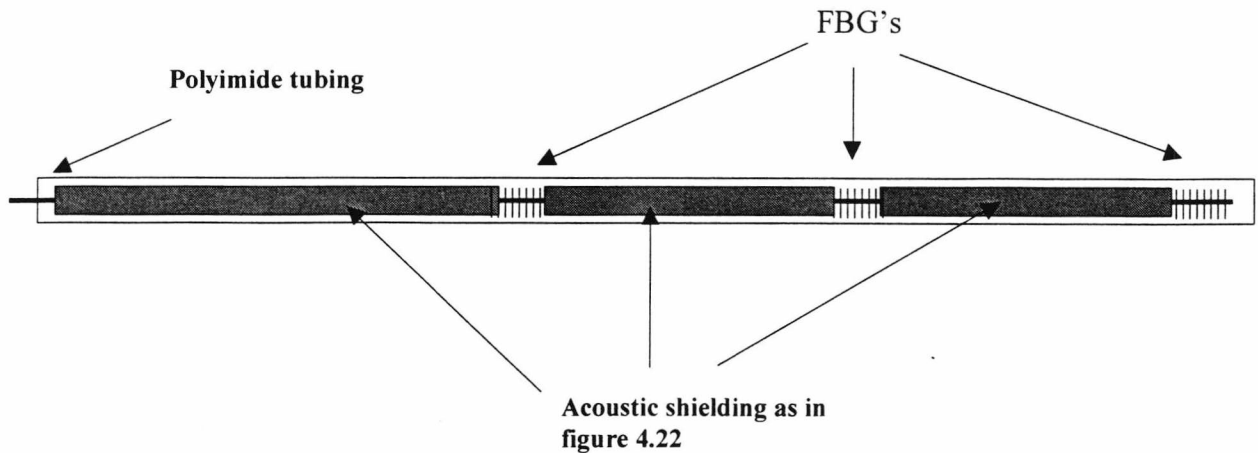
Figure 4.23 – Longitudinal arrangement of improved FBG array

The polyimide tubing would provide some degree of mechanical strength to the array as well as ensuring that the various array components did not come into contact with any substances which could chemically corrode the array, such as may be found in-vivo. The high Young's modulus of the polyimide tubing allows thin (~10-20 μm) tubing to be used which would not significantly effect the acoustic detection sensitivity of the array. This assumption was verified by a relatively simple experiment in which a single FBG was sheathed with a length of the tubing and the FBG response measured and compared to the unsheathed case. No measurable decrease in acoustic detection sensitivity was observed. Sterilisation of such an array is obviously important in medical applications where the sensor may be used on several different patients. The high melting point (~350-400°C) of the polyimide would allow sterilisation of the sensor in the steam autoclaves currently used in hospital operating theatres. However, there may be some difficulties encountered with the use of the silicone polymer as part of the acoustic shielding – the melting point of this polymer will be considerable lower than that of the polyimide. Careful choice of a more refractory polymer for the acoustic shielding would overcome this potential difficulty.

The improvements in the system response using a short grating are significant. However, several points should be noted. Firstly, by shortening the grating the grating reflectivity is dramatically reduced (in this case by a factor of well over 100) as well as increasing the grating bandwidth, hence the noise-limited pressure resolution is reduced. For applications involving high power ablation where pulsed ultrasound intensities can be several hundreds or even thousands of Wcm^{-2}, the resolution obtained is sufficient. For physiotherapy treatments where the acoustic intensities may vary from about 0.2 to 2 Wcm^{-2}, an improvement in the noise limited pressure resolution may well be necessary.

Secondly, based on the stationary wave model, a limiting factor in the successful performance of the grating is that its length should be less than half the acoustic wavelength in fused quartz. This sets an upper limit on the incident acoustic frequency which can be measured. Fortunately, frequencies of between 500kHz and 4MHz are generally used in most medical applications of ultrasound which implies that the grating lengths should be no greater than about 0.5mm for the highest frequency. Again, such lengths are available. In the case of lithotripsy, multiple frequency components may be generated. However, as the acoustic field traverses several cm of tissue, the higher order modes are in general significantly attenuated. Hence, in certain cases, acoustic fields of only a few MHz may be of importance.

Thirdly, as previously mentioned, more sophisticated techniques (entailing multiple coatings) for desensitising optical fibres have been reported. In the experiments performed here fluctuations in the r.f. power (to the transducer) were observed as the FBG sensor was moved around in the vicinity of the focal spot. This was especially evident when the focal spot was incident on the PVC sleeving and is evidence for back-reflections and scattering of the acoustical field by the sensor. Obviously, reducing the dimensions of the shielding by using these multiple coatings will greatly minimise this scattering. In addition, it is worth mentioning again that if the acoustic modes in the fibre can be significantly attenuated using these coatings (as found using the sleeving) then in principle it should be possible to multiplex FBGs onto the same fibre with little or no acoustic cross-talk between them. A further point entails the grating acting as an acoustic probe in "smart structure" design. Here acoustic emission is monitored and

gives information about twinning, dislocation motion, cracking etc. in the material. The response of the grating to multi-frequency bursts needs to be investigated. However, typical frequency spectra range from about 0.1 to 1.0 MHz and so readily available gratings of lengths 1 to 2mm may (in principle) be used.

The brief discussion of acousto-optic frequency shifters in this chapter illustrates that in some instances, the presence of travelling acoustic waves in an optical fibre is required for the correct operation of the device. The converse is true in the case of using FBGs as ultrasonic sensors, and some form of acoustic damping is required if point detection sensitivity is to be obtained. Because the FBG sensor is localised in the fibre, evidence for this can be seen in the longitudinal scans, which demonstrate that bare fibres containing an FBG do not display point ultrasonic detection sensitivity. Instead, the entire unshielded fibre acts to transmit the travelling ultrasonic wave to the FBG. In some other interferometric and polarimetric schemes, the sensing element is the entire fibre length [14,15,16]. Sensing is therefore not localised and so in performing longitudinal scans, evidence for the stationary waves may not be readily observable.

To conclude, it has been demonstrated that a Bragg grating may function effectively as a point ultrasonic probe with mm resolution if:

(a) The grating length is small (less than half the acoustic wavelength in fused quartz).

(b) The fibre is appropriately desensitised using some form of acoustically damping coating. A distinct advantage that FBGs have over other forms of sensor are their potential to also simultaneously measure temperature.

References:

1. JACKSON, D.A., KERSEY, A.D., CORKE, M., JONES J.D.C.: 'Pseudo-heterodyne detection scheme for optical interferometers' Electronics Letters, **18,** 1982 pp. 1081-1083

2. PRESTON, R.C., BACON, D.R., LIVETT, A.J., RAJENDRAN, K., 'PVDF membrane hydrophones performance properties and their relevance to the measurement of the acoustic output of medical ultrasonic equipment.', Journal of Physics E: Scientific Instrumentation, **6,** 1983, pp 786-796.

3. KINO, G.S.: 'Acoustic Waves : Devices, Imaging and Analogue Signal Processing', Prentice-Hall signal processing series, ISBN/ISSN : 0130030473.

4. KOSSOFF, G.: 'Analysis of focusing action of spherically curved transducers' , Ultrasound Medical Biology, **5,** 1979, pp 359-365

5. LEES, S., GILMORE, R.S., KRANZ, R.P.: 'Acoustic properties of Tungsten-Vinyl Composites', IEEE Transactions on Sonics and Ultrasonics, Vol. SU-20, No. 1, Jan. 1973.

6. NCRP 1983 'Biological effects of ultrasound: mechanisms and clinical implications', report 74 of the National Council of Radiation Protection and Measurements.

7. SANGHVI, N.T., FRY, F.J., FOSTER, R.S., PHILLIPS, M.H., SYRUS, J., ZAITSEV, A.V., HENNIGE, C.W.: 'Noninvasive surgery of prostate tissue by high-intensity focused ultrasound', IEEE Trans. Ultrasonics, Ferroelectrics and Frequency Control, **43,** 1996, pp. 1099-110.

8.   FIELD, S.B., HAND, J.W., (ed) 'An Introduction to the Practical Aspects of Clinical Hyperthermia', (London: Taylor and Francis), 1990.

9.   RAO, Y-J., WEBB, D.J., JACKSON, D.A., ZHANG, L., BENNION, I., 'In-Fibre Bragg Grating Temperature Sensor System for Medical Applications', Journal of Lightwave Technology, 15, No. 5, May 1997, pp 779-784.

10.   HYNYNEN, K., EDWARDS, D.K., 'Temperature Measurements during ultrasound hyperthermia', Medical Physics, 16, No. 4, Jul/Aug. 1989, pp 618-626.

11.   LAGAKOS, N., HICKMAN. R.T., COLE J.H., BUCARO J.A., 'Optical fibres with reduced pressure sensitivity' , Optics Letters, 6, No. 9, Sep. 1981, pp 443-445.

12.   LAGAKOS, N., BUSH, I. J., COLE J.H., BUCARO J.A, 'Acoustic Desensitisation of single-mode fibres utilizing nickel coatings', Optics Letters, 7, No. 9, Sep. 1982, pp 460-462.

13.   LAGAKOS, N., KU, G., JARZYNSKI, J., COLE J.H., BUCARO J.A, 'Desensitization of the ultrasonic response of single-mode fibers', Journal of Lightwave Technology, 5, 1985, pp 1036-1039.

14.   DE PAULA, R.P., FLAX, L., COLE, J.H., BUCARO, J.A., 'Single mode fiber ultrasonic sensor', IEEE Journal of Quantum Electronics, 18 pp. 680-693, 1982.

15.   CHAN, H.L.W., CHIANG, K.S., PRICE, D.C., GARDENER, J.L., 'The characterisation of high frequency ultrasonic fields using a polarimetric optical fiber sensor' Journal of Applied Physics, 66 pp. 1565-1570, 1989.

16.   CHIANG, K.S., CHAN, H.L.W., GARDENER, J.L., 'Detection of high frequency ultrasound with a polarisation maintaining fiber', Journal of Lightwave Technology, 8, pp. 1221-1227, 1990.

17.   BERWICK, M, PANNELL, C.N., RUSSELL P. ST. J, JACKSON, D.A.: 'Demonstration of birefringent optical fibre frequency shifter employing torsional acoustic waves', Electronics Letters, **27**, No.9, pp 713-715, 1991.

18.   JI, J., UTTAM, D., CULSHAW, B.: 'Acousto-optic frequency shifting in ordinary single-mode fibre', Electronics Letters, 22, No.21, pp 1141-1143, 1986.

Chapter 5

Use of Low-Finesse Interferometric Cavities as Ultrasonic Sensors

5.1   Introduction

An optical fibre Fabry-Perot sensor is an interferometer where the sensing element is an optical cavity defined by two reflecting surfaces. The applied measurand, an acoustic field in this case, modulates the optical path length of the cavity, resulting in a phase change which is observable as a change in the reflected or transmitted optical power. Cavity-based sensors may be divided into extrinsic and intrinsic types. In an extrinsic sensor, the cavity is external to the fibre and may be composed of a range of different materials. An intrinsic sensor is one where the cavity is formed within the fibre itself by partially reflective internal mirrors. A common approach to fabricating an intrinsic cavity sensor is to sputter thin films of titanium dioxide (TiO_2) onto the cleaved ends of a single-mode fibre [1]. The cleaved ends are then fusion spliced with a spacer to form a cavity, the spacer being composed of a short length of hollow-core fibre. The use of in-fibre Bragg gratings also provides a means of forming an intrinsic cavity, where the cavity length can be several tens of cm [2,3]. The use of FBG's in forming a cavity has the added advantage of not affecting the mechanical strength of the fibre, which may be of importance in applications where the sensor is permanently embedded in a structural member. Sensor strength is important in applications where the fabrication process of the structural member can lead to mechanical failure of the sensor if the sensor is not sufficiently robust. Of particular interest in this chapter is the experimental examination of low-finesse extrinsic cavities formed in a thin (50 µm) polymer film.

The impetus for this approach comes from previous work [4,5] investigating the potential of such film-based cavities for the detection of ultrasonic fields. In [4,5], the detection scheme involved the use of a thin film of polyethylene teraphthalate (PET) as the acoustic sensing element mounted at the end of a multimode fibre. Before discussing the approach adopted in this chapter towards constructing an acoustic sensor based around a low-finesse extrinsic Fabry-Perot cavity it is worth examining previous approaches to the problem to determine whether there is any scope for improvement in terms of increased acoustic sensitivity. The most well-developed approach has been documented in [4,5] and it is this approach which will be examined and the experimental results reported. This will in turn provide a reference ultrasonic detection sensitivity for the experimental results quoted in this chapter.

5.2 Interaction of a polymer film cavity with an ultrasonic field.

Figure 5.1 shows a schematic of a Fabry-Perot polymer film ultrasound transducer, such as the one described in [4,5]. A discrete polymer film such as PET (polyethyene teraphthalate) is used as the sensing element. The thickness of the polymer film is typically of the order of 50μm.
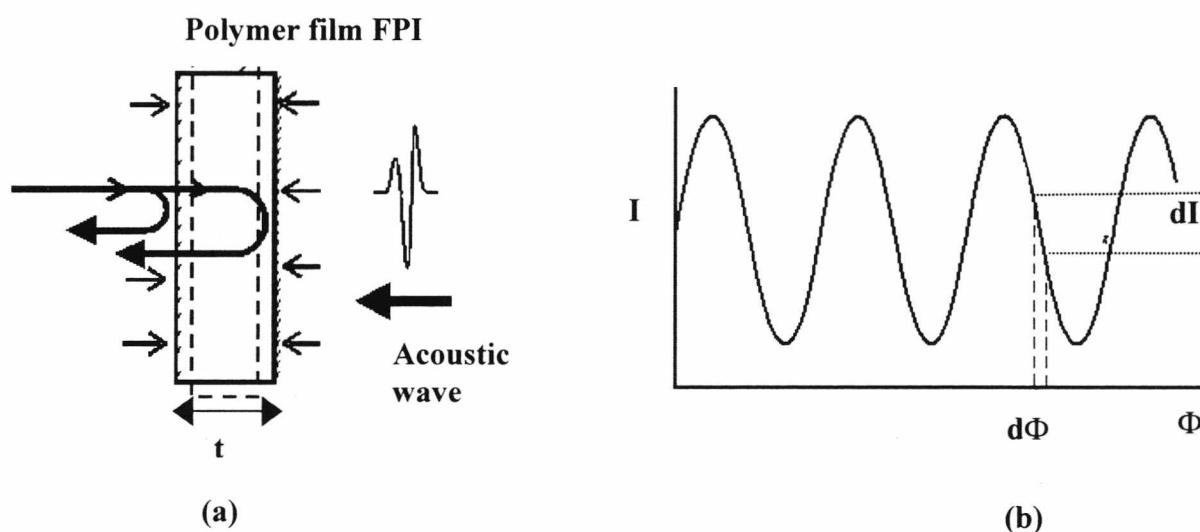
Figure 5.1 Fabry-Perot polymer film ultrasound sensor and (b) low finesse Fabry-Perot interferometer transfer function.

The "mirrors" of the interferometer can be formed by depositing metallic or dielectric reflective coatings or left uncoated with the refractive index mismatch between the film and surrounding media providing the necessary Fresnel reflections. The transduction mechanism comprises two processes. Firstly, external acoustic pressure is linearly converted to a change in the optical thickness of the film (figure 5.1(a)). Secondly, the resulting optical phase shift $d\Phi$ is converted to an intensity modulation dI. (figure 5.1 (b)) through the intensity-phase transfer function of the interferometer. The latter is not strictly linear although by setting the bias point of the interferometer to be at quadrature, both the acoustic detection sensitivity and the linearity will be maximised.

Note also that figure 5.1(b) shows the raised transfer function characteristic of a two beam interferometer, such as a Mach-Zehnder or Michelson interferometer. In a Fabry-Perot cavity, this occurs when the reflectivities of the cavity mirrors are small (<10%). In this case the contribution of multiple reflections to the reflected fringe system can be neglected and the interferometer becomes one of low finesse, sometimes known as a Fizeau interferometer [5]. Whilst higher sensitivity can be achieved using high reflectivity low absorption dielectric mirrors to create a high finesse Fabry-Perot cavity, there are several important practical advantages to the low finesse configuration. It offers reasonable detection sensitivity (comparable to PVDF transducers) and a useful linear phase range with the detection of phase shifts up to 0.8 radians achievable with a linearity of better than 10% [4]. An optimum fringe visibility close to unity can be achieved with a relatively wide range of mirror reflectivities.

The use of a thin polymer film as an acoustic sensing element has a number of advantages over other forms of extrinsic (and intrinsic) acoustic sensor. Because the polymer film itself is the interferometer and has a short optical path length, it exhibits a low sensitivity to spurious environmental thermal and pressure fluctuations. The reflective surface is formed by the Fresnel reflection coefficients arising from the difference in refractive index between the polymer and the water in which the sensor is examined. A film thickness of a few tens of microns implies that a long-coherence length source is not needed and that low-coherence heterodyne interrogation techniques could be used. Also, the low Young's modulus (4-5 GPa) of many polymers compared to that of fused silica (~72 GPa) will give rise to an enhanced acoustic sensitivity

compared to the type of intrinsic fibre sensors discussed previously. As the acoustic impedance of many polymers is comparable to that of water, the frequency response of polymer film sensors should be uniform. As the active area of the sensor is defined by the core diameter of the fibre, small active areas are possible. This allows a high spatial resolution and a low directional sensitivity to be achieved.

The following analysis is taken from [4]. The strain due to a normally incident acoustic field produces a change dl in the thickness l of the polymer film. This thickness change results in a phase change $d\Phi$, which gives the following expression relating the thickness and phase changes :

$$d\Phi = \frac{4\pi n dl}{\lambda} \tag{5.1}$$

where n is the refractive index of the polymer film and λ is the source wavelength.. The change in film thickness is given by :

$$dl = \int_0^l \frac{P_T(x,t)}{E} \cdot dx \tag{5.2}$$

Where E is the Young's modulus of the polymer. The quantity $P_T(x,t)$ represents the spatial variation of the pressure across the thickness of the sensing film and is the sum of the component of the incident acoustic wave that is transmitted into the polymer film and subsequent reflections at the boundaries of the film. These reflections arise as a result of the differences in acoustic impedance between the polymer and the surrounding medium. It can be shown [4] that for a rigid-backed sensing film such as investigated here, the acoustic sensitivity is given by the following expression:-

$$\frac{d\Phi}{P_0} = \frac{4n}{\lambda}\frac{\lambda_a}{E}\sin\left(\frac{2\pi l}{\lambda_a}\right) \tag{5.3}$$

where P_0 is the amplitude of the acoustic field, n is the polymer refractive index, E is the Young's modulus of the polymer film and λ, λ_a are the optical and acoustic wavelengths.

As the acoustic wavelength here (~750 μm) is significantly greater than the film thickness l (~50 μm) the expression given in (5.3) is simplified and reduces to:-

$$\frac{d\Phi_0}{P_0} \approx \frac{8\pi nl}{\lambda E} \qquad (5.4)$$

Equation (5.4) shows that the acoustic sensitivity can be maximised by having a material with a low Young's modulus and is frequency independent for the acoustic wavelength greater than the film thickness i.e $\lambda_a \gg l$, where a small angle approximation can be made for the *sin* function in equation 5.3. This is a valid assumption for acoustic wavelengths of ~750 μm, i.e. up to ~2 MHz in frequency.

5.3   Low coherence interrogation of a low-finesse cavity.

The transfer function of a low-finesse cavity illuminated by a low-coherence source can be readily approximated by an ordinary two-beam transfer function if the reflectivity of the cavity surfaces is low enough for higher-order reflections to be neglected. In this case the resultant intensity is given by the following expression:-

$$I_0 = I_1 + I_2 + 2\sqrt{I_1 I_2}\, \cos\Phi \qquad (5.5)$$

where I_0 is the resultant intensity from the reflections I_1, I_2 from the two sides of the film, and Φ is the phase difference arising from the optical path length difference between the two reflections. For a PET film of refractive index n (=1.6), the intensities I_1, I_2 can be written in terms of the Fresnel reflection coefficients and the incident intensity I, and are given by:-

$$I_1 = Ir_1, \qquad I_2 = I(1 - r_1)^2 r_2 \qquad (5.6)$$

where :-

$$r_1 = \left(\frac{n - n_1}{n + n_1}\right)^2 \qquad r_2 = \left(\frac{n - n_2}{n + n_2}\right)^2 \qquad (5.7)$$

For situations where a PET film is surrounded by water, $n_1 = n_2 = 1.33$, and $r_1 = r_2 \sim 0.0085$. Hence the assumption that higher-order reflections can be neglected is justified and the two-beam approximation is valid for this case.

5.4   Previous investigations of a low-finesse polymer film cavity.

In [4,5,6], the sensor was constructed as shown in figure 5.2.
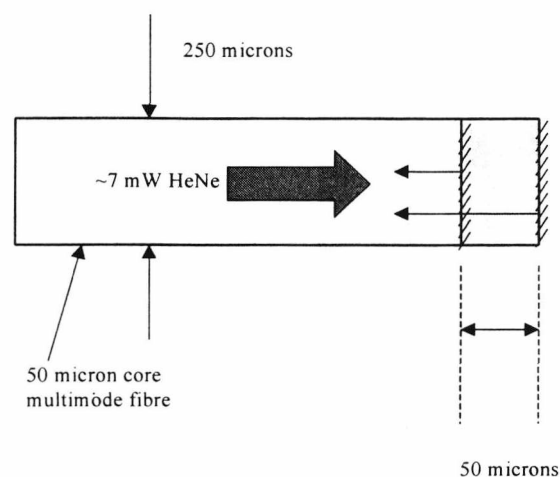
Figure 5.2 Fabry-Perot acoustic sensor based on thin polymer film

The sensor in figure 5.2 consisted of a 50 μm PET film disc 0.25 mm in diameter bonded to the cleaved end of a multimode fibre using an ultraviolet curable adhesive. To increase the fringe visibility and hence the acoustic detection sensitivity the polymer film was aluminised on both sides, one side being 100% reflective (or as close as achievable) and the other side aluminised to $\sim$ 40% reflectivity. Interrogation of this sensor to determine the ultrasonic detection sensitivity consisted simply of monitoring the intensity of the backreflected light from the sensor. This method of interrogation relies on the interferometer being as close to the quadrature point as possible to maximise the detection sensitivity and also the sensor linearity. The transfer function around the quadrature point (figure 5.1(b)) is

linear within ~10% over a relatively large phase change (~0.8 radians) [5]. In [4,5], operation at quadrature was determined by trial and error. A number of sensing films were prepared from different areas of a sheet of PET. The slight manufacturing variations in thickness over the area of the sheet produced a range of phase biases and hence a range of sensitivities. The sensor that gave the highest sensitivity was assumed to have a thickness that resulted in a phase bias closest to quadrature.

5.5 Results from previous investigations.

5.5.1 Noise Limited Pressure Resolution.

From [4,5,6], the measured noise limited acoustic detection sensitivity of the polymer film hydrophone was 10 kPa in a 25 MHz bandwidth, which equates to a detection sensitivity of 2 Pa/√Hz. This figure is comparable to the sensitivity obtainable from a commercially available PVDF transducer, as is shown in table 5.1 later in this chapter.

5.5.2 Linearity

The linearity obtained from [6] is shown below in figure 5.3.
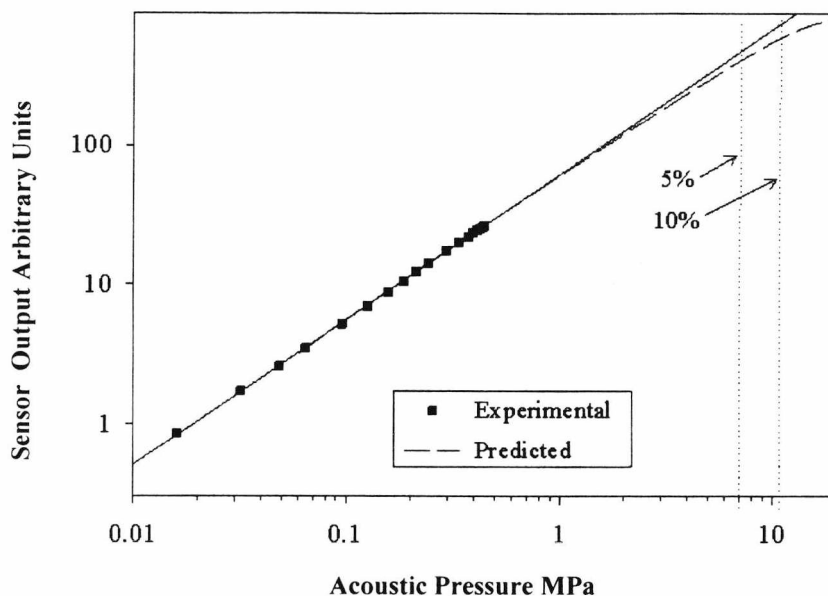
Figure 5.3 Linearity of an intensity-based optical fibre hydrophone employing a 50 μm thick PET sensing film.

Assuming the elastic limits of the polymer film are not exceeded, the upper limit of linear acoustic detection is determined by the characteristics of the interferometer transfer function. At the quadrature point, phase shifts up to 0.5 radians can be resolved with a linearity of better than ~5%. The dotted vertical lines show the acoustic pressure at which the sensor non-linearity becomes 5% and 10%.

5.5.3 Frequency Response

Figure 5.4 shows the experimentally measured frequency response of three different configurations. The first configuration is where the PET sensing film is glued directly to the multimode optical fibre (glass-backed PET). The second configuration is where the PET film is backed by water. The third case is where the optical fibre is composed of polymethyl methacrylate (PMMA). In each case 50 μm thick PET sensing films were used.
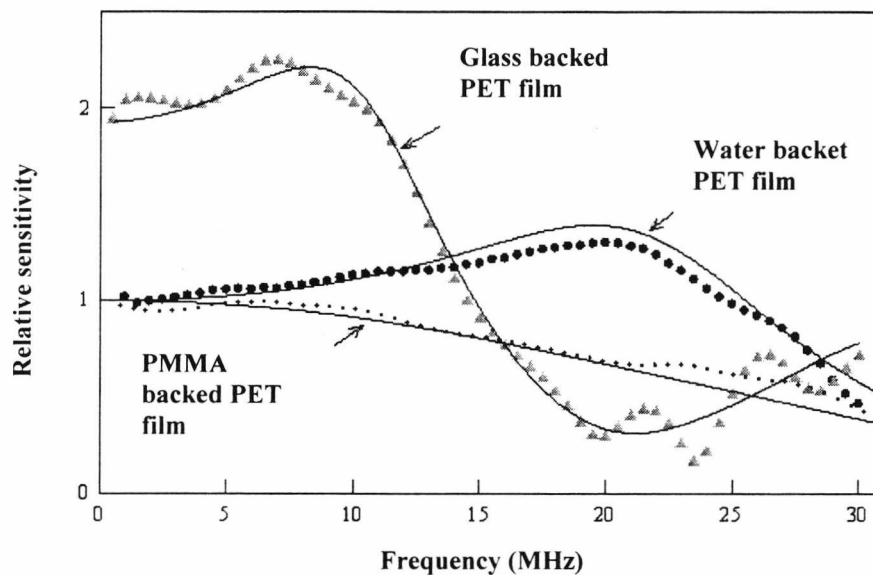
Figure 5.4 Experimentally measured frequency responses of three different backing configurations using 50μm thickness PET sensing film.

The continuous lines on figure 5.4 show the theoretically predicted frequency response. The acoustic frequency range shown in figure 5.4 is significantly greater than the frequency range provided by the experimental equipment used in the low-coherence investigations later on.

The intensity-based interrogation method used in this previous investigation is unsuitable for readily constructing sensors where the response is independent of variations in the polymer sheet thickness and the source wavelength. The sensor response will also be very dependent on the source intensity. A much more satisfactory interrogation system from the point of view of reproducibility would be the low-coherence heterodyne or psuedo-heterodyne system described in previous chapters. Here the acoustic signal would be encoded as a phase modulation of an optical carrier instead of the intensity modulation seen in the system of [4,5,6]. A heterodyne method of interrogation was chosen as a means of assessing the sensor response. The primary aims of this particular investigation were :-

•   Assessment of the feasibility of using a heterodyne interrogation method coupled with low-coherence techniques to see if a workable ultrasonic detector could be constructed using the same polymer film as in the investigations described previously. This would avoid the need for the polymer sensing films to be of the correct thickness to ensure quadrature operation.

•   Measurement of the sensor detection sensitivity and linearity and comparison of these values with :-

(a) Previous investigations of a low-finesse polymer cavity [4,5].

(b) The detection sensitivity of a calibrated polyvinyledine difluoride (PVDF) hydrophone.

(c) The FBG system discussed in a previous chapter of this thesis.

5.6   Experimental Arrangement

The heterodyne low-coherence interferometric system [7,8] used to interrogate the sensor is shown below in figure 5.5.
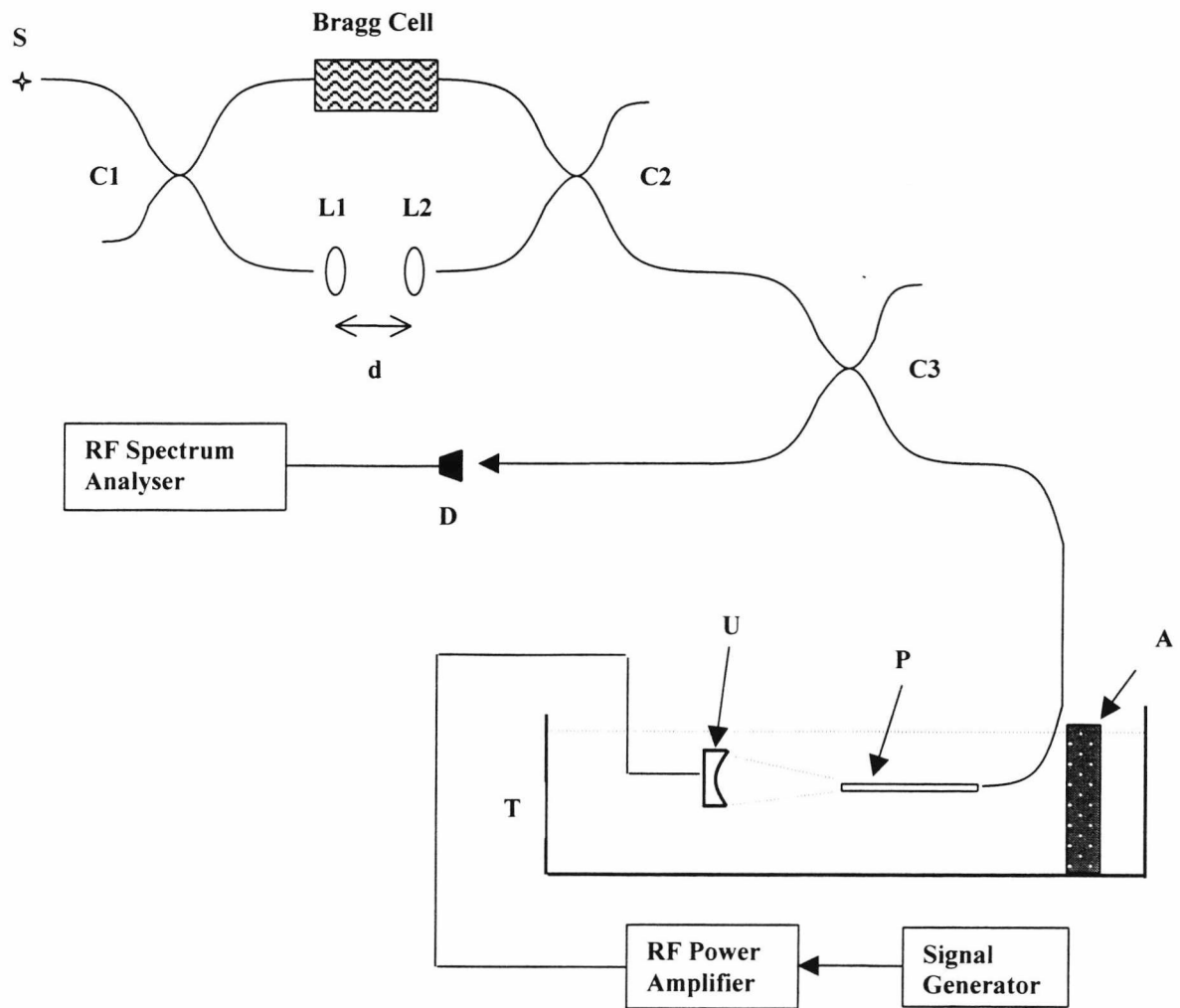
Figure 5.5 Heterodyne low-coherence interrogation of the polymer film sensor.

In the experimental arrangement of figure 5.5, S is a superluminescent diode source with a full width half maximum of ~30 nm with an output power of a maximum of 10 mW into single-mode fibre at a peak wavelength of 1310 nm. (This diode is model SLD-561-HP2). C1, C2 ,C3 are all commercially available fibre taper couplers optimised to have the correct 50:50 splitting ratio at the system

peak operating wavelength of 1310 nm. The Bragg cell was a commercially available acousto-optic fibre pigtailed frequency shifter unit (M040-8J-F2S from manufacturers Gooch and Housego) which is able to provide a high diffraction efficiency at 1310 nm, giving an insertion loss of < 2.4 dB. The Bragg cell operates at 40 MHz and for this particular model gives a frequency downshift, although the direction of the frequency shift provided by the Bragg cell will not affect the experimental results in any way. L1, L2 are collimating microscope objectives, L2 being mounted on a linear translation stage to allow the distance d between the objectives to be changed. This is to compensate for the unknown optical path length of the Bragg cell and also to allow the interferometer to be coherence tuned to the optical sensor. This is achieved by having the Mach-Zehnder interferometer optical path difference (OPD) equal to the sensor OPD. The polymer film sensor (P) is mounted on an x-y-z translation stage (not shown for sake of clarity) which allowed the sensor to be scanned across the ultrasonic field spatial distribution. This is for the focussed transducer only, as the planar transducer ultrasonic field has negligible spatial dependence. The backreflected light from the polymer film sensor in the water tank (T) is incident on an InGaAs p-I-n diode photodetector (D) coupled to a transimpedance amplifier (not shown on figure 5.5) with a bandwidth of 125 MHz. The output signal from this amplifier is fed into a radio-frequency spectrum analyser for analysis and measurement. The ultrasonic transducer (U) is powered by a high frequency sinewave signal generator coupled to a RF power amplifier, with a maximum RF output power of ~100 W. Two ultrasonic transducers were used in this investigation, one being the concave focussed 1.911 MHz medical transducer (from Hammersmith hospital) used previously in the fibre Bragg grating investigations, the other being a planar transducer at 612 kHz for sonar applications. Also included in the water tank behind the sensor was an acoustic absorbing material (A) to absorb any power from the ultrasonic transducer to prevent the formation of standing waves in the water tank, which could potentially interfere with any experimental results.

5.7   Construction of the sensor.

No investigations of a cavity based purely around the Fresnel reflection coefficients was performed as this would have resulted in a lower acoustic sensitivity than could be achieved with some form of enhancement of the reflectivity of the polymer surface. Also, the construction of a minature sensor was of some interest from the point of view of compactness and also the possibility of using such a sensor in-vivo to detect the pulsed ultrasonic fields from a lithotripsy machine. With these criteria in mind, the sensor design chosen was as shown in figure 5.2.
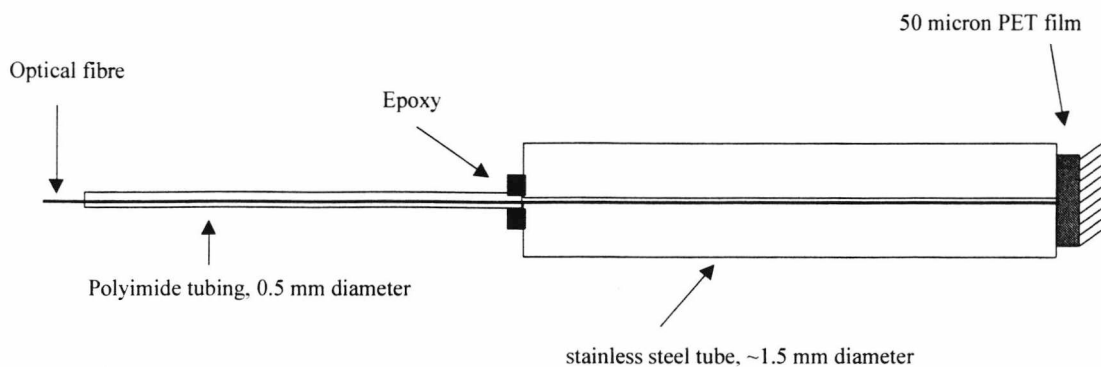
Figure 5.6 – Outline construction of polymer film sensor.

Referring to figure 5.6, the sensor consists of a stainless steel tube ~1.5 mm in diameter with a 250 μm hole through which a cleaved optical fibre is passed. The fibre is butted against the surface of a disc of PET ~1mm in diameter. The outer surface of the PET disc is aluminised to ~100% reflectivity, whilst the inner surface in contact with the steel tube was left uncoated. This design was chosen purely for ease of construction, as it was found that aluminising the polymer surface to a specified reflectivity value between 0 and 100% was extremely difficult due to the aged nature of the vacuum deposition apparatus. This apparatus consisted of a vacuum chamber with a heated tungsten filament on which small pieces of pure aluminium wire could be suspended. As the filament was not controlled by a constant current source accurate control of the deposition rate was not possible and it was found that as the aluminium melted and was drawn into the windings of the filament the resistance dropped due to the addition of

the aluminium, resulting in a drop in temperature and a subsequent decrease in the evaporation rate. Hence it was decided that only one surface of the PET would be aluminised. However, this does not detract from the validity of the experimental results, as aluminising the second face to a specified reflectivity would simply result in an improvement in the acoustic sensitivity. This approach is justified later in this chapter, where it is shown that useful experimental results can still be obtained using the sensor design given here. The PET film was bonded to the polished surface of the tube using a small amount of epoxy. Similarly, the fibre at the other end of the tube was also anchored in place with epoxy and additional strengthening was provided by a short (~6 cm) of polyimide tubing. Initial alignment of the sensor was performed by clamping the steel tube/PET film arrangement. The cleaved optical fibre was mounted in a linear translation stage and carefully butted up to the PET surface. The backreflected optical power was monitored using an optical powermeter. The cavity spectrum was observed on an optical spectrum analyser to ensure that interference fringes could be seen. Having determined that the sensor was giving rise to interference fringes the next step was to examine the sensor response to an ultrasonic field. Of particular interest were the sensor linearity, ability to spatially resolve the ultrasonic field profile from a focussed transducer and the noise limited pressure resolution. The sensor linearity is given in figure 5.7 as a function of the acoustic field pressure.
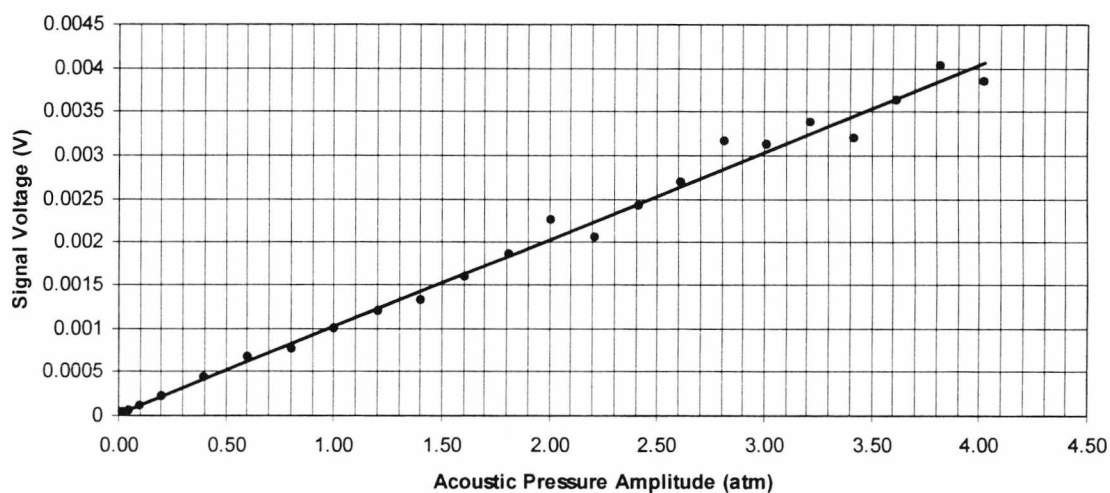
Figure 5.7 – Sensor response as a function of acoustic field pressure.

From figure 5.7, the sensor response is reasonably linear up to ~2.00 atmospheres (~ 2×10^5 Pa), after which significant scatter in the response is apparent. The mechanical construction of the sensor may contribute to the observed scatter. The diameter of the sensor is approximately twice the acoustic wavelength. Hence diffraction of the acoustic field will occur with the subsequent generation of nodes and antinodes of the acoustic field over the area of the PET film. This will give rise to a modulation of the film thickness which may vary significantly over the area of the film as the acoustic pressure is increased. Even though the film is firmly anchored to the steel tubing, the acoustic pressures generated here may be sufficient to cause the film to be subject to lifting forces which cause the film-fibre gap (nominally zero) to vary, giving rise to an unpredictable acoustic response. In short, this sensor may be useful for small acoustic field pressures, but will show significant scatter in the measurements as the field pressure is increased. However, it was still thought useful to examine the ability of this design to spatially resolve the acoustic field profile of a focussed transducer. The results of this investigation are given in figure 5.8.

F-P sensor 1.911 MHz spatial resolution
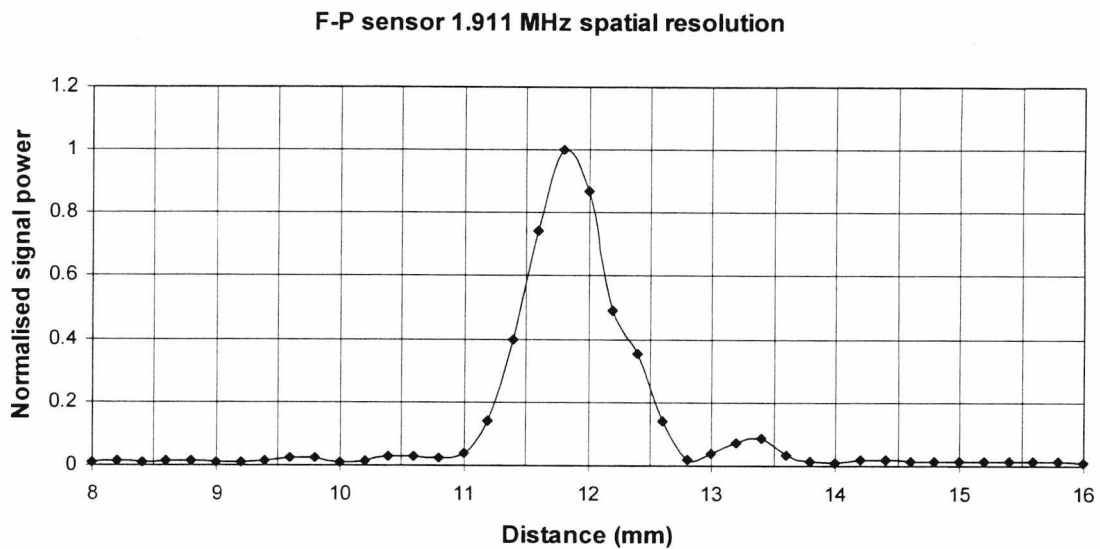
Figure 5.8 – F-P sensor 1.911 MHz spatial field profile resolution

Even though the sensor dimensions are greater than the acoustic wavelength, figure 5.8 demonstrates that useful resolution of the field profile can still be obtained, the width of the central maximum corresponding closely with the calculated width of the transducer profile. The noise limited pressure resolution of this sensor was found to be 7.15×10^{-4} atm/√Hz (~72 Pa /√Hz) at 1.911 MHz. The NLPR of the calibrated PVDF hydrophone was measured and found to be be 1.25×10^{-5} atm/√Hz (~1.3 Pa /√Hz) at 1.911 MHz. Hence the acoustic pressure sensitivity of this particular design of sensor is ~60 times less than that of the PVDF hydrophone at 1.911 MHz. As another ultrasonic transducer had recently become available, it was of some interest to compare the results obtained at 1.911 MHz with those obtainable from this second transducer. However, the second transducer was a planar transducer used primarily for sonar applications. Hence the acoustic field generated was unfocussed. Therefore only measurements of the sensor linearity and noise limited pressure resolution could be made. The planar sensor resonant frequency was 612 kHz, providing a useful lower frequency against which to compare differences in linearity and noise limited pressure resolution. The acoustic field pressures obtainable with this second transducer were significantly smaller than those obtainable with the focussed transducer, for obvious reasons. The results of the investigation of the sensor linearity at 612 kHz are given in figure 5.9.

F-P cavity sensor 612 kHz response
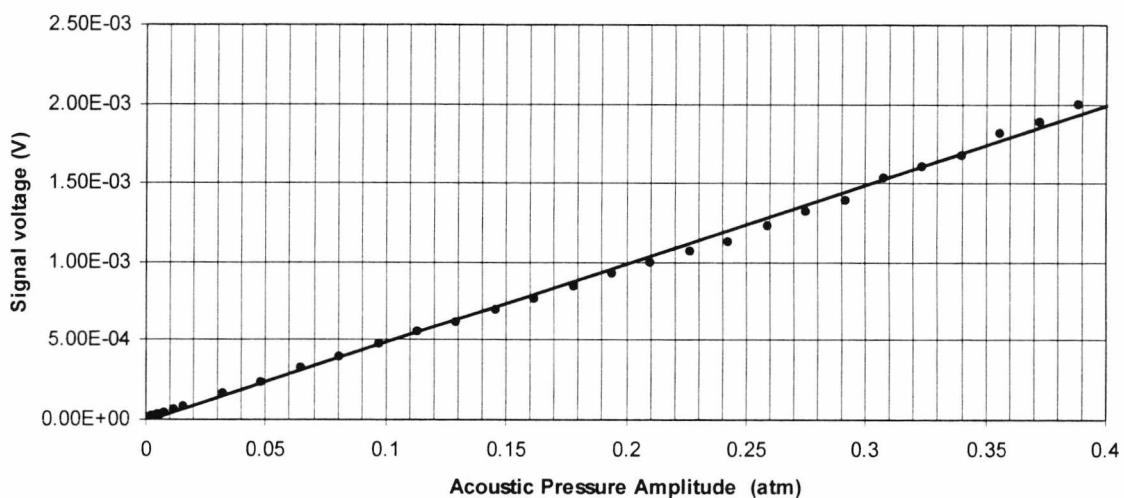
Figure 5.9 F-P sensor linearity at 612 kHz

Some small degree of scatter in the experimental results can be seen from figure 5.9. As the acoustic pressures generated by the planar transducer are significantly smaller than those from the focussed transducer, the sensor response is linear to within ~5% over the range of pressures examined here. The noise limited pressure resolution at this frequency was measured and was found to be 1.09×10^{-4} atm/$\sqrt{Hz}$ (~11 Pa/$\sqrt{Hz}$), significantly higher than that at 1.911 MHz. This is an unexpected result as the acoustic sensitivity should be frequency independent at these relatively low frequencies. The NLPR at 612 kHz is only an order of magnitude less than the NLPR for the PVDF hydrophone, which was measured as 1.25×10^{-5} atm/$\sqrt{Hz}$. (~1.3 Pa /$\sqrt{Hz}$). Considering the relative simplicity of this sensor design this is an encouraging result from the point of view of building cheap sensors with a high acoustic sensitivity. In its current form the sensor could not be used *in-vivo*, as the sensor diameter is too large to fit into a medical catheter. Also, consideration would have to be given to the biological compatibility of the materials used in the sensor design. However, the primary aim of this investigation was to assess the applicability of this particular method of constructing and interrogating an ultrasonic detector based around low-coherence techniques rather than the final construction of a useable medical device. With some further mechanical development this design could almost certainly be minaturised and made biologically compatible.

5.8   Summary and Conclusions.

A relatively simple design of interferometric cavity sensor has been implemented and the sensor acoustic response assessed at two different ultrasonic frequencies. The experimental results and comparison with the results of [4,5,6] are given in table 5.1 overleaf, which gives the noise limited pressure resolutions in Pa/$\sqrt{Hz}$ as well as a comparison with the sensitivity of the calibrated hydrophone used in these experiments, and the fibre Bragg grating sensor investigated previously.

Sensor type	Noise limited pressure resolution. (Pa/√Hz)	Sensitivity in dB relative to calibrated PVDF hydrophone.	Upper range of detection linearity (Mpa)
0.5mm diameter PVDF bilaminar membrane. Model Y-34-3698.	~1.3 (f = 1.911 MHz)	0	~1 MPa
Low-finesse cavity of refs [4,5,6].	~ 2 (f = 0 to 25 MHz).	3.7	~7 MPa (5%) ~10 MPa (10%)
Heterodyne interrogated low-coherence system.	~72 (f = 1.911 MHz) ~11 (f = 0.612 MHz).	35.0 18.5	~0.2 MPa (5%)
FBG sensor.	~4500 (f = 1.911 MHz)	71.0	~0.25 MPa

Table 5.1 Summary of experimental results for low-finesse cavity.

Table 5.1 demonstrates that despite the relative simplicity of the sensor and of the experimental arrangement the results of the investigations detailed in references [4,5,6] are in some respects superior to those obtained using the low-coherence heterodyne interrogation technique investigated here in terms of higher acoustic detection sensitivity and linearity range. However, the use of heterodyne signal processing techniques coupled with a low-coherence interrogation method avoids the need to maintain the phase bias of the low-finesse cavity sensor at quadrature in order to achieve a high acoustic detection sensitivity. Some deviation from the expected frequency dependence of the acoustic sensitivity was observed, the sensor being more sensitive at the lower ultrasonic frequency. This is an unexpected result and further investigations would benefit from the availability of some form of tunable ultrasonic source so that the sensor frequency response could be more accurately assessed over a more comprehensive frequency range. At the lower frequency of 612 kHz the acoustic sensitivity is only an order of magnitude less than the significantly more expensive calibrated PVDF hydrophone. This suggests that this simple design may provide a cheap alternative to more expensive commercially available hydrophones. Also, the all-optical nature of the sensor readily provides a high degree of immunity from spurious electrical pickup.

References:-

1. J.J.ALCOZ, C.E.LEE, AND H F.TAYLOR, : 'Embedded Fiber_Optic Fabry-Perot Ultrasound Sensor.', IEEE Transactions on Ultrasonics, Ferroelectrics and Frequency Control, Vol. 37, No. 4 July 1990.

2. J.SIRKIS, T.A.BERKOFF, R.T.JONES, H.SINGH, A.D.KERSEY, E.J. FRIEBELE AND M.A. NEWMAN. : 'In-Line Fiber Etalon (ILFE) Fiber-Optic Strain Sensors.', Journal Of Lightwave Technology, Vol. 13, No. 7, July 1995 pp 1256-1263.

3. J.SIRKIS, D.D.BRENNAN, M.A.PUTMAN, T.A.BERKOFF, A.D.KERSEY, E.J. FRIEBELE. : 'In-Line Fiber Etalon for Strain measurement', Optics Letters, Vol. 28, No.22, November 15th 1993.

4. P.C. BEARD AND T.N.MILLS. : 'Extrinsic optical-fibre ultrasound sensor using a thin polymer film as a low-finesse Fabry-Perot interferometer.', Applied Optics, Vol. 35, No.4, 1st February 1996 pp 663-675.

5. P.C. BEARD AND T.N.MILLS. : 'Minature optical fibre ultrasonic hydrophone using a Fabry-Perot polymer film interferometer.',Electronics Letters, 18, No. 9, 24th April 1997, pp 801–803.

6. BEARD, P.C., HURRELL, A., ELZEN, E, van den., MILLS, T.N.: 'Comparison of a minature ultrasonic optical fibre hydrophone with PVDF hydrophone technology', Proc. IEEE Ultrasonics Symposium, 1998.

7. SANTOS, J,L, LEITE, A.P,, JACKSON, D.A.: 'Optical fibre sensing with a low finesse Fabry-Perot cavity.', Applied Optics, 31, No 34, 1st Dec. 1992, pp 7361-7366.

8. B.T.MEGGITT, W.J.O.BOYLE, K.T.V.GRATTAN, A.E.BARUCH AND A.W.PALMER. : 'Heterodyne processing scheme for low coherence interferometric sensor systems', IEE Proceedings-J, Vol. 138, No.6, December 1991 pp 393-395.

Chapter 6

Acoustic Detection using Er^{3+} Fibre Bragg Grating Lasers.

6.1   Introduction

Optical hydrophones based around the use of optical fibre as the sensing element were first demonstrated in the late 1970's [1]. Initial attempts involved a number of measurement techniques, such as amplitude and polarisation sensing [2]. However, the most successful optical hydrophone systems in terms of providing the highest acoustic detection sensitivity have been based around the use of interferometric techniques [3]. An unbalanced interferometer system with a long coherence length laser source generally provides the highest acoustic detection sensitivity. A typical fibre-based interferometric system is outlined below in figure 6.1.
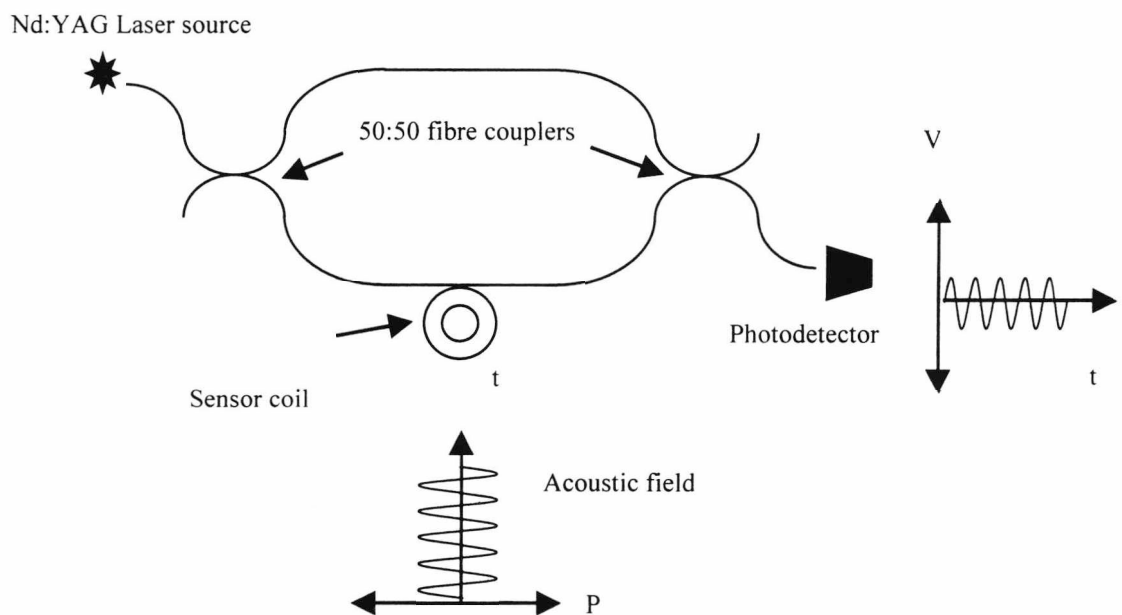
Figure 6.1 – Optical hydrophone based on a Mach-Zehnder interferometer

The impetus for further development of optical hydrophone systems has been and continues to be military. The use of highly sensitive sonar arrays obviously provides an advantage in detecting both submarines and ships. The acoustic signal is transduced into a change in the optical path length of the sensor coil. This optical path length change manifests itself as a periodic intensity variation at the interferometer output, readily detectable by a photodetector. To further increase the detection sensitivity the fibre is often coiled around a mandrel of acoustically compliant material. While providing for a high acoustic detection sensitivity the arrangement shown in figure 6.1 suffers from a number of disadvantages, the main one being the difficulty of achieving a multiplexed array. A secondary consideration is the limited upper frequency response of such a mandrel based hydrophone, a typical upper response being of the order of a few kHz. Also the coils are bulky and do not easily lend themselves to the construction of a small hydrophone array. An ideal optical hydrophone would have the following advantages over its electrical (and optical) counterparts.

- Freedom from spurious electrical pickup.
- Easy multiplexing/demultiplexing into an array of as many sensors as required.
- Small dimensions to minimise the array size and weight.

The figure of merit used in characterizing hydrophone systems is the acoustic detection sensitivity relative to a parameter known as <u>Deep Sea State Zero (DSSO)</u>. This is the noise floor experienced in the quietest parts of the deep ocean, and in terms of acoustic pressure is –80 dB relative to 1 Pascal /$\sqrt{\text{Hz}}$ @ 1kHz, or 10^{-4} Nm^{-2} @ 1 kHz. The type of system outlined in figure 6.1 can easily achieve an acoustic detection sensitivity equal to or even in excess of DSSO. With the above criteria in mind, it is useful to examine the merits of various in-fibre sensor components/configurations to try and determine which one would be the most suitable in terms of achieving the required detection sensitivity of DSSO. The choice of optical components which could potentially form a multiplexed system is given overleaf.

1.   Standard FBGs (linewidth $\approx$ 0.2 nm);

2.   Strong FBGs;

3.   Narrow linewidth long FBGs;

4.   Fabry-Perot cavities;

5.   Moiré gratings;

6. π-shifted grating;

7.   Er^{3+} Fibre lasers.

The Bragg wavelength shift associated with a pressure of DSSO is of the order of 10^{-8} *nm* (calculated later in this chapter). Clearly a very significant increase in sensitivity of several orders of magnitude is required and this allows standard FBGs to be completely ruled out as the sensing element. Options 2 to 6 in the list above all result in spectral features where the reflectance changes very rapidly with wavelength. Option 3 was ruled out due to practical difficulties in fabrication coupled with the difficulty of maintaining a long structure (~1 m) in an unstrained state and the requirement that the sensing length should be shorter than 1 m. The fundamental difficulty associated with components 2-6 lies in accurately tracking the peak of the narrow spectral features so as to recover the acoustic signal, as acoustic signals would manifest themselves as a wavelength shift in the spectral feature of interest. In order to achieve high acoustic detection sensitivity the spectral feature needs to be as narrow as possible (subnanometer width) so as to accentuate any acoustically-induced wavelength shifts. For this reason the best choice of device for the construction of a high sensitivity acoustic sensor would appear to be an in-fibre Er^{3+} laser. The aims of this chapter are:-

- The construction of a multiplexed array of such sensors.
- The experimental measurement, where possible, of the limiting noise sources in the system.
- Assessment of the feasibility of different demultiplexing schemes for an array of sensors.
- Comparison of experimental measurements of the laser sensor acoustic detection sensitivity with other sensor systems.

However, before discussing the use of fibre lasers as a potential acoustic sensor, it is useful to examine some of the current approaches taken towards constructing an interferometric hydrophone array and to compare and contrast the relative merits of the different interrogation schemes required and also their respective sensitivities. The use of a fibre laser as a dynamic strain sensor will also be discussed [15] and the sensitivity obtained from such a system will be compared with that obtainable from the types of interferometric systems currently being considered elsewhere [3].

6.2   Erbium fibre laser as a dynamic strain sensor.
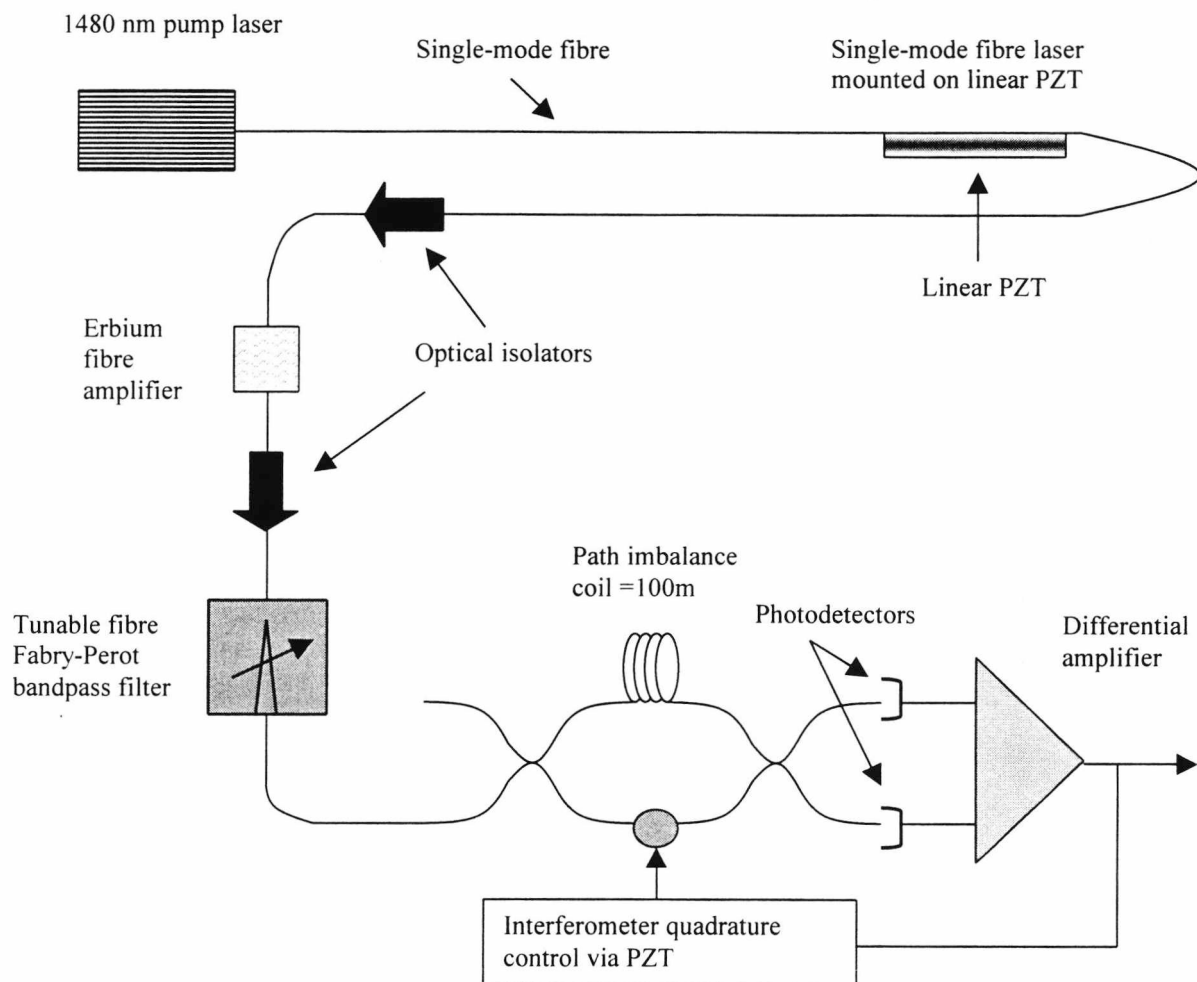
Figure 6.2 Erbium fibre laser as dynamic strain sensor.

In figure 6.2, showing the experimental arrangement of the study of [15], optical pump power for the fibre laser was provided by a 1480 nm pump laser diode operating at around 70 mW. The fibre laser was mounted on a linear piezoelectric translation stage which allowed a dynamic longitudinal strain at a known amplitude to be applied to the laser. The laser cavity length was 2.5 cm and the laser was single-mode at λ=1554 nm, determined by the FBG peak reflectivity wavelength. An additional length of erbium fibre following the laser served to provide extra amplification of the laser signal. The tunable fibre Fabry-Perot filter filtered out the 1480 pump power and allowed only the laser wavelength into the Mach-Zehnder interferometer. The filter also had the additional effect of filtering out the amplified spontaneous emission noise of the erbium fibre amplifier. The optical isolators shown in figure 6.2 served to prevent any potential instabilities caused by backreflected fibre laser light re-entering the fibre laser [31]. The interferometer was actively maintained at quadrature by a feedback loop from the differential amplifier output to a piezoelectric cylinder in one of the interferometer arms. Hence the signal from the laser could be recovered by measuring the feedback voltage required to maintain the interferometer at a quadrature position. From [15], the noise-limited strain resolution of this system was found to be 5.6×10^{-14} /$\sqrt{\text{Hz}}$, or 56 femtostrain /$\sqrt{\text{Hz}}$ at a dynamic strain frequency of 7kHz. In terms of acoustic pressure this is equivalent to a noise-limited pressure resolution of approximately 6×10^{-3} Pa/$\sqrt{\text{Hz}}$. This was estimated as follows for the laser of length L_{FL} = 2.5 cm subject to a pressure P giving rise to a strain ε :-

$$\varepsilon = \Delta L_{FL} / L_{FL} = (P/E)(1 - 2\mu) = 56 \times 10^{-15} \rightarrow P = 6 \times 10^{-3}\ Pa$$

Substituting values of Young's modulus E = 70 GPa, μ = 0.27 into the formula above gives a minimum detectable pressure P in a 1 Hz bandwidth of the order of 6×10^{-3} Pa. Although this result from [15] is for a dynamic strain frequency of 7 kHz, it is still of some interest to compare this minimum detectable pressure with the DSSO value of 10^{-4} Pa/$\sqrt{\text{Hz}}$. The system defined in [15] appears to be capable of approaching a detection sensitivity of DSSO, and is a factor of ~35 dB away from this value.

6.3 Interrogation and multiplexing schemes for interferometric hydrophone arrays.

6.3.1 Gated phase modulated heterodyne technique

Current approaches towards constructing an optical fibre hydrophone system are based around the simple Mach-Zehnder interferometer system shown previously in figure 6.1. Such a single-sensor arrangement can provide an acoustic detection sensitivity of 30 dB below the accepted Deep Sea State Zero (DSSO) figure of merit of −80 dB relative to 1 Pascal /√Hz @ 1kHz, or 10^{-4} Nm^{-2} @ 1 kHz [3]. However, a single sensor does not provide the distributed detection capability required for current applications, geophysical surveying for oil prospecting, for example, or submarine and ship detection which is of obvious military interest. Hence some form of multiplexing is required which allows several sensors to be used in such a way as to provide a distributed acoustic sensor array. The first demonstration of a multiplexed optical hydrophone array achieving an acoustic detection sensitivity of DSSO was given in [4]. The optical layout of this system is outlined below in figure 6.3.
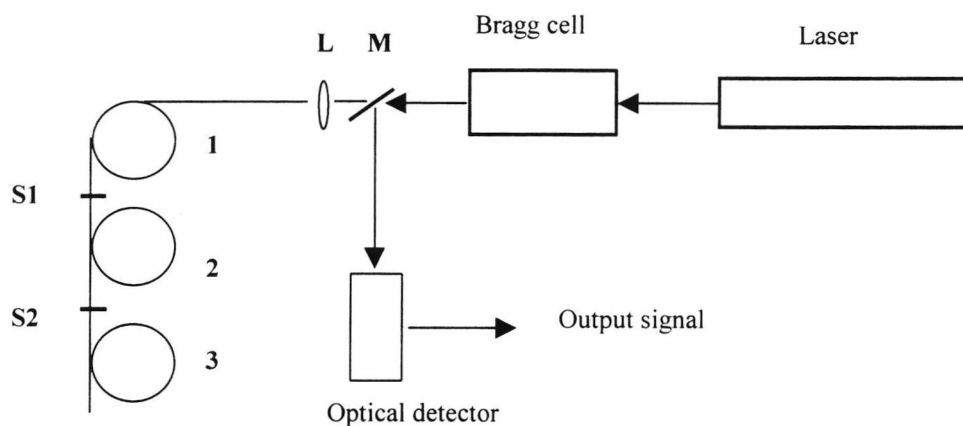
Figure 6.3 First demonstration of multiplexed optical hydrophone array.

Referring to figure 6.3, 1, 2, 3 indicate the separate sensors in the array. S1 and S2 are reflective splices between the sensors. L is a convex lens coupling the laser beam into the optical fibre, M is a partially silvered mirror which allows the backreflected signals from the sensors to be coupled into the optical detector. The sensors consist of fibre loops which, in combination with the reflective splices between the loops, form a series

of low-finesse Fabry-Perot cavities. The Bragg cell in this arrangement is being operated both as an optical modulator and as an optical gate which allows the generation of a series of optical pulses into the array. The interrogation technique is illustrated below in figure 6.4, which shows the pulse sequence from the Bragg cell on the same time axis as the backreflected pulses from the sensor array. Also shown on the same axis is the optical detector output signal.
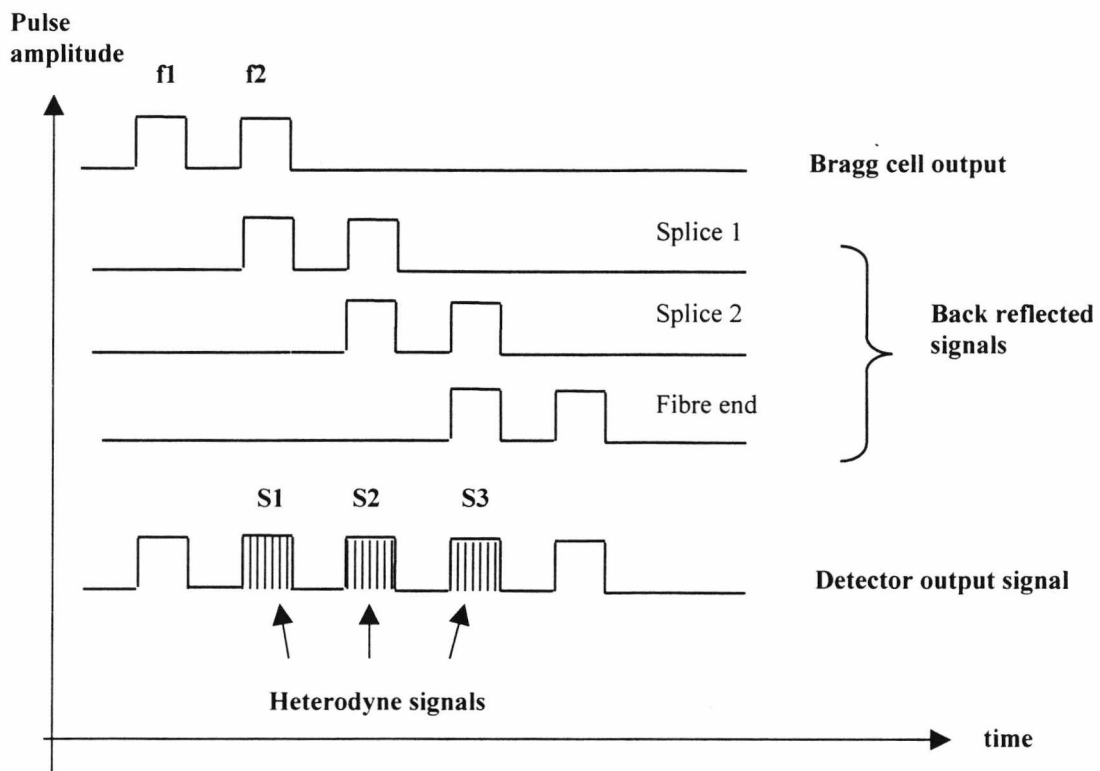
Figure 6.4 Gated optical input and corresponding detector output

Referring to figure 6.4, the Bragg cell is gated to produce two optical pulses separated in time by the transit time of the light through each sensor element. Also the separate pulses are generated at two different Bragg cell modulation frequencies $f1$ and $f2$. Considering sensor 1, light modulated at frequency $f1$ and reflected from the rear face of sensor 1 (reflective splice S1) will coherently mix with the light reflected at frequency $f2$ from the front face of the same sensor (the bare fibre end immediately after the convex lens L), to produce a heterodyne signal at the detector output equal to the difference frequency $(f1 - f2)$. If the sensor coil is in turn acoustically excited then

the phase of the optical heterodyne signal will be influenced by the corresponding optical path length changes in the sensor, giving rise to modulation in the ($f1$ $-f2$) heterodyne signal. The same argument applies to sensors 2, 3 further along the array. This approach to optical sensor multiplexing is known as gated phase modulation heterodyne multiplexing, and is effectively a form of time division multiplexing. While demonstrating the feasibility of multiplexing an array of optical acoustic sensors, the main disadvantage of this approach is the decreasing signal to noise ratio as one progresses further down the sensor array, due to the reflective splices which form an integral part of the sensor Fabry-Perot cavity. These splices will cause optical losses which will in turn decrease the amplitude of the returned heterodyne signal. As mentioned previously, for a small number (~3-4) of sensors, this optical arrangement can produce optical detection sensitivities approaching DSSO. An alternative approach to multiplexing involves a phase generated carrier technique and it is this approach which will be discussed next along with typical detection sensitivities for such a system.

6.3.2 Phase generated carrier techniques

An illustration of this approach is given in figure 6.5 for a four sensor array .
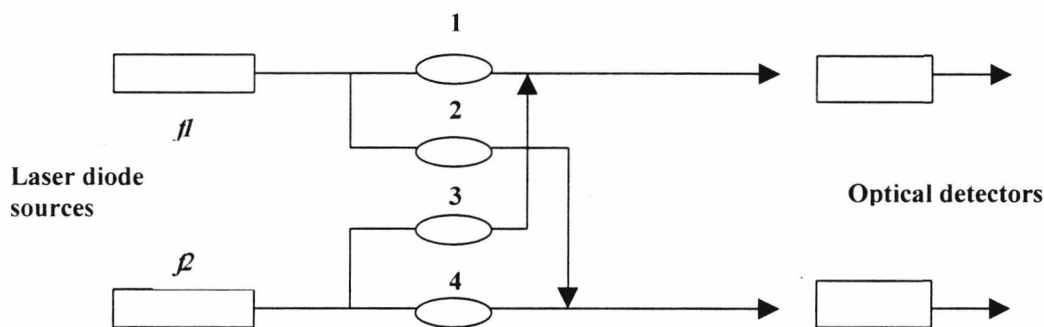
Figure 6.5 – Hydrophone multiplexing using phase generated carrier technique

Referring to figure 6.5, the array of acoustic sensors (1-4) consists of four path-imbalanced Mach-Zehnder interferometers illuminated by two laser diode sources. The acoustic detection element in each of the interferometers consists of a fibre coil wrapped around an acoustically compliant mandrel, as discussed in section 6.1 of this chapter. Each laser diode source is modulated at a different fixed carrier frequency, one

source at *f1*, the other at *f2*. The output at each detector consists of the signals from two hydrophones, each hydrophone signal being encoded as a phase modulation of the carrier signal from the modulated laser diode source. Demultiplexing and demodulation of the hydrophone signal is provided by narrowband filtering the detector output signal to recover the carriers at frequencies *f1* and *f2*. For example, consider hydrophones 1 and 3 in figure 6.4. The output signal from these two hydrophones is detected by the topmost optical detector. Hydrophone 1 will be interrogated at a carrier frequency *f1*, similarly, the acoustic signal from hydrophone 3 will be heterodyned with the carrier signal at frequency *f2*. A similar argument applies to hydrophones 2 and 4. Once the carrier frequencies have been recovered, the acoustic signal heterodyned with the carrier can be retrieved using standard demodulation techniques. An increase in the number of multiplexed hydrophones can be provided by having several sources all generating carriers of different frequencies. This is effectively a form of frequency division multiplexing (FDM), where the response of each sensor, an acoustic signal in this case, is encoded on a separate carrier frequency. Systems based on this approach have achieved noise floors as low as 10 dB below DSSO [3,5]. While achieving a high detection sensitivity, this approach still relies on the use of unbalanced interferometers to provide the acoustic sensors, with the corresponding need for some form of acoustically complaint mandrel and hence an increase in the sensor size.

6.3.3 Time division multiplexing (TDM)

This is illustrated in figure 6.6 for a linear array of six Mach-Zehnder interferometric hydrophone sensors. Referring to figure 6.6, each of the sensors is separated by a reflective element, which can be a reflective splice.
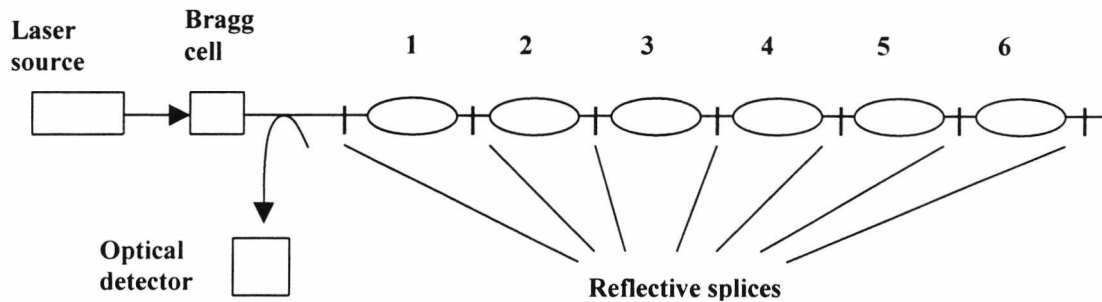
Figure 6.6 Time division multiplexed hydrophone array

In figure 6.6, the Bragg cell is used to generate gated optical pulses at two separate Bragg cell modulation frequencies. The time separation of the pulses is set equal to the transit time between each of the reflective splices, each interferometer sensor (1-6) having the same optical path length and each reflective splice being spaced equidistantly. In the arrangement in figure 6.6, the backreflected pulses from the separate interferometers are detected by an optical detector via a fibre optic coupler, where gating circuitry in the detector separates out the signals from each sensor according to their relative time distribution i.e. pulses arriving later are those from interferometers situated further along the array. The acoustic signal is encoded as a phase modulation on the carrier signal generated by the mutual interference of the two frequencies generated by the Bragg cell, in the same way as described previously in section 6.3.1 for the gated phase modulation heterodyne technique. The multiplexing limits in a TDM array are determined by the optical power budget. As the number of sensors increases so the optical signal amplitude returned from sensors further along the array decreases, giving a reduced signal to noise ratio. However, TDM optical hydrophone array systems with up to six hydrophones as shown in figure 6.6 have achieved noise limited pressure resolutions of up to 10 dB below the DSSO figure of merit over a frequency range of 400 Hz to 2 kHz [3].

6.3.4   Problems with interferometric hydrophone arrays.

The most important problem common to all interferometer based sensors is that of polarisation fading [6,8]. This is the unpredictable loss of interference efficiency between the separate arms of the interferometer due to random changes in the beam polarization state caused by changes in fibre birefringence. This can lead to the random degradation or even loss of signal for one or more of the hydrophones. Faraday rotator mirrors can be used to effectively remove all polarization sensitivity from an interferometric sensor system, as demonstrated for a Michelson interferometer [7]. Also of importance in interferometers with long path imbalances is the conversion of the optical source (laser) phase noise into intensity noise due to the large path imbalances required to achieve the desired high acoustic detection sensitivity. The use of large path imbalances also implies that the source coherence length must exceed the path difference between the interferometer arms if interference is to take place. Hence the optical source of choice for interferometric hydrophone arrays with long path imbalances is the Nd:YAG laser, which combines high optical output powers (>100 mW) with large coherence lengths.

6.3.5   Summary of acoustic detection sensitivities for hydrophone arrays.

Table 6.1 below provides a summary of the achievable acoustic detection sensitivities relative to DSSO for the systems discussed previously.

Sensor type	Multiplexing system	Acoustic detection sensitivity relative to DSSO (@ 1kHz)
Dynamically strained erbium fibre single laser. [ref 15]	Not applicable	+35dB
Single unbalanced Mach-Zehnder interferometer with acoustically compliant mandrel	Not applicable	-30 dB
Low finesse Fabry-Perot cavities	Gated phase modulated heterodyne	0 dB
Unbalanced Mach-Zehnder with acoustically compliant mandrel	Phase generated carrier	-10 dB
Unbalanced Mach-Zehnder with acoustically compliant mandrel	Time Division Multiplexing	-10 dB

Table 6.1 Acoustic detection sensitivities of multiplexed optical hydrophones and erbium fibre single laser sensor.

Also included in table 6.1 is the detection sensitivity of a single element hydrophone based on the simple scheme shown in figure 6.1 using an unbalanced Mach-Zehnder interferometer [3]. The detection sensitivity of the system from [15] is also included. In table 6.1, a relative detection sensitivity of 0 dB corresponds to a sensitivity of DSSO.

It can be seen that even relatively simple optical hydrophone arrays can readily achieve acoustic detection sensitivities of or even exceeding DSSO. However, a number of disadvantages exist even with the high acoustic sensitivities obtained with interferometric techniques. The first of these is the physical size of the sensor. This is of importance in arrays where large numbers of sensors are required. In order to enhance the sensitivity, a large length of fibre (100m or more) is coiled around an acoustically compliant cylindrical mandrel which physically deforms when subjected to acoustic waves, this physical deformation causing a corresponding change in the fibre optical properties. The minimum size of this mandrel is determined by the mininum bend radius of the fibre, which for standard telecommunications fibre at 1550 nm is of the order of 3-4cm.

Fibre bend radii exceeding this would lead to unacceptable optical losses and reduced sensitivity. As the sensors are passive, the returned signal amplitude in a multiplexed array is determined by the source optical power. For sensors further down the array (away from the source) the signal to noise ratio will be decreased relative to sensors closer to the source, hence the system sensitivity will be a function of the number of sensors. A more desirable sensor from the point of view of ease of multiplexing and small size would be an erbium fibre laser. The lasers could be constructed with unique wavelengths which would readily allow some form of wavelength division multiplexing technique.

6.4   Er^{3+} based fibre lasers.

The optical properties of a silica fibre core can be radically altered by doping the core with rare earth elements, specifically erbium in this application. With a suitable optical pump source the erbium doped fibre functions as an efficient optical amplifier in the region ~1500-1600 nm [9]. In order to ensure a high optical pump density and efficient usage of the pump signal the core diameter of an erbium doped fibre is often significantly less (~2 μm) than that of an ordinary single mode fibre (~5μm diameter). The optically amplifying properties of erbium doped fibres have obvious applications in telecommunications where there is often a need to compensate for the inevitable absorbtion/scattering losses in a long fibre by having some form of amplification at regular intervals [10], a primary example of this being undersea communications links where the total fibre length can be several thousands of kilometers. An energy level diagram for Er^{3+} ions in silica with associated emission and absorption processes is shown below in figure 6.7.
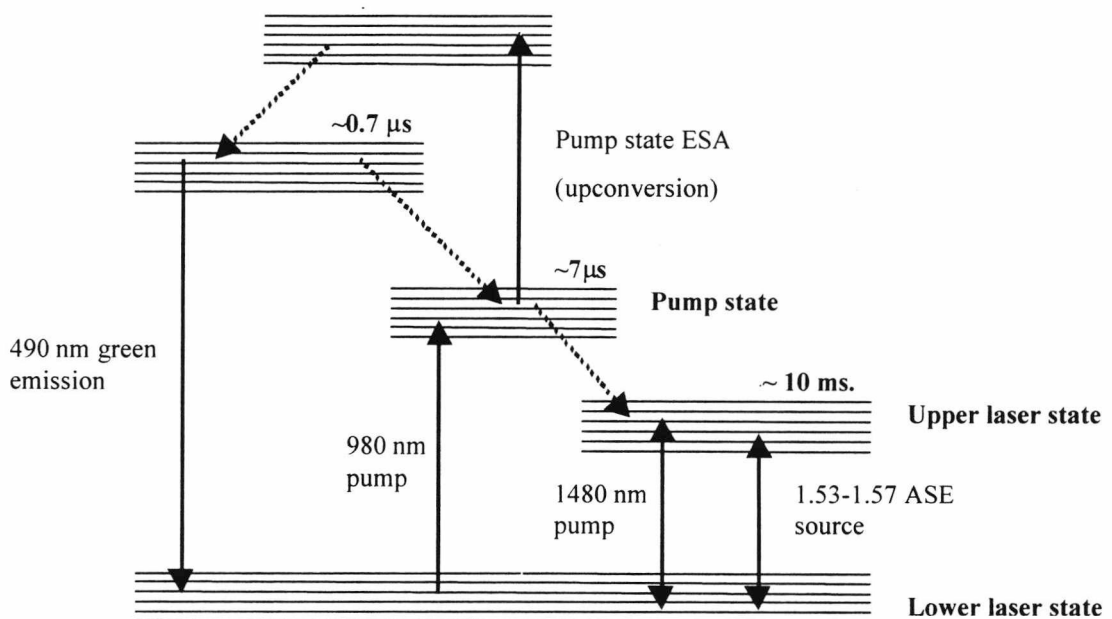
Figure 6.7 Energy level diagram for Er doped silica pumped at 980 or 1480 nm including possible ESA processes and state lifetimes.

In figure 6.7, solid arrows denote photon emission/absorption processes, dotted arrows denote nonradiative decay processes where the ion excitation energy is lost to the surrounding silica as phonons (heat). The energy levels are broadened by Stark splitting and are occupied according to Boltzmann statistics. Consequently the absorption and emission cross-sections are temperature dependent quantities. The doped fibre can either be pumped at 980 nm or 1480 nm, the wavelength of choice being determined by the application. The pumping efficiency is higher at 980 nm than at 1480nm. The three energy levels of most interest in terms of building a laser are the pump, upper and lower states as shown in figure 6.7. To form the laser cavity a pair of FBGs can be written into a length of doped fibre [12] as shown in figure 6.8. Also of interest are the excited state absorption (ESA) or upconversion processes from the pump state to higher energy levels [11]. These processes give rise to pump frequency doubling to 490nm which can be clearly seen as a green glow when the fibre is pumped at 980 nm. Secondary decay and absorption processes between the upper and lower laser states give rise to amplified spontaneous emission (ASE) which can be a significant noise source in erbium doped fibre amplifiers [10].

Few cm cavity in Er^{3+} doped fibre.

pump λL λL

Single-mode
Optical fibre

Fibre Bragg Gratings
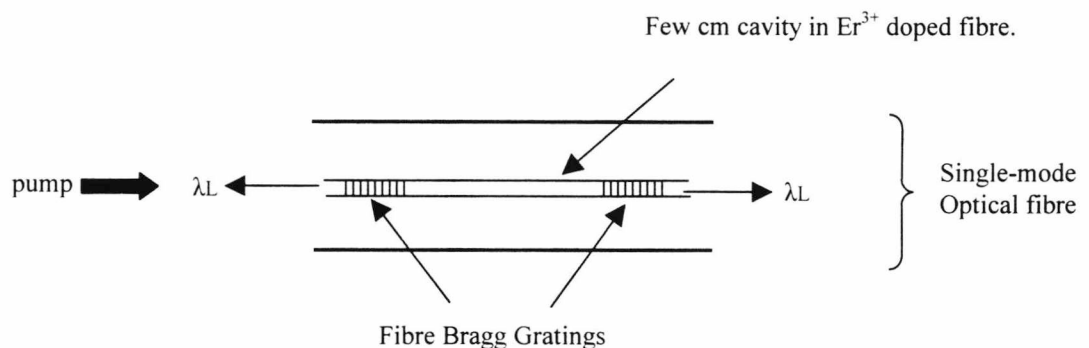
Figure 6.8 – Outline construction of a Distributed Bragg Reflector fibre grating based Er^{3+} laser

The DBR laser wavelength is determined by both the FBG reflectivity profile and by which mode or modes are above the threshold reflectivity for laser action. This is illustrated in figure 6.9, where $R(\lambda)$ is the FBG wavelength response. From figure 6.9, only the $n'th$ mode will fall above the threshold reflectivity and give rise to laser action. In the event of two or more modes being above threshold then the laser will be multimode. The mode spacing is determined by the cavity length and the core refractive

index. For a sufficiently short cavity the laser will be single mode [12,13], as the mode spacing will be large enough for only one mode to be above threshold, assuming that the FBG peak reflectivity is chosen to coincide with this mode wavelength.
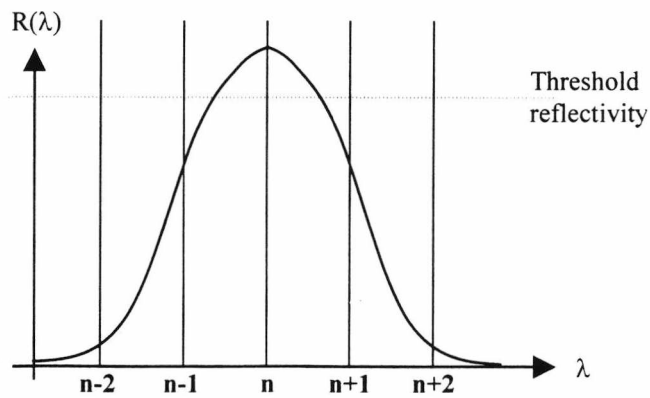
Figure 6.9 – Laser wavelength selection from mode spacing and FBG profile

Light within a laser cavity of length L in a fibre core of refractive index n will resonate when there are an integral number m of half wavelengths within the cavity. The optical path length of the cavity will differ from the physical path length and is given simply by nL. The value of m is therefore given by:

$$m = \frac{nL}{\lambda/2} = \frac{2nL}{\lambda} \tag{6.1}$$

Hence the cavity mode frequencies v_m are given by:

$$v_m = \frac{c}{\lambda_m} = \frac{mc}{2nL} \tag{6.2}$$

where c is the velocity of light in a vacuum. The mode spacing Δv is therefore

$$\Delta v = \frac{c}{2nL} \tag{6.3}$$

For a refractive index $n \sim 1.5$ and a typical cavity length L of 0.05 m the mode spacing is approximately 2GHz, which for a typical laser wavelength of 1550 nm corresponds to a spacing of approximately 0.016 nm. Hence an FBG with a full width half

maximum (FWHM) of 0.2 nm will have ~12 modes above 50% reflectivity. This suggests that only a few modes will be above the threshold reflectivity for laser action and that the laser may well be single mode. This possibility is examined later where a high frequency photodetector (20 GHz) InGaAs p-i-n diode is used in conjunction with a spectrum analyser to detect any optical mode-mode beat signals. Any acoustically-induced strain will give rise to a periodic variation in both the laser cavity length L and also in refractive index n due to the photoelastic effect, thereby shifting the emitted wavelength.

6.5   Fibre laser response to a pressure field.

For light of frequency v in a laser of cavity length L_{FL}, the optical frequency change in the laser output caused by the combined effects of the physical length change and the change in refractive index can be found by calculating the mode spacing shift. This approach is valid for both single and multi-mode lasers. The pressure-induced frequency shift for a laser of cavity length L_{FL} is given by:

$$\Delta v = \frac{c}{2} \Delta\left(\frac{1}{nL_{FL}}\right) = -\frac{c}{2(nL_{FL})^2}\left(n\Delta L_{FL} + L_{FL}\Delta n\right) = -\frac{c}{2nL_{FL}}\left(\frac{\Delta L_{FL}}{L} + \frac{\Delta n}{n}\right) \tag{6.4}$$

Using $v = c/2nL_{FL}$ for the mode spacing (eqn. 6.3) and $\varepsilon = \Delta L_{FL}/L_{FL}$ and substituting into equation 6.4 gives :-

$$\Delta v = -v\left(\varepsilon + \frac{\Delta n}{n}\right) \tag{6.5}$$

Using $\varepsilon = \Delta L_{FL}/L_{FL} = (P/E)(1-2\mu)$ and $\Delta n = -\frac{1}{2}n^3(P/E)(1-2\mu)(2p_{12} + p_{11})$ derived in chapter 2 gives :-

$$\Delta v = -\frac{\Delta L_{FL}}{L_{FL}}\left(1 - \frac{n^2}{2}(2p_{12} + p_{11})\right) \cdot v = -kv\frac{\Delta L_{FL}}{L_{FL}} \tag{6.6}$$

where k is a constant which is proportional to the photoelastic coefficients and the refractive index. P is the pressure in Pa, E is the Young's modulus for silica, (= 70 GPa), μ is the Poisson ratio (= 0.17), p_{12} = 0.27 and p_{11} = 0.12.

For a Mach-Zehnder interferometer with a path imbalance of L_{MZ}, the phase change $\Delta\Phi_{MZ}$ corresponding to a source frequency change of $\Delta\nu$ is given by :-

$$\Phi_{MZ} = \frac{2\pi n L_{MZ}}{\lambda} = \frac{2\pi n L_{MZ}\nu}{c} \rightarrow \Delta\Phi_{MZ} = \frac{2\pi n L_{MZ}\cdot\Delta\nu}{c} \tag{6.7}$$

Substituting the expression for the laser frequency shift derived in equation 6.6 into equation 6.7 gives :-

$$\Delta\Phi_{MZ} = \frac{2\pi n L_{MZ}\cdot\Delta\nu}{c} = -k\nu\frac{\Delta L_{FL}}{L_{FL}}\cdot\frac{2\pi n L_{MZ}}{c} = -\frac{2\pi k\nu}{c}\cdot\Delta L_{FL}\cdot\frac{L_{MZ}}{L_{FL}} \tag{6.8}$$

Hence the interferometer phase change is proportional to the laser length change. More importantly, the phase change is also proportional to the ratio of the M-Z path imbalance to the fibre laser cavity length. Hence the phase change in the laser is effectively amplified by the interferometer by a factor proportional to the ratio $(L_{MZ}\,/\,L_{FL})$. A path imbalance L_{MZ} of 100 metres (or more) is feasible considering the long coherence length (~several km) of the fibre lasers, which in this case have a cavity length of 5 cm. Therefore the phase amplification factor due to the M-Z path imbalance of 100m is ~2000. Consequently very small phase (or frequency) changes in the fibre laser will be significantly increased at the M-Z output.

Of particular interest is the strain value associated with a pressure of Deep Sea State Zero (DSSO), equal to 10^{-4} Pa. The axial strain in the laser for a hydrostatic pressure of DSSO is given by P/E and can be derived using the expression $\varepsilon = \Delta L_{FL}/L_{FL} = (P/E)(1-2\mu)$. Therefore, substituting typical values of Poisson's ratio (0.17), Young's modulus (70Gpa), refractive index (1.5), p_{11} (0.12) and p_{12} (0.27) gives

$$\varepsilon = \Delta L_{FL}/L_{FL} = (P/E)(1-2\mu)\rightarrow\varepsilon \approx 1\,f\varepsilon$$

Where $f\varepsilon$ denotes femtostrain (10^{-15}). For a laser cavity length of 5 cm a strain of 1 $f\varepsilon$ corresponds to a length change of 5×10^{-17} m. To put this figure into some sort of perspective, typical atomic radii are of the order of 10^{-10} m and typical nuclear radii for elements such as iron are of the order of 10^{-14} m. Hence the length changes associated with a pressure field of DSSO are approximately three orders of magnitude less than a typical nuclear radius. It would seem unlikely that a length change of this magnitude could actually be detected. However, experimental results suggest that not only can this sensitivity be achieved but exceeded given the appropriate experimental arrangement.

Also relevant is the acoustic pressure-induced wavelength shift in the FBG peak wavelength. The analysis of the laser wavelength changes assumes that only the fibre laser cavity is affected by the acoustic field while the FBG reflectivity peak remains unchanged. The change in the FBG peak reflectivity value is calculated below using values of peak acoustic pressure $P = 1\text{Pa}$, Young's modulus $E = 70$ GPa, refractive index $n = 1.5$, Poisson's ratio $\mu = 0.17$, stress-optic coefficients $p_{12} = 0.27$ and $p_{11} = 0.12$. This gives a fractional wavelength shift $\Delta\lambda$ for a 1550 nm grating of :-

$$\Delta\lambda = \lambda\left[\left(\frac{P}{E}\right)(1-2\mu) - \frac{n^2}{2}\left(\frac{P}{E}\right)(1-2\mu)(p_{11} + 2p_{12})\right] \approx 2.5\times10^{-8}\,nm \qquad (6.9)$$

Hence the change in the FBG peak reflectivity due to the typical acoustic pressures in these experiments is negligible and can be ignored in further analysis.

The effect of a pressure field on the fibre laser polarization modes is discussed next, along with the application of changes in the laser polarization mode frequencies towards constructing polarimetric fibre laser strain sensors.

6.6   Polarimetric Fibre laser Strain Sensors.

A polarimetric fibre laser sensor is based around the stress-induced beat frequency between the orthogonal polarisation modes of a single or multimode fibre laser. As discussed previously, an optically resonant cavity of length L allows resonances at optical frequencies $v_N = cN/2nL$, where N is an integer denoting the N'th optical mode, c is the velocity of light (in vacuo) and n is the fibre core refractive index. This beat frequency arises due to stress-induced birefringence in the fibre, which causes the mutually orthogonal X,Y longitudinal polarisation modes to experience different refractive indices. An external stress applied to the fibre causes the normally isotropic refractive index of the fibre core to become anisotropic, as discussed in previous chapters. For polarisation modes at the same frequency in an unstressed fibre no polarisation mode beating will occur. In cases where the fibre has an intrinsic birefringence there will be some frequency difference between polarisation modes [19,20], and mode beating can occur when the modes are combined using some form of polarization analyzer. These ideas are illustrated for a single mode laser operating in two orthogonal polarisation modes with no intrinsic fibre birefringence. This is shown in figure 6.10 for an <u>anisotropically</u> strained and unstrained laser.
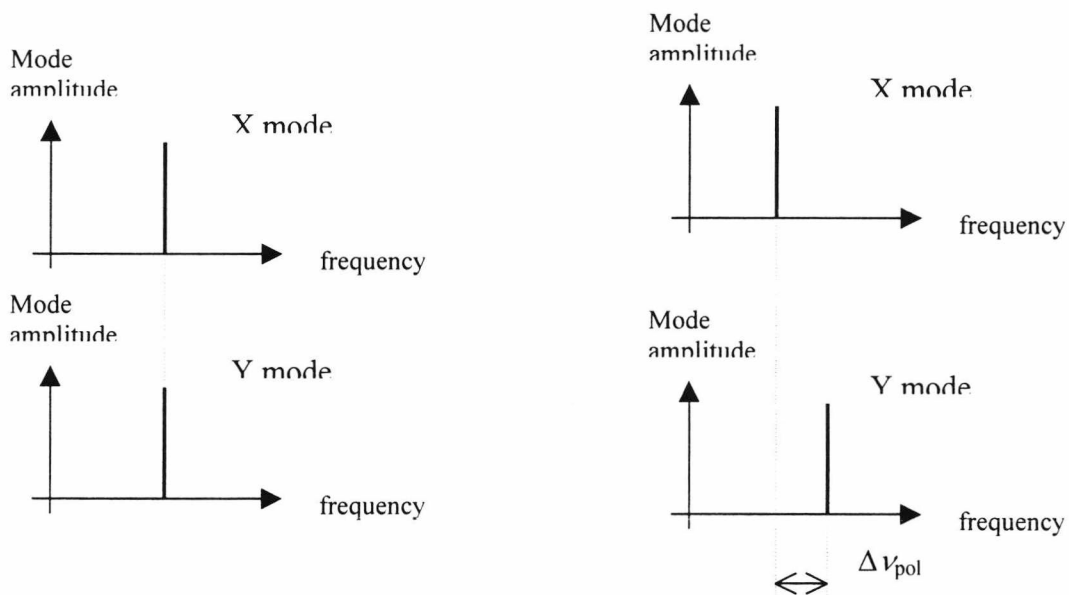
(i) Unstrained case, $\Delta v_{pol} = 0$.   (ii) Anisotropically strained case, $\Delta v_{pol} > 0$.

Figure 6.10 Polarisation mode frequency shift in anisotropically strained fibre laser.

As the modes are orthogonal no mode beating at Δv_{pol} will occur unless the modes are combined using a polariser before being incident on a photodetector. Birefringence induced polarisation mode frequency shifts in fibre lasers have been used to construct strain sensors, as demonstrated in [19,20]. Results in [19,20] are quoted in terms of (Δv_{pol}/millistrain), which is not directly comparable with the acoustic sensitivity figures given before for the different hydrophone array multiplexing schemes.

 In [19,20], the fibre pressure was applied externally by sandwiching the fibre between two horizontal metal plates and simply applying small masses to the plates to induce birefringence. Over a 5cm fibre length and a typical cross-sectional fibre diameter of 125μm, even a modest force of 1N can give rise to axial stresses of the order of 10^5 Pa, far in excess of the acoustic pressures experienced here. This suggests that polarimetric fibre laser sensors are not a viable approach towards constructing a high sensitivity acoustic sensor, as large axial stresses are required to produce a measurable polarisation mode frequency shift.

6.7   Experimental Investigation of Distributed Bragg Reflector lasers.

The output powers for two DBR lasers were measured using the simple experimental arrangement shown below in figure 6.11:-
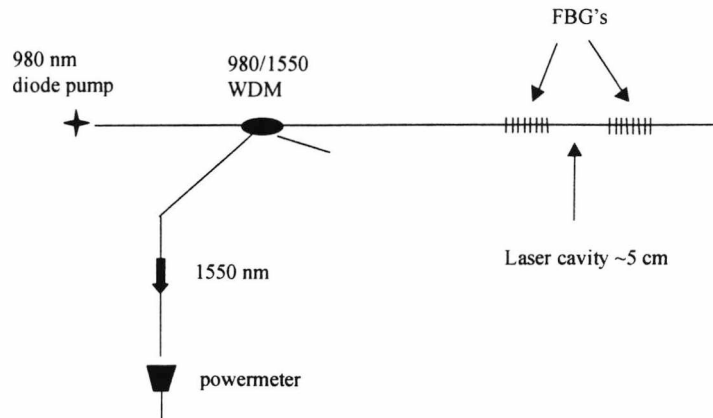
Figure 6.11 – Measurement of laser threshold pump power

The 980 diode pump is a commercially available unit (LDC 200) which allows accurate control over the pump intensity. The output from this pump source was fusion spliced to a standard telecoms 980/1550 WDM coupler with an insertion loss of < 0.3 dB providing > 18 dB of isolation over a 1530-1560 nm bandwidth. This allows the pump and laser source to be effectively decoupled before reaching the detector.
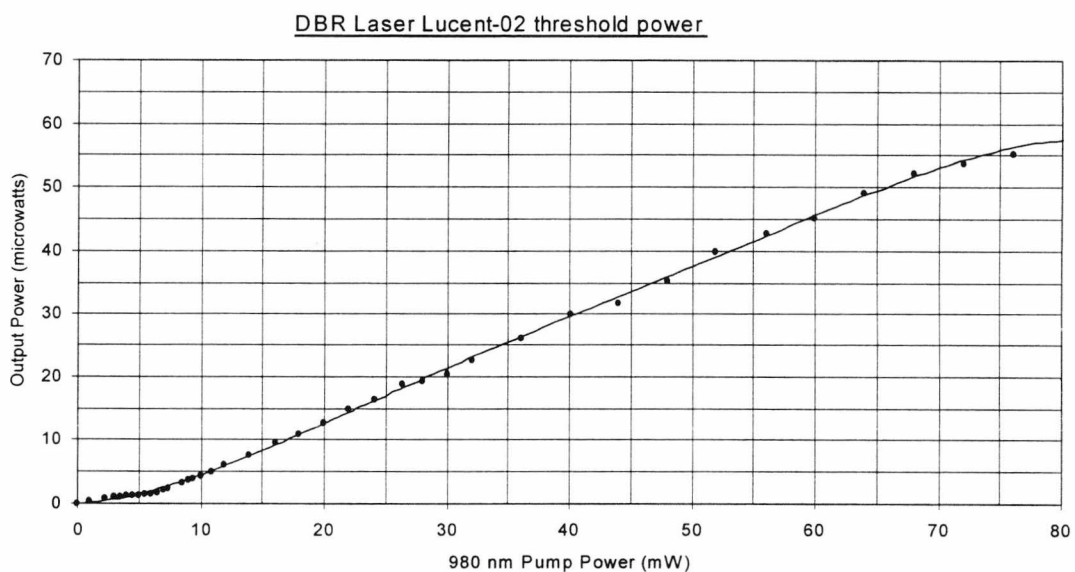
Figure 6.12 – DBR laser Lucent-02 output power as a function of pump power

As can be seen from figures 6.12 and 6.13, the power output for the laser built in Fibercore fibre is considerably higher than that for the Lucent laser. This may be due to different doping levels in the two fibres, as the fibres were sourced from two different manufacturers (Lucent Technologies and Fibrecore). The fibre laser properties are summarized below in table 6.2.

Fibre laser type	Erbium fibre type	Grating bandwidth	Laser wavelength (nm)	Laser cavity length	Erbium fibre attenuation @ 1550 nm
Lucent DBR	981344380002	~0.05 nm	1568	5 cm	12.6 dB/m
Fibrecore2 DBR	DF1500F-0980	~0.05 nm	1548	5 cm	5.7 dB/m

Table 6.2 DBR fibre laser properties

The lasers were supplied by the Photonics Research group at Aston University. The lasers had been previously spliced onto ~1m of Corning SMF-28 fibre. One feature of the Fibrecore laser was that the temperature of the FBG nearest to the pump source had to be raised by approximately 30-40°C above ambient in order for laser action to take place. This suggests that some wavelength mismatch between the FBG's occurred during manufacture. The need to heat the FBG by some external means obviously precludes the use of this laser for any operational system. However, the laser output characteristics could still be determined experimentally by using a soldering iron positioned closely to the FBG to provide heating.
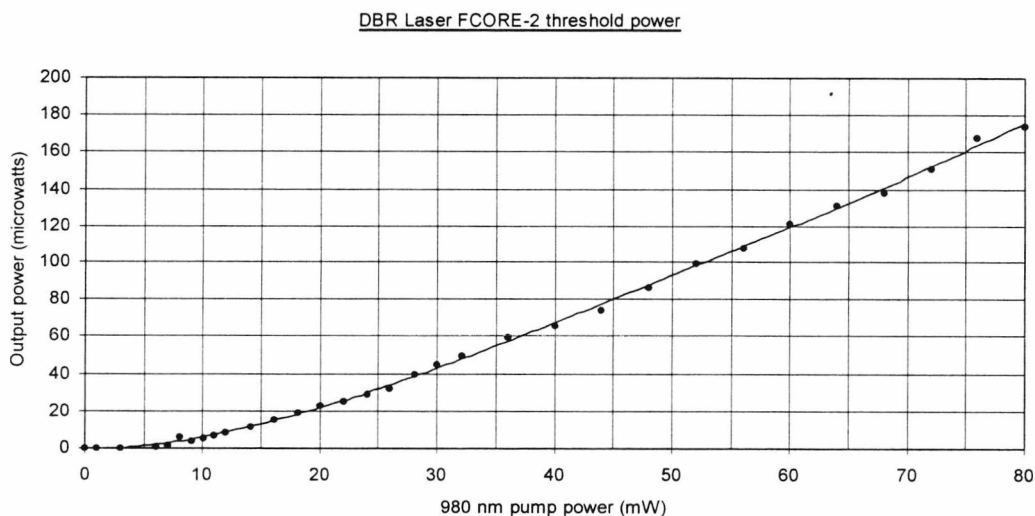
Figure 6.13 – DBR laser Fibrecore2 output power as a function of pump power.

The laser wavelengths were 1568 nm and 1548 nm for the Lucent and Fibrecore lasers respectively. To remove the effects of any spurious environmentally induced phase shifts in the interferometer, the acoustically-induced laser wavelength and hence phase change is downshifted by an acousto-optic Bragg cell in one arm of the interferometer. The Bragg cell is a commercially available fibre pigtailed unit model MO408J-FxS (from manufacturers Gooch and Housego) with an insertion loss of < 2.4dB. The RF driver used to modulate the Bragg cell was driver model A114, with a 40 MHz output at a maximum output of 1.6 W RF. The 980 pump laser is also a commercially available unit (model LDC 200, manufacturers Sifam Optics) with inherent stabilization to suppress the relaxation oscillations common to solid-state lasers. All fibre used in the interconnections between components was single-mode telecoms fibre (Corning SMF-28). The optical isolator was a standard telecoms isolator with an insertion loss < 0.3 dB providing >18dB of isolation. All fibres were fusion spliced, the optical losses for each splice being of the order of 0.1 dB.
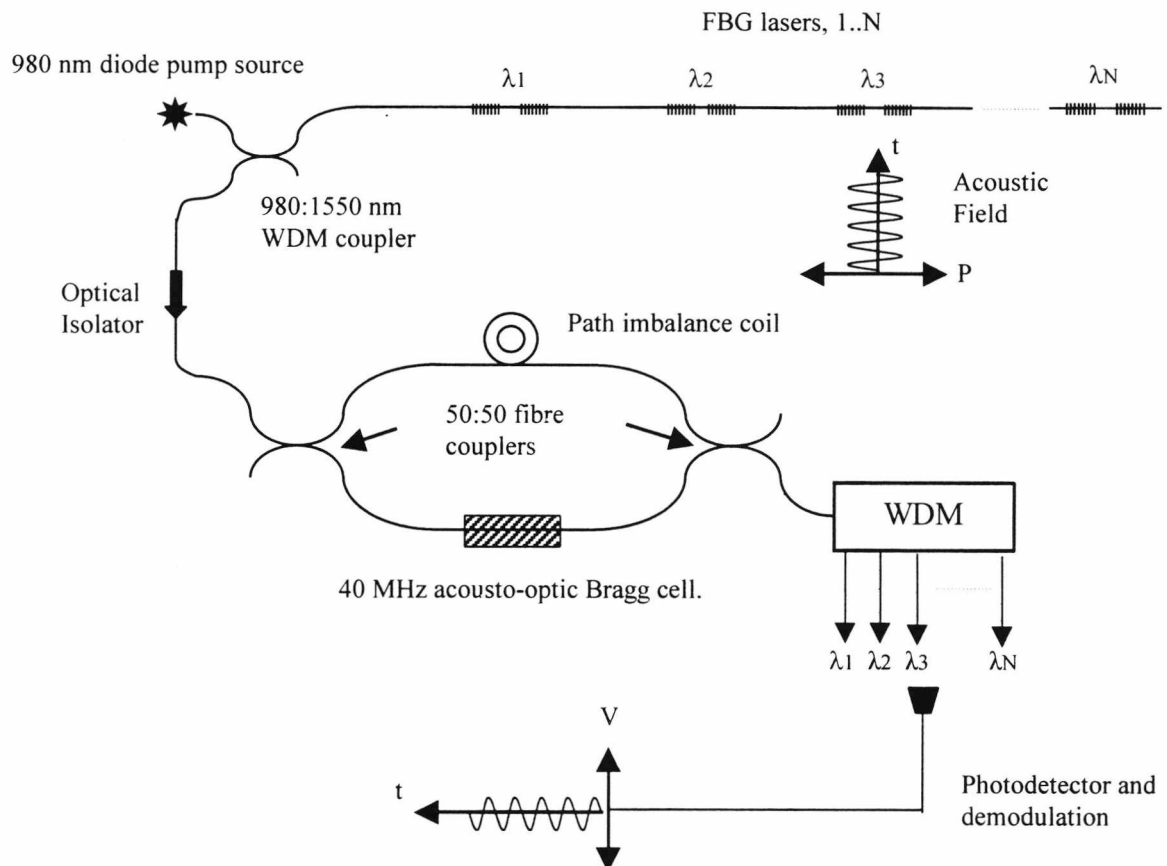
Figure 6.14 – Wavelength Division Multiplexed FBG laser based acoustic detection system.

In figure 6.14, the photodetector consisted of an InGaAs pin diode coupled to an amplifier unit with a amplification bandwidth of DC-125 MHz (from manufacturers New Focus, model 1811-FC). The acoustic signal is heterodyned with the carrier frequency generated by the Bragg cell, and appears as sidebands on either side of the 40 MHz carrier. The number of sidebands and the sideband amplitude are determined by the acoustic modulation depth. For high acoustic field strengths several sidebands were apparent. The acoustic field amplitude was measured with a calibrated electret microphone close to the fibre laser. As the wavelengths were significantly different a preliminary demultiplexing experiment was attempted to assess the feasibility of demultiplexing the lasers with a simple diffraction grating arrangement (see fig 6.15 overleaf). In the system shown in fig 6.15 overleaf both the Fibrecore and the Lucent lasers were used. WDM was accomplished using a 600 lines/mm planar blazed diffraction grating and some collimating optics (10× microscope objective) as shown in figure 6.15. This was found to work well but needed careful mechanical adjustment to maximise the signal. Demodulation of the photodetector output signal was accomplished using a RF spectrum analyser with a FM demodulation function. This allowed the original acoustic signal to be recovered and to be routed into a second acoustic frequency spectrum analyser (model HP 3561-A) for further measurement. Amplification of the small acoustically-induced optical phase changes is provided by the path imbalance coil, which in this case was 100m. The system shown previously in figure 6.14 will also function extremely well as an acoustic detector by virtue of having a large path imbalance coil, which is the basic principle behind currently available optical hydrophones. Hence shielding the path imbalance coil from spurious acoustic pickup is of primary importance in determining the system noise floor. All fibre used in constructing the interferometer was Corning SMF-28 standard telecommunications single-mode optical fibre with an attenuation of ~0.15 dB/km at 1550 nm, from the manufacturers specifications.

Diffraction grating

1st order diffraction lines, $\lambda1, \lambda2$

Collimated beam

Microscope objective

p-I-n diode detector and microscope objective on linear translation stage.

Fibre input
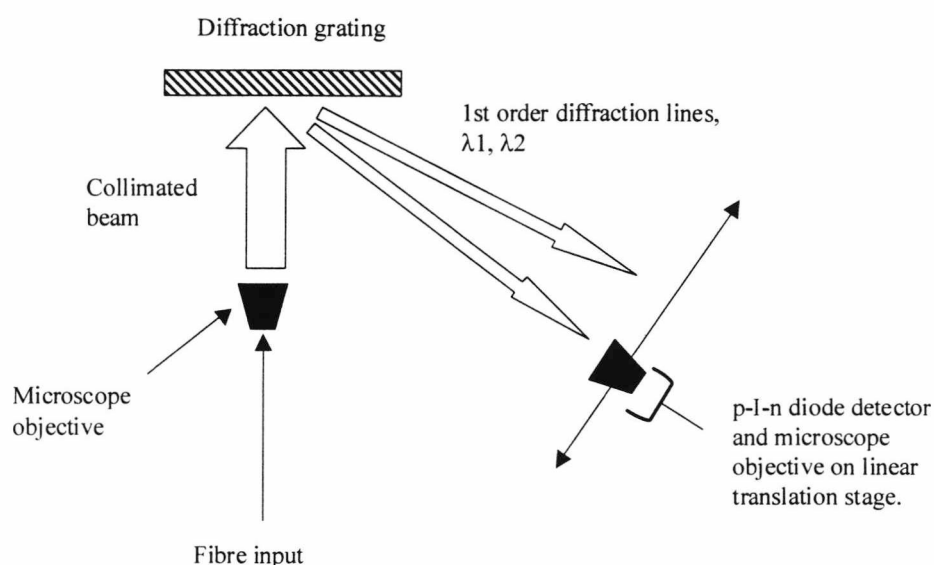
Figure 6.15 – Optical demultiplexing using a diffraction grating.

Acoustic shielding of the path imbalance coil was provided by firstly enclosing the fibre coil in the rigid plastic protective case that the coil was originally supplied in. This was then placed in a box containing expanded foam pieces to provide further acoustic absorbtion. Finally the box was enclosed on four sides by 1 inch wooden boards and on the top and bottom by rigid steel plate. With this shielding arrangement in place the lasers were acoustically excited in turn using a small speaker and a signal generator producing a sine output in the range 200Hz-20 kHz. and the acoustic sensitivity of the system assessed. The calibrated electret microphone response was effectively (+/- 0.5 dB) flat over the frequency range 200Hz-20kHz with a response of 31.2 mV/Pa and it was over this frequency range that the laser acoustic responsivity was assessed. To further reduce the possibility of spurious pickup in parts of the interferometer not associated with the path imbalance coil both the speaker and microphone were enclosed in a mount that covered the laser and helped to localize the acoustic signal. With these precautions in place the acoustic response of both lasers was assessed. The acoustic responses of both the Lucent and Fibrecore lasers are given below in figures 6.16 and 6.17 respectively.
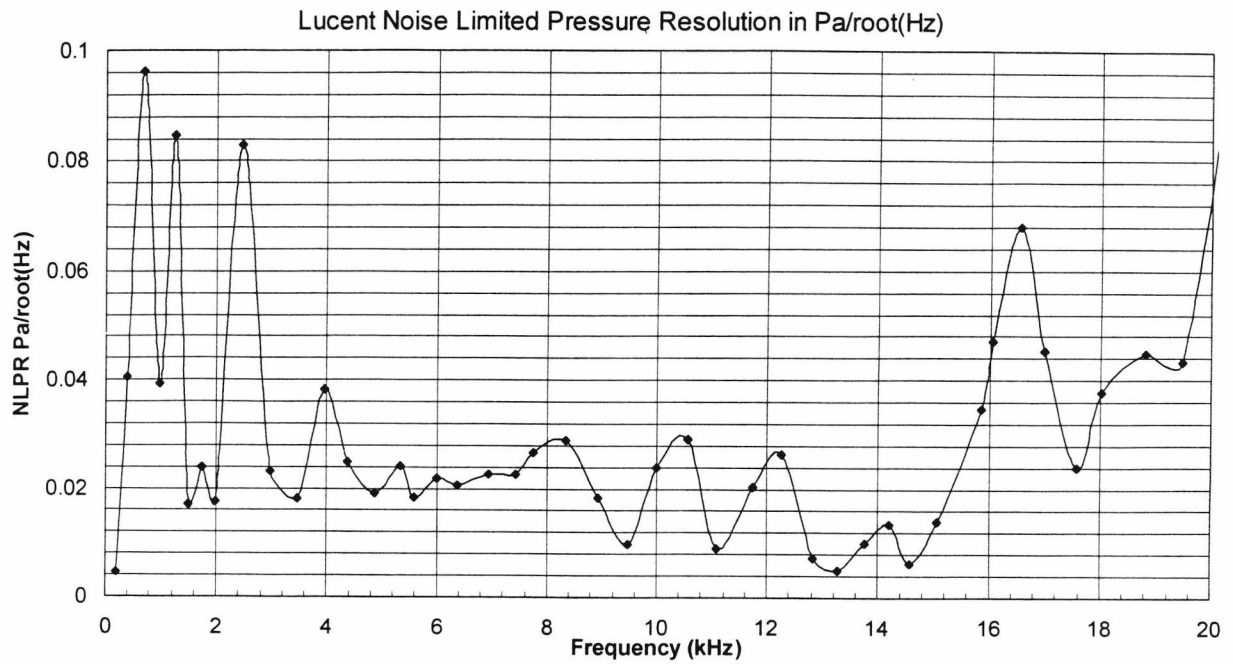
Figure 6.16 Lucent fibre laser NLPR with 100m path imbalance
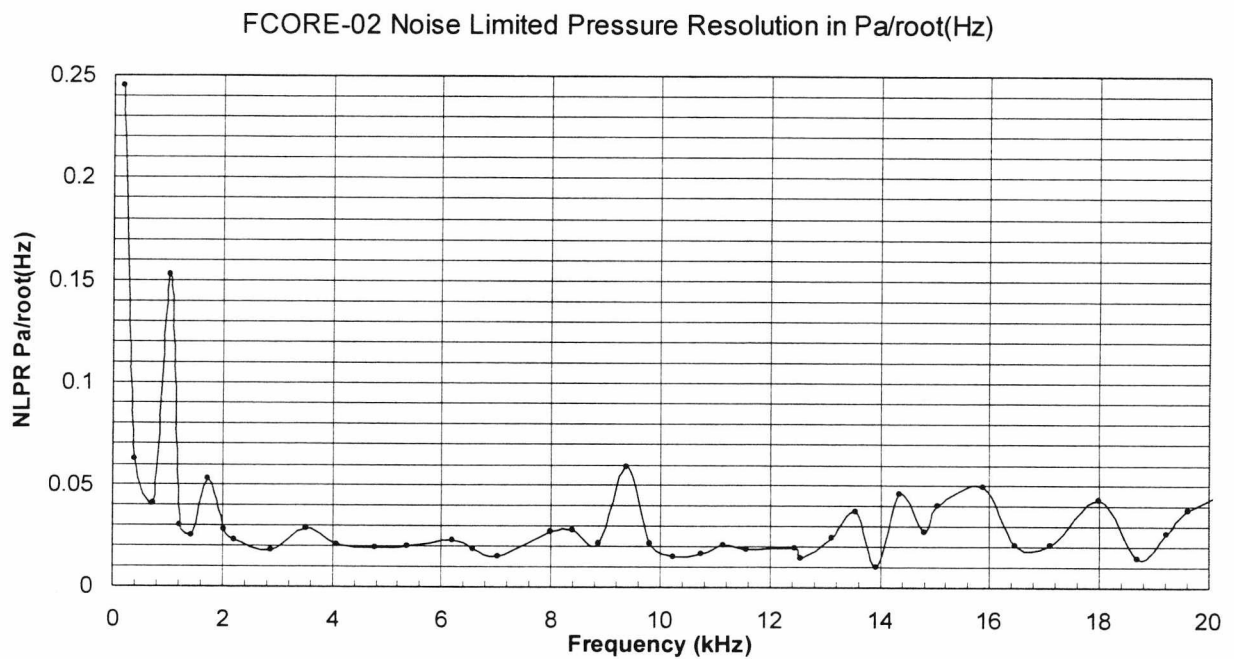
Figure 6.17 Fibrecore laser NLPR with 100m path imbalance.

The noise limited pressure resolutions given in figures 6.16, 6.17 are at best only an indication of the true laser acoustic sensitivity for a number of reasons. As the lasers were only loosely mounted on a rigid support the possibility exists of mechanical resonances in the fibre which may give rise to anomalous frequency responses. Also, the electret microphone was a few cm away from the fibre laser, hence this is a source of some uncertainty in the acoustic field pressure. The noise limited pressure resolutions (NLPR) are given in Pa/$\sqrt{Hz}$. As the acoustic detection sensitivity is directly proportional to the interferometer path imbalance (see previous analysis), the path imbalance was increased from an initial value of 100 metres to 4.2 km and the NLPR re-measured for the Lucent laser. The results of this investigation are given in figure 6.18 below.
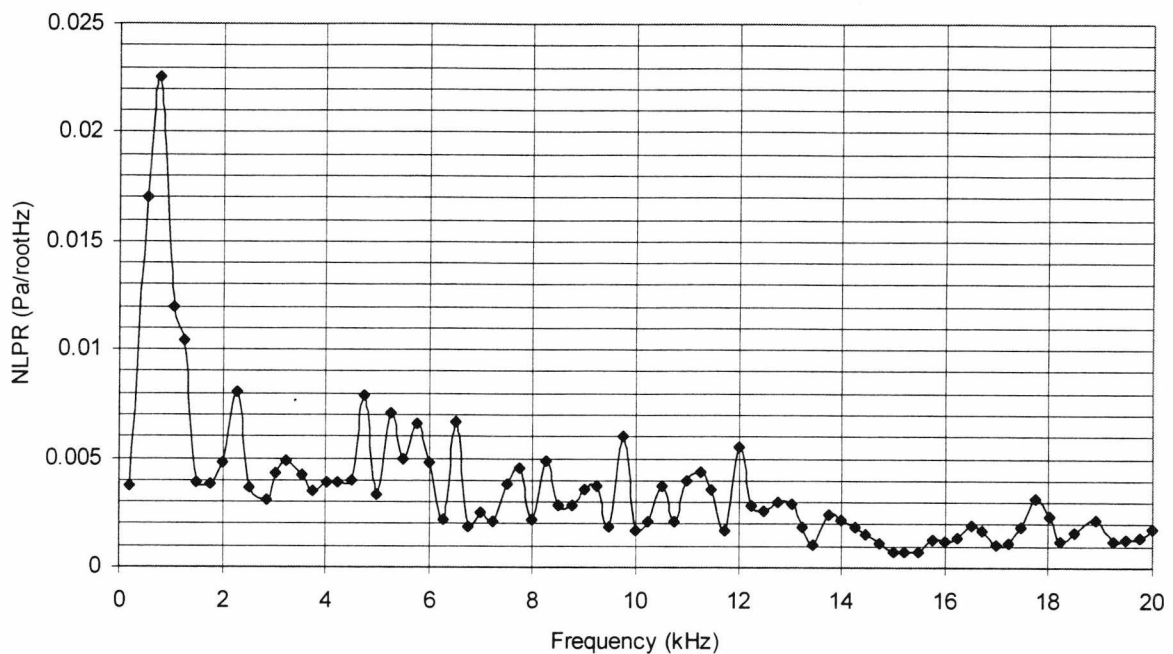
Figure 6.18 Lucent laser acoustic response with 4.2 km path imbalance.

Referring back to figure 6.16 over the range 4-6 kHz, a NLPR of ~0.02 Pa/$\sqrt{Hz}$ corresponds to a strain resolution of ~270 fϵ/$\sqrt{Hz}$. As can be seen from figure 6.18, the NLPR for a 4.2 km interferometer path imbalance has improved significantly over that for a 100 metres path imbalance. Although significant differences can be seen in the acoustic frequency response for the two Lucent laser plots, figure 6.18 shows a NLPR

of ~0.004 Pa/√Hz at around 4 kHz, corresponding to a noise limited strain resolution of ~50 fε/√Hz. This compares very favourably with the figure of 56 fε/√Hz from [14,15]. These results are summarized in Table 6.3 for both of the DBR lasers and also for the study of [14,15] .

Laser type	λ(nm)	M-Z Path imbalance (m)	Measurement frequency (kHz)	Noise limited Pressure Resolution (Pa/√Hz)	Noise limited strain Resolution (fε/√Hz)
Lucent DBR	1568	100	4-6	~0.02	~270
Fibrecore DBR	1548	100	4-6	~0.02	~270
Lucent DBR	1568	4200	4-6	~0.004	~50
2.5 cm DBR [14,15]	1554	100	7	~0.005	~56

Table 6.3 Noise limited pressure and strain resolutions from preliminary diffraction grating demultiplexing experiment.

Hence a very high strain sensitivity can be achieved even with the relatively crude diffraction grating demultiplexing and signal demodulation used here. No attempt was made during these preliminary experiments to fully analyse the relative importance of the various noise sources within the system. The aim was to establish the feasibility of using fibre lasers as acoustic sensors with a heterodyne interferometric interrogation system. These preliminary experiments strongly suggested that a more detailed investigation of the potential of this system was warranted and that with some modifications to various parts of the experimental setup a significantly higher acoustic detection sensitivity could be readily achieved. Hence the system shown in figure 6.14 was modified in order to enhance the acoustic detection sensitivity and to further investigate the possibility of a more efficient demultiplexing scheme. This forms the basis of subsequent sections of this chapter, along with the results from investigations of an array of distributed feedback (DFB) lasers.

6.8   Distributed Feedback (DFB) Fibre Lasers.

The lasers used in the experiments described previously consisted of a resonant cavity formed by two FBG's in the doped fibre core. These lasers may well be multimode with the associated possibility of mode hopping which could potentially give rise to a non-linear response as the acoustic field intensity and hence the cavity strain is increased. This possibility was investigated for the two DBR lasers used previously by looking for mode-mode optical beat frequencies using a high frequency (20GHz) InGaAs p-I-n diode detector coupled to a spectrum analyser of a comparable frequency range. As the calculated mode spacing was around 2GHz for the DBR lasers any mode-mode beat signals should have been apparent on the spectrum analyser. As none were seen this strongly suggested that the particular lasers used in these preliminary measurements were in fact single mode, although this was fortuitous, as other lasers not used in experimental measurements were tested and found to be multimode.

A more preferable laser from the point of view of constructing a sensor would be single mode. Such a laser can be manufactured by having a few cm length FBG in a doped fibre core with a $\pi/2$ phase shift in the middle of the grating. Such a laser is known as a distributed feedback (DFB) laser [16] and is inherently single-mode and stable. These lasers are commercially available at any wavelength within the Er^{3+} gain profile. Four of these lasers were obtained at lasing wavelengths of 1550.97, 1554.28, 1556.54 and 1560.55 nm. The DFB lasers were IONAS model number IFL01W1E, which had an output power specified at 100 µW at a pump power of 100mW (1480 nm) coupled with a linewidth of less than 30 kHz. The wavelength spacings correspond to the International standard wavelength (ITU) schedule of 3.2 nm or 400 GHz. This allowed demultiplexing using a commercially available thin-film based bandpass wavelength division multiplexer (BWDM), model AN-096001 from manufacturers E-TEK. The key component of the BWDM filter is a thin-film dielectric interference coating on a glass or polymer substrate. The interference coatings consist of alternating thin layers of high and low refractive index materials such as SiO_2 and Ta_2O_5. The multiple coating layers form dielectric cavities that selectively transmit or reflect light depending on the wavelength. The lasers were constructed so has to have a one-to-one wavelength correspondence with the bandpass response of this commercially available

device. As the BWDM is fully connectorised with FC/PC connectors spurious optical losses are minimised. Preliminary measurements were in agreement with the specified losses of the BWDM of between 2.5 - 3 dB per channel. The optical bandpass filter width is approximately 0.8 nm, so temperature-induced shifts in the DFB laser wavelengths (which would be significantly less than 0.8 nm) would not adversely effect the system sensitivity. Only 4 of the available 8 channels were required in the experiments here.

6.8.1   Threshold Pump Power measurements on DFB lasers.

As the DFB lasers would eventually be spliced into a linear array the initial measurements were of the laser threshold pump powers, as the laser with the highest threshold would be the one chosen to be nearest the pump source, and so on until the laser with the lowest threshold at the end of the array. This is because in an array containing several tens of lasers, the pump power would be gradually absorbed in successive lasers along the array. Each laser was individually spliced onto the system shown previously in figure 6.13 and the laser output power measured directly after the optical isolator. The results of the power measurements on all four lasers are shown overleaf in figure 6.19. As a pump source at 1480 nm was not available at the time, all measurements were taken with a pump wavelength of 980 nm. The threshold powers for each laser are not immediately obvious from figure 6.19, and have been tabulated separately in table 6.4 below along with the maximum laser output power at 80 mW pump.

DFB Laser Wavelength (nm)	Laser threshold power (mW)	Laser output power (µW) at 80 mW of 980 nm pump power.
1550.97	6.3	32.8
1554.28	9.0	25.0
1556.54	6.6	39.7
1560.55	6.0	22.0

Table 6.4 – DFB laser threshold powers and maximum output power.

DFB Lasers Output Powers @980 nm pump
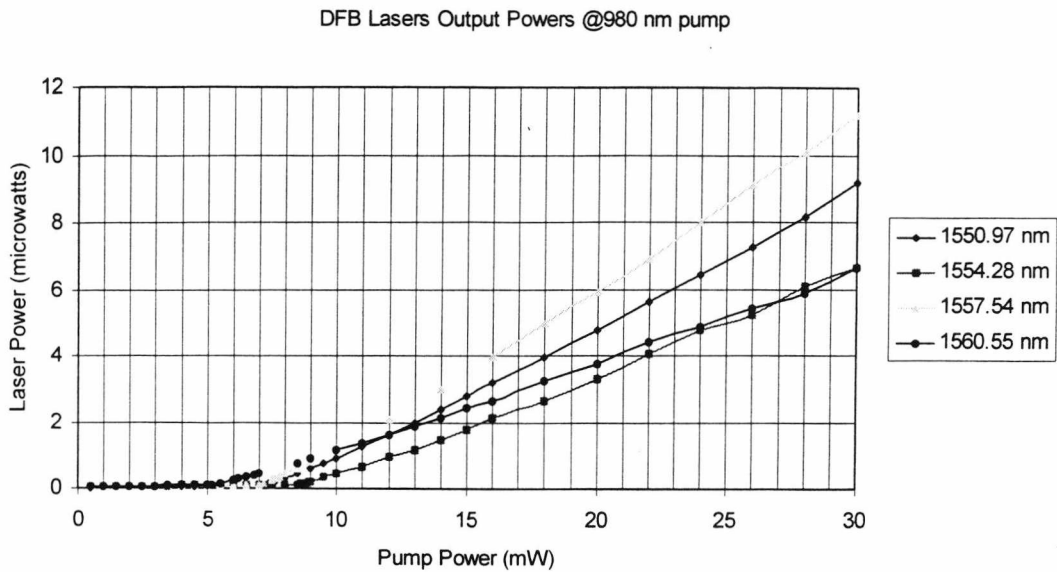
Figure 6.19 – Threshold power measurements on DFB lasers

The threshold powers will also be dependent on the splice losses, as each laser was spliced on separately in order to give a more accurate measurement. However the figures in table 6.4 are thought to be accurate due to the small splice losses (~0.1dB) given by the automatic fusion splicer. Hence from table 6.4, the laser order in the array (starting nearest the pump) would be: 1554.28, 1556.54, 1550.97 and 1560.55 nm. This threshold power consideration is probably not particularly important for the small number of lasers used here, as there is easily sufficient pump power available to excite all lasers simultaneously. However, for an array containing several tens of lasers, as would be the case in a working hydrophone array, considerations of threshold power and pump power distribution would be of primary importance as the pump would be gradually absorbed in successive lasers along the array.

6.8.2   Initial investigations of DFB lasers.

The initial investigations of the DFB array consisted of experimental measurements of the system noise sources. Several noise sources contribute to the overall system noise. These are as follows:

6.8.2.1   Optical shot noise limit.

This is a fundamental and irreducible noise limit due to the quantisation of light into photons with energy $h\nu$, h being Planck's constant and ν the optical frequency. The shot noise limit therefore provides a useful baseline against which to compare other noise sources, and sets a lower limit to the detected relative intensity noise. The magnitude of the root mean square (rms) shot noise current i_{SHOT} in the photodetector in a 1 Hz bandwidth is given by the following expression [17]:

$$i_{SHOT} = \left(2ei_{PHOTO}\right)^{\frac{1}{2}} = \left(2eRP_{OPT}\right)^{\frac{1}{2}} \tag{6.12}$$

where i_{PHOTO} is the detector photocurrent, and is given by the product of the detector optical responsivity R in Amps/Watt and the incident optical power P_{OPT}. Assuming a typical detector responsivity of 0.9 at 1550 nm for an InGaAs photodetector [17] and an incident optical power of 1 microwatt the shot noise current is $\sim 5.09 \times 10^{-13}$ A. Hence in terms of dB the shot noise floor is given, in this case , by:

$$dB = 20\log_{10}\left(\frac{5.09\times10^{-13}}{9\times10^{-7}}\right) \sim -125 \ dB/\sqrt{Hz} \tag{6.13}$$

6.8.2.2   Laser relative intensity noise (RIN).

This is a consequence of random fluctuations in the laser output power. Spontaneous emission of radiation into the laser mode by atoms dropping from upper energy levels into lower levels is incoherent with respect to the laser mode, hence the laser output is subject to both amplitude and phase fluctuations. The RIN is defined over a 1 Hz bandwidth and is given by:- $RIN = \left(\Delta P(t)\right)^2/\langle P(t)\rangle^2$ [17] where $\Delta P(t)$ is the instantaneous laser noise power and $\langle P(t)\rangle$ denotes the average laser power. The units of RIN are usually expressed in dB/√Hz.

6.8.2.3   Laser phase noise.

This is a consequence of the finite laser linewidth and can be a significant noise source for an interferometric interrogation system as used here [21,22,23], as the laser phase noise is effectively amplified by the interferometer path imbalance. Again this is an irreducible noise source and cannot be minimised by further signal processing techniques.

6.8.2.4   Laser relaxation oscillations.

Relaxation oscillations have been observed in most types of solid-state lasers [17]. The relaxation oscillations are a function of the pump power and were readily seen for all four DFB lasers, as well as the two DBR lasers investigated previously. The relaxation oscillations can be seen as sidebands on the 40 MHz carrier frequency generated by the Bragg cell, and on an oscilloscope can be easily seen as large amplitude spikes in the laser output power. Figure 6.20 explains the physical origin of spiking occurring when a laser is switched on.
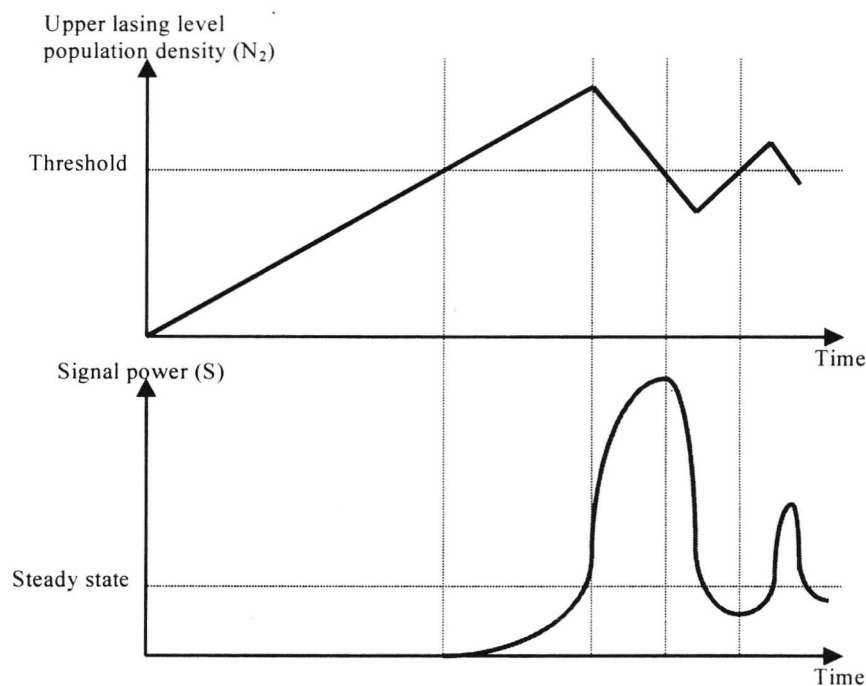
Figure 6.20 – Laser relaxation oscillations.

Initially the signal power in the cavity is almost zero being only a result of spontaneous emission. This situation endures until the population density of the upper lasing level is pumped up to threshold. Once it exceeds threshold the signal power begins to rise rapidly, but it takes a finite time to reach the steady state value, during which time the population of the upper lasing level has gone well beyond threshold. The signal power therefore continues to rise reaching a peak many times the steady state value before the now reducing upper lasing level population goes below threshold and causes the signal power to fall. This process of overshooting continues many times with the excursions gradually becoming smaller, less like spikes and more sinusoidal in nature. These lightly damped sinusoidal oscillations are known as relaxation oscillations. In the ideal system described above the laser output will tend toward the steady state level. In the lasers used here this spiking could be seen even when the laser had been on for some time. This is because the system is only weakly stable; anything that perturbs a parameter of the system (pump power, mirror reflectivity, birefringence in the cavity, back-reflection, acoustic fields) can cause spiking and oscillations. A typical relaxation oscillation frequency at 80 mW pump is of the order of several tens of kHz. Although not implemented here, an effective method of actively suppressing the relaxation oscillations is to have a monitor photodiode on the laser output which is in turn fed to the pump source using an active control loop to alter the pump power in a direction so as to suppress the oscillations. This will work effectively for one laser but is not possible in an array of fibre lasers.

6.8.2.5 Optical pump noise.

This will add to the intrinsic RIN noise figure described above. This can be minimised by having an actively stabilised laser pump source, as was the case here.

6.8.2.6 Thermodynamic phase noise

This is a consequence of random microscopic thermodynamic fluctuations in the fibre core which give rise to density and hence optical path length fluctuations. As the path

imbalance coil contains the greatest length of fibre in the system it is there that this effect will be most pronounced. This in turn gives rise to a source of phase noise in addition to that of the intrinsic laser phase noise. [21,22,23]. The magnitude of this noise source is discussed later in this chapter.

6.8.2.7 Amplifier noise

This can be reduced by a judicious choice of the correct detection system. In this case the detectors used were InGaAs p-i-n diodes with a very low noise transimpedance amplifier chip specifically designed for optical detection applications. In this case a commercially available low-noise transimpedance amplifier module model 1811-FC (from manufacturers New Focus) with a 125 MHz bandwidth was used.

Given the existence of these various noise sources the primary experimental aim was to determine the relative importance and magnitude of each noise source, either by experiment where possible or by reference to previous work where appropriate.

6.9   Modifications to Original Experimental Setup

Acoustic pickup in the path imbalance coil and other parts of the interferometer would largely invalidate any noise measurements. Hence the Mach-Zehnder interferometer part of figure 6.14 was enclosed in a steel vacuum vessel originally intended for liquid nitrogen storage. The open end of the vessel was filled with ~10cm of acoustically absorbing material and finally capped with ~3 cm of steel plate. The vessel was then mounted on a vibration isolated optical bench. This arrangement is shown schematically overleaf in figure 6.21.
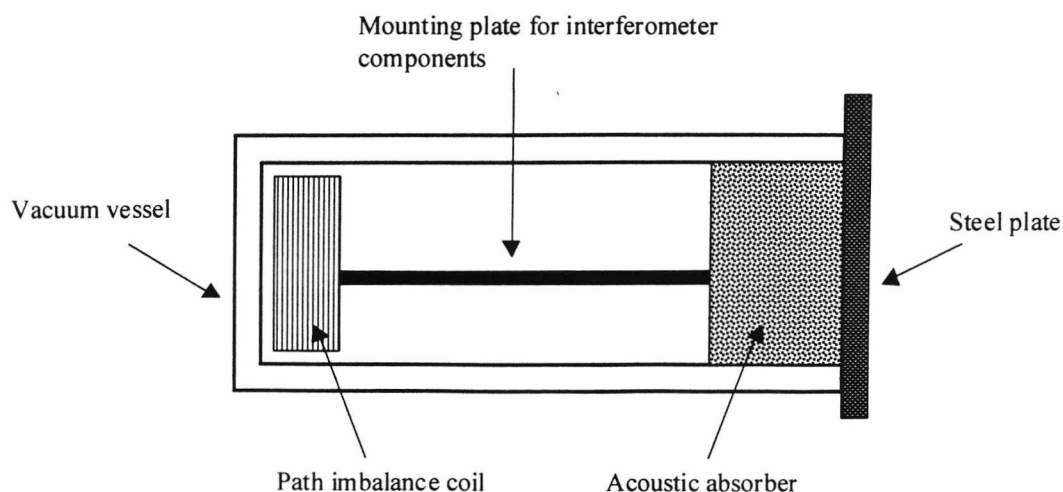
Figure 6.21 – Further Acoustic Isolation Measures

A small hole in the side of the steel plate allowed access for optical fibres to connect to other parts of the optical system, specifically the pump source, WDM section and also the fibre lasers. When acoustic sensitivity measurements were being made the lasers were external to the vacuum vessel. For phase and intensity noise measurements only one laser was spliced into the system and this laser was in turn isolated inside the vacuum vessel. Hence all sections of the optical system which could potentially be subject to background acoustic pickup were isolated from the environment.

6.9.1 Fibre Laser Coherence length measurement.

A delayed self-heterodyne technique [24,25,26] was used to assess the coherence length l_C, or to at least find a lower bounding value for all the lasers used in the experiments. The Mach-Zehnder interferometer functions as an autocorrelator for the optical signals. It can be shown mathematically [17] that for a path imbalance greater than the laser coherence length the Fourier transform of the autocorrelation function (denoted by $C_V(t)$) is the spectral source density function (denoted by $S_V(\omega)$). The two parameters are related by the Wiener-Khintchine theorem, which states that $C_V(t)$ and $S_V(\omega)$ form a Fourier transform pair. The experimental setup consisted of the system shown in figure 6.13 but with only one laser spliced on at a time, hence no WDM was required. The path imbalance was 25.6 km, and the Fourier transform of the

interferometer output was provided by a RF spectrum analyser. The results from measurements taken on all six lasers are given in Table 6.5, along with the manufacturers bounding measurements of the linewidths for the DFB lasers.

Wavelength (nm)	Measured linewidth (kHz)	Stated linewidth (kHz) from specifications
1568 (Lucent DBR)	<15	-
1548 (Fcore DBR)	<15	-
1550.97 (Ionas DFB)	<10	<10
1554.28 (Ionas DFB)	<15	<15
1556.54 (Ionas DFB)	<16	<10
1560.55 (Ionas DFB)	<20	<20

Table 6.5 – Measured DBR and DFB laser linewidths.

From [17], the spectrum consists of a Lorentzian distribution centred on the 40 MHz carrier generated by the Bragg cell. The laser linewidth was taken to be half of the spectral peak width measured at the full width half maximum (FWHM). As can be seen from Table 6.5, there is good agreement between the experimentally measured bounding values of the linewidths and the stated linewidths from the maker's specifications. A value of l_c of the order of 10 kHz corresponds to a coherence time of 10^{-4} seconds and hence a minimum coherence length in fibre of 20 km. Hence the value of l_c is unlikely to be the limiting factor in determining the system sensitivity to acoustic signals.

6.10   Noise Measurements

6.10.1   Relative Intensity Noise (RIN)

To measure the intensity noise the laser output was simply fed into a spectrum analyzer, model HP3561-A. The measured signal power was then normalised to a 1 Hz bandwidth. Typical relative intensity noise spectra for one of the lasers (Ionas 1550.97nm DFB) are given in figures 6.22, 6.23 for two pump powers, one at 40 mW pump and the other at 80 mW.

RIN for 1550.97 nm DFB laser, 40mW pump @980nm
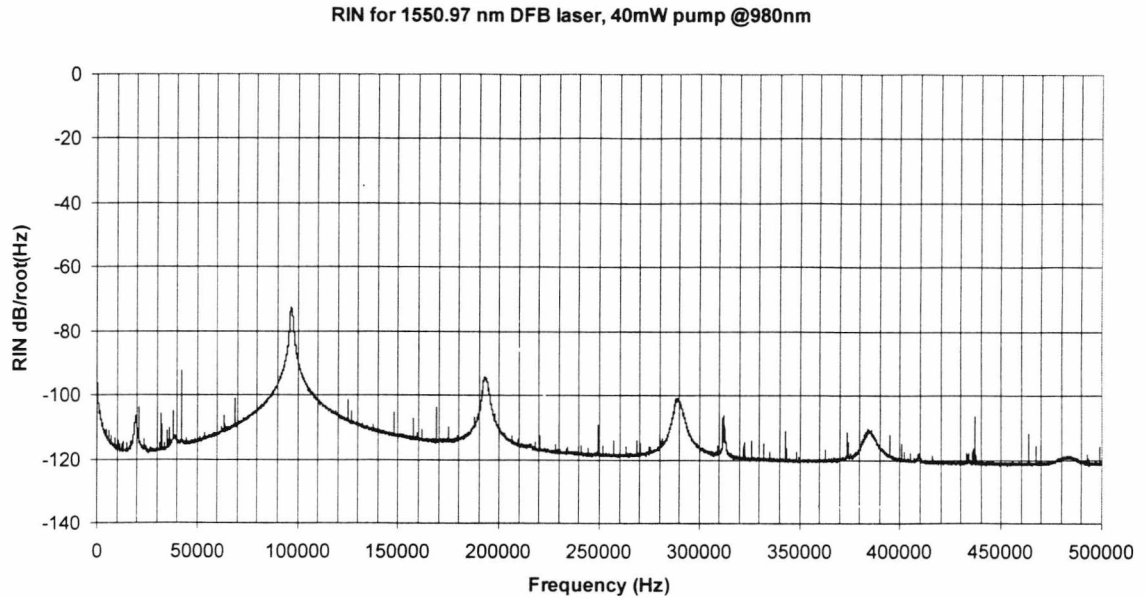
Figure 6.22   RIN at 40 mW 980 nm pump power for 1550.97 nm DFB laser

Comparing figures 6.22 and 6.23 shows that the relaxation oscillation frequency is increased for higher pump powers, as expected. Also shown are the higher harmonics of the oscillation frequency. For 80 mW pump power the main peak of the relaxation oscillation occurs at ~145 kHz.

RIN for 1550.97 DFB laser, 80 mW pump @980nm
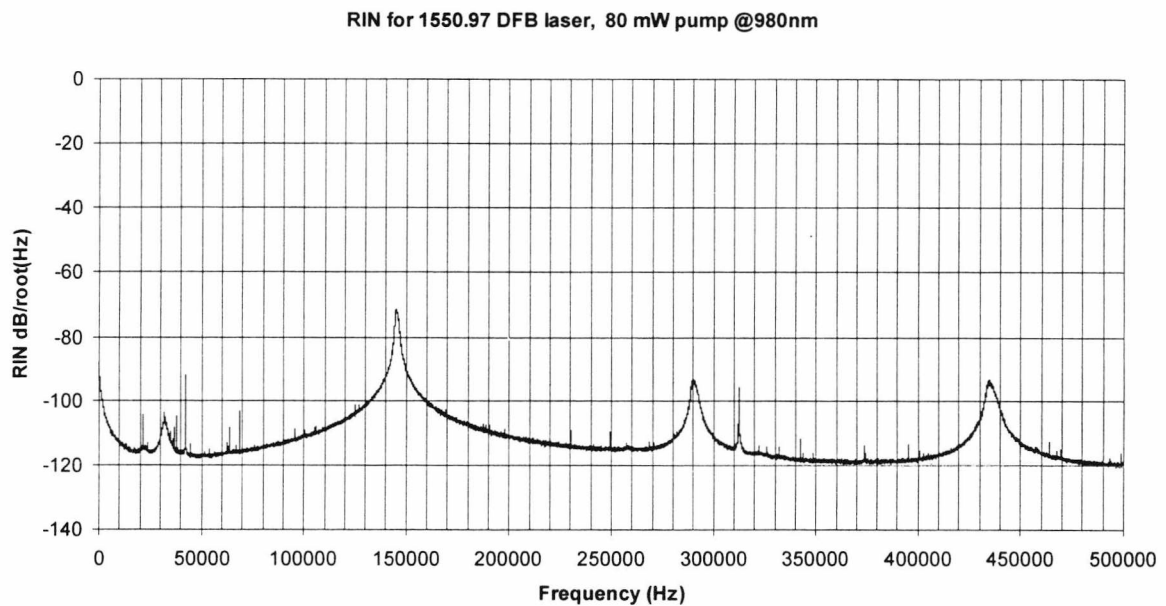
Figure 6.23   RIN at 80 mW pump for 1550.97 nm DFB laser

Also shown is a smaller amplitude peak at around 36 kHz. This is due to spurious electrical pickup and is not thought to be associated with the relaxation oscillations. The relaxation oscillations are at a much higher frequency than the acoustic signals of interest for all four of the DFB lasers, so there is no significant conflict between the two. It is of some interest to plot the variation of the relaxation oscillation frequency with optical pump power. This is shown below in figure 6.24 below for one of the DBR lasers (Lucent DBR laser). The variation for the DFB lasers will be of a similar nature.
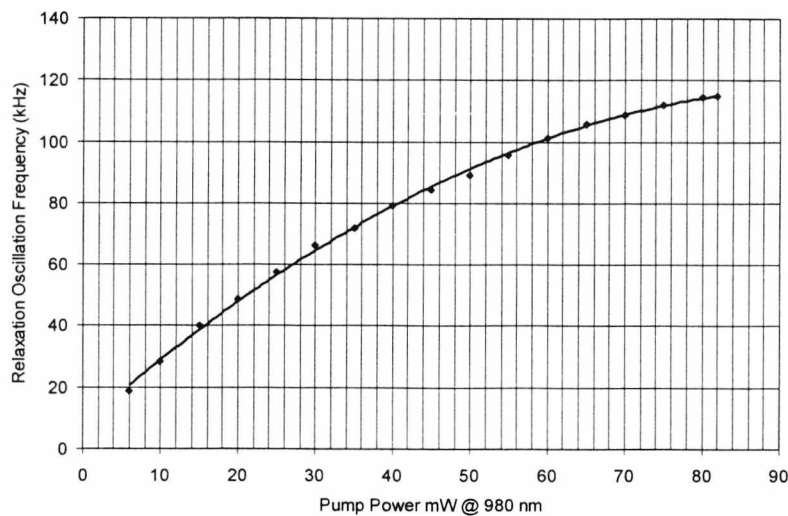
Figure 6.24 Variation of relaxation oscillation frequency as a function of optical pump power for Lucent DBR laser.

Figure 6.24 demonstrates that even for moderate optical pump powers the relaxation oscillation frequency is significantly above the acoustic signals of interest.

6.10.2 Phase noise measurement.

To eliminate the intensity noise, a balanced detection system was used as shown in figure 6.25 overleaf. The intensity noise is split equally between the two Mach-Zehnder outputs and is unchanged in amplitude by the presence of the path imbalance coil. The two detectors were InGaAs p-i-n diodes, type New Focus model 1811-FC with a DC-125 MHz bandwidth.
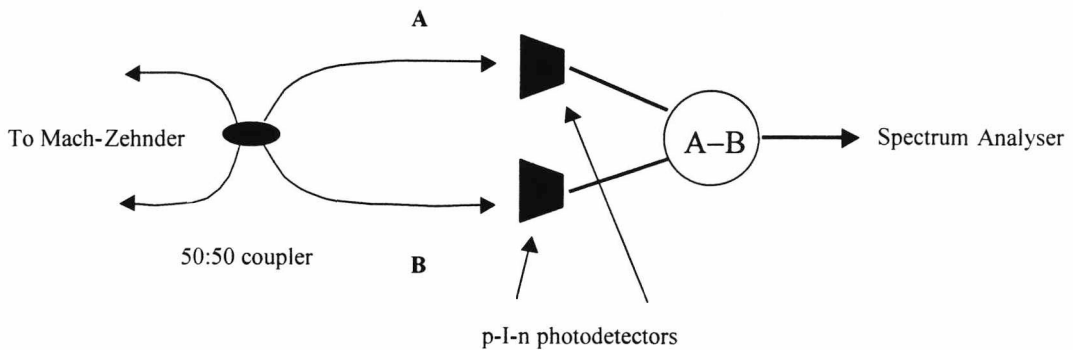
Figure 6.25 Balanced detection system for phase noise measurement

As the A,B outputs of the interferometer are in antiphase so far as the phase noise is concerned the balanced detection system shown above will eliminate the intensity noise and allow only the phase noise to be measured, assuming that the A,B output optical powers are identical and that the gains of the two detectors are identical.

In practice the gains of the two detectors were manually adjusted with a zero interferometer path imbalance to compensate for any asymmetry in the coupler splitting ratio, nominally 50:50 but with some variation ($\sim\pm 1\%$) due to manufacturing tolerances. This allowed the intensity noise to be minimised and the phase noise to be measured with the path imbalance in place. This was done for one laser (IONAS 1550.65 nm DFB), the entire system including the fibre laser being enclosed in the vacuum vessel as described previously. The results of this measurement are shown in figure 6.26 overleaf in dB relative to a phase shift of 1 radian/$\sqrt{\text{Hz}}$ normalised to a 1 m path imbalance. Figure 6.26 was calculated using the following expression:

$$\text{Phase noise in dB re. 1 rad/}\sqrt{\text{Hz}} = 20\log\left(\frac{V_{NOISE}}{\Delta P \cdot G \cdot \sqrt{BW}}\right) \quad\quad (6.14)$$

Where ΔP is the path imbalance in metres, G is the detector gain in volts/radian and BW is the spectrum analyser bandwidth in Hz. Of the four parameters in the above formula, three (ΔP, V_{NOISE}, BW) were easily measured.

Phase noise for 1560.55 nm laser in dB re. 1radian/rootHz
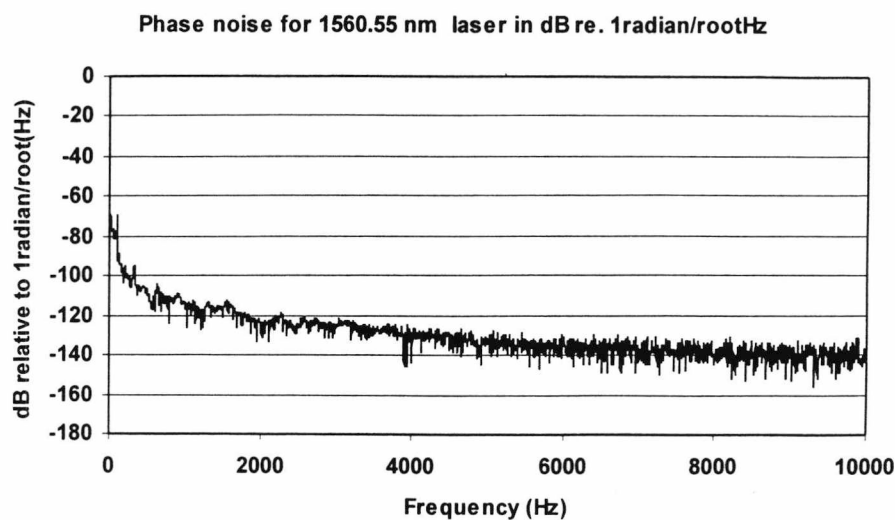
Figure 6.26 – Typical frequency dependence of laser phase noise.

To determine the detector gain G in volts/radian the Bragg cell was removed and the interferometer allowed to drift over a period of some minutes, the detector DC level being measured on an oscilloscope. Hence the detector gain in volts/radian could be easily calculated. As the interferometer transfer function is non-linear some further analysis was required in order to find the detector gain G in volts/radian averaged over the interferometer (cosine) transfer function. This is illustrated below in figure 6.27 which gives a representation of the interferometer drift with time.
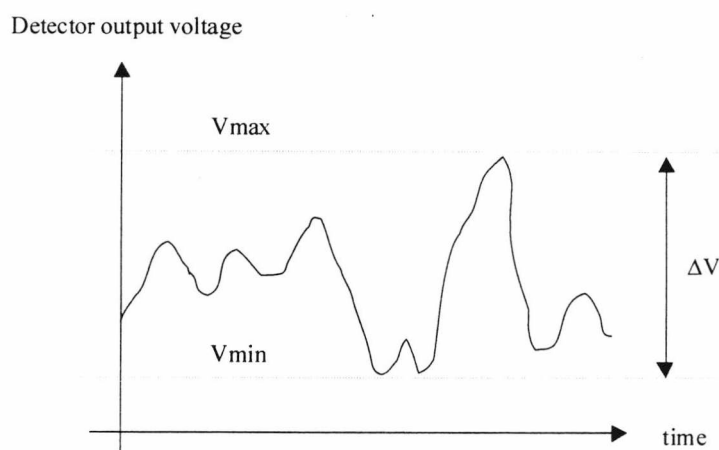
Figure 6.27 - Interferometer and detector DC level drift

The detector gain G averaged over the interferometer (cosine) transfer function is given by:

$$G = \frac{\frac{\Delta V}{2} \int_0^{\pi/2} \cos \Phi \cdot \delta \Phi}{\pi/2} = \frac{\Delta V}{2} \cdot \frac{2}{\pi} = \frac{\Delta V}{\pi} \qquad (6.15)$$

as the integral of the cosine transfer function over the specified range is equal to 1. Hence G is readily calculated from a relatively simple measurement.

6.11 DFB Fibre Laser Acoustic Response

The noise limited pressure resolution of the 1550.97 nm DFB laser was measured using the electret microphone and a path imbalance of 4.2 km in an attempt to maximise the acoustic detection sensitivity. The NLPR for this laser is given in figure 6.28. As for the previous measurements on the DBR lasers, figure 6.28 can at best only be an indication
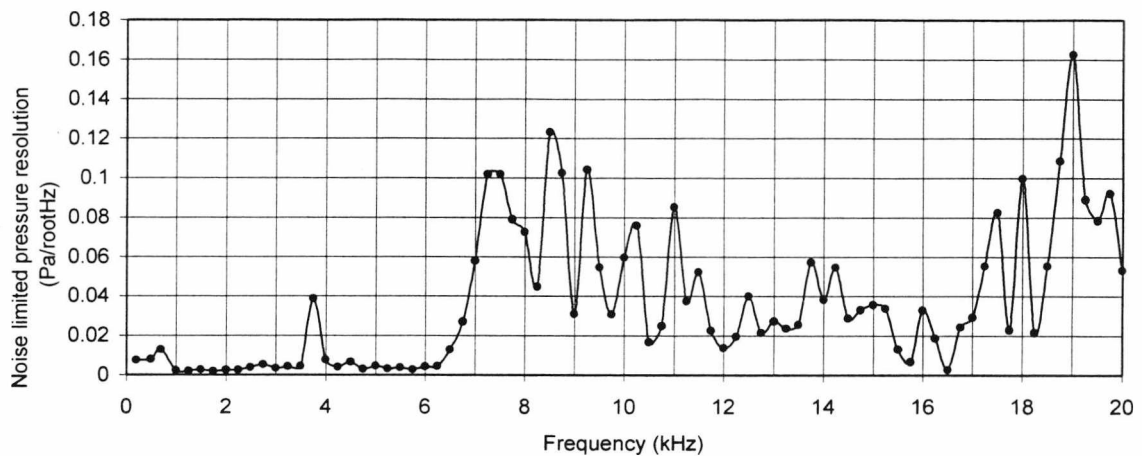
Figure 6.28 – 1550.97 nm IONAS DFB laser acoustic response

Unlike the DBR lasers which were bare fibre, the DFB lasers were recoated after being written into the fibre core. The presence of a polymer coating can significantly enhance the fibre acoustic sensitivity [27,28] if the coating is sufficiently thick (~5mm) However, the recoating performed on the lasers used here was simply a re-application

of the standard fibre coating found on telecom fibres, and would have no significant effect on the laser acoustic sensitivity due to the thinness (~125μm) of the coating. From figure 6.27, in the 0-1 kHz region a noise limited resolution of 0.01 Pa/√Hz is obtained (-40 dB re 1Pa√Hz). However, just above 1 kHz the resolution is 0.002 Pa/√Hz (-54 dB re 1Pa√Hz). Due to the effect of mechanical resonances and room noise, this latter figure could well be a better indication of the true performance of the system and is only 26 dB (a factor of 20) above DSS0. This is within reach of the amplification available from an acoustically compliant coating. [28, 29, 30].

6.12   Fundamental Limiting Factors on the Acoustic Detection Sensitivity.

6.12.1 Laser Phase Noise.

The laser phase noise is a maximum in the frequency regime of most interest. From figure 6.26, a typical value over the range 0-3 kHz is −120 dB relative to 1 radian/√Hz, (or 1 μradian/√Hz) normalised to a 1m path imbalance, which for this system corresponds to a pressure resolution of approximately 3μPa/√Hz. This figure is calculated using measurements of the sideband amplitude relative to the carrier for a known acoustic modulation pressure. From experimental measurements using the calibrated electret microphone, a pressure amplitude of ~0.064 Pa corresponds to a phase shift of ~0.022 radians in the Mach-Zehnder output, the phase shift being obtained simply from the amplitude of the sideband and by using the small-value approximation for the first–order Bessel function. Hence a noise value of 1 μradian/√Hz corresponds to a laser phase noise floor of ~3μPa/√Hz normalised to a 1 metre path imbalance. The phase noise is a fundamental property of the laser and unlike the relative intensity noise cannot be reduced by further signal processing.

6.12.2   Thermodynamic Phase Fluctuations.

As described previously, random thermodynamic fluctuations in the optical fibre give rise to density and hence refractive index changes in the fibre core. These random fluctuations manifest themselves as a source of phase noise in addition to the intrinsic laser phase noise and give rise to a minimum detectable phase shift in any interferometric system with long path imbalances. From [21], the r.m.s. phase noise amplitude exhibits a linear temperature dependence. Hence this noise source could be reduced by cooling the path imbalance coil, although a significant degree of cooling would be required in order for a substantial noise reduction to take place. Although not measured here, a typical value of this noise source is ~0.6μrad/√Hz [21] (or −125 dB

relative to 1 radian/√Hz) in the frequency range 0-3 kHz for a path imbalance of 100 metres, which for this system corresponds to a pressure resolution of ~2μPa/√Hz, this pressure resolution figure being calculated as for the laser phase noise. This is also a fundamental noise source and cannot be reduced by further signal processing. From [21], the r.m.s. amplitude of this source scales as $\sqrt{L_{MZ}}$, where L_{MZ} is the interferometer path imbalance. Hence this noise source scales more slowly with increased path imbalance than the laser phase noise or the signal..

6.12.3 Optical Shot Noise.

The shot noise for a typical detector input power of 1μW from the fibre lasers is approximately −125 dB/√Hz [17], corresponding to a shot noise limited pressure resolution of ~1μPa/√Hz. This figure is unaffected by the interferometer path imbalance and is relatively insignificant by comparison with the relative intensity noise noise figure.

6.12.4 Laser Relative Intensity Noise.

From figure 6.23, a typical value for the relative intensity noise (RIN) is −110dB/√Hz over the frequency range 0-10 kHz, corresponding to a noise limited pressure resolution of ~35 μPa/√Hz. This noise source can be effectively minimised by using a balanced detection technique as discussed previously when measuring the laser phase noise. The relative contributions of the system noise sources are summarized in table 6.6.

Noise Source	Measurement frequency range (kHz)	Contribution to Noise Limited Pressure Resolution (Pa/√Hz) (Average over frequency range)
Laser phase noise	0 - 3	~300 μPa/√Hz (100m path imbalance)
Thermodynamic phase fluctuations	0 - 3	~2μPa/√Hz (100m path imbalance)
Optical shot noise	0 - 3	~1 μPa/√Hz
Laser relative intensity noise	0 – 10	~35 μPa/√Hz

Table 6.6 – Contributions of system noise sources to Noise Limited Pressure Resolution.

Adding the noise sources in quadrature results in a theoretical noise limited pressure resolution for the multiplexed system of ~300 μPa/$\sqrt{\text{Hz}}$, as the other noise sources are small compared to the magnitude of the laser phase noise. Hence the laser phase noise is the limiting noise source in this system and gives a NLPR a factor 3 above the DSSO figure of 100 μPa/$\sqrt{\text{Hz}}$.

6.13   Comparison of Demultiplexing Techniques.

Two methods of demultiplexing the laser array were examined in some detail. The first involved the use of a customised commercially available monochromator; the second involved the use of a commercial thin film interference Bandpass Wavelength Division Multiplexer (BWDM).

6.13.1 Digikrom Monochromator

A schematic of the internal layout of the monochromator is shown below in figure 6.29. The Digikrom monochromator investigated for signal demultiplexing is a commercially available unit (model DK480) which utilises spherical rather than imaging-spectrograph optics. The optics were enclosed in a rigid steel case 0.5 m long which could be dismantled to allow adjustment of the internal optics if required. The use of spherical optics has implications for the dispersive/focussing performance of the spectrometer, as was ascertained by 3D mapping of the output using singlemode input/output test-fibres, with the following results:
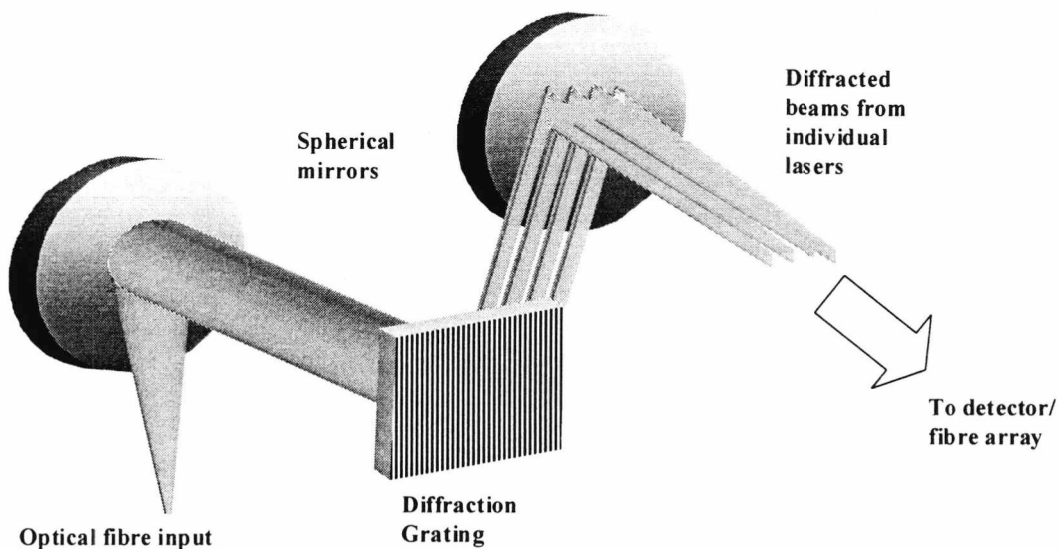
Figure 6.29 – Schematic of internal optics of Digikrom monochromator

- The location of the smallest output spot size in the vertical direction (i.e. along direction of the input slit) is ~6.5cm outside the case.

- The location of optimal dispersion (i.e. of smallest spot size per unit bandwidth in the horizontal direction) is ~4.5cm outside the case. At this location, the vertical spot size rises from a minimum of a few tens of microns to ~2.5mm, so that if a monomode fibre is used to collect the light, the collection efficiency is ~0.06%. Hence the spectrometer, as supplied, is not set up for simultaneous optimal dispersion and efficient focussing.

These results imply that the collection efficiency for the diffracted laser signals needs to be significantly increased. The use of a 6cm focal length lens outside the monochromator's case was shown to significantly reduce the vertical divergence at the plane of optimal dispersion, increasing the transmission from ~0.06% to ~0.6%. However, when stripping down the monochromator (removing the outer case) and paying close attention to x-y-z and angular positioning of the input signal, it was found to be possible (when using unpolarised input) to increase the detection efficiency with respect to the diameter of the receiving detector as shown below in Table 6.7.

Detector Diameter	Detection Efficiency
>1 cm	69%
400 μm	47%
300 μm	41%
200 μm	28%

Table 6.7 – Detection efficiency as a function of detector diameter

The maximum diameter of the detector is determined (in the absence of other factors) by the dispersion of the monochromator. Early experiments suggested that this was about 450 microns per dispersed spot. A survey of available photodiodes showed that a device of 1mm photosensitive diameter (Hamamatsu G5832-01), having a dark current of 1nA would be suitable if used in conjunction with a large-core diameter multimode fibre. Considering the distance between the photosensitive surface of this device and its window (~1mm), calculations suggested that Elliot Scientific FG-365-LER fibre would

be most suitable. This fibre has an NA of 0.22, a core diameter of 365 microns and a cladding diameter of 425 microns.

6.13.2 Modifications to the monochromator

Early design considerations were constrained by the need for the laser signals to be input via an FC/APC bulkhead connector, and the output signals (from the dispersed spots) to be collected via 2 m long multimode optical fibres. The FC/APC input was applied by means of suitable modification to the end-plate of the monochromator. The internal monomode fibre from this endplate was directed toward a horizontal platform, which was attached to an existing input side-plate on the monochromator. The output multimode fibres were intended to be attached to a platform with vertical adjustment, this platform being attached to the existing output side-plate of the monochromator. The output multimode fibres were intended to be cabled with 3 mm furcation tubing (4 were already), and a means for outputting 8 fibres through the monochromator end-plate was provided by means of a clamping mechanism for rigidity. These fibres were terminated with SMA connectors. The need for these mechanical modifications suggested that the monochromator would be difficult to use practically.

6.13.3 Characterisation of the monochromator response

The following experimental measurements were obtained :

- The overall monochromator transmission at about 1550 nm, using the discussed fibre design and unpolarised input, was measured to be about 45%.

- Using an input of least optimal linear polarisation, the transmission was measured to be about 18%. Hence the response is highly polarization dependent.

- A number of design imperfections were noted. Attaching the fibre platforms to the monochromator side-plates was undesirable as these acted as cantilevers: application of perpendicular force led to significant signal loss. The platforms should have been built more robustly from the monochromator base. Second, the specification for an FC/APC input was, perhaps, short-sighted. The fibre-end directed toward the input collimating mirror needs a 90° cleave. Thus, the input side-plate may just as well been modified to mount an FC/PC connectorised fibre.

6.13.4 Evaluation with DFB lasers

The DFB lasers cover the 4 400 GHz ITU channels from 1550.92 to 1560.61 nm; the spectrum from an optical spectrum analyser (OSA) of the 4 element array being shown in figure 6.30.
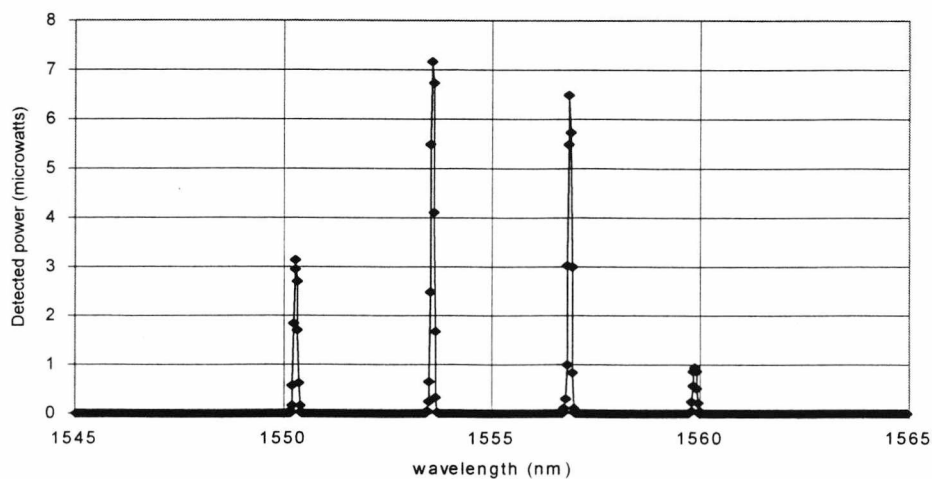
Figure 6.30 – OSA plot of laser array output signals

When using an 80mW 980nm pump signal (with no Mach-Zehnder interrogating interferometer), the profile of intensity versus lateral displacement at the output of the monochromator obtained with the DFB laser array is shown in figure 6.31 overleaf. This is similar to that of figure 6.30, except with a broadened response. The fibre lasers were spliced such that the least powerful was first in the line (and so on). This gave a spread of intensities of a factor of 6. The lateral displacement between peak intensities is larger than initially expected. Four hundred micron cored multimode fibres could have been used giving a few extra percent transmission. The worst cross-talk between the detected signals was measured to be 5 parts in 10^4. The data for the above figure were obtained at a random state of polarisation – there was no polarisation input control to the monochromator. Varying the state of input polarisation with a coiled birefringent

polarization controller was shown to vary the overall transmission between 34% and 56% .
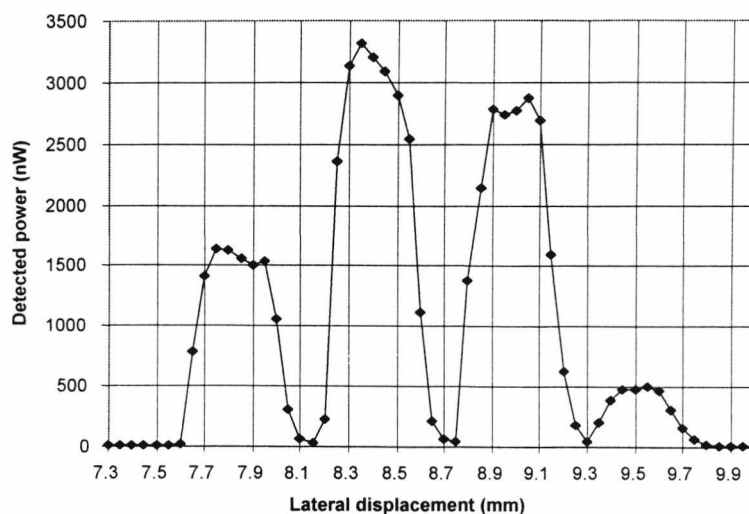
Figure 6.31 – Monochromator output with 4 DFB laser array

6.13.5 Bandpass Wavelength Division Multiplexer (BWDM)

This is a hybrid fibre optic/interference thin film filter based device with a bandpass response centered around the individual laser wavelengths. The key component of the filter is a thin-film dielectric interference coating on a glass or polymer substrate. The interference coatings consist of alternating thin layers of high and low refractive index materials such as SiO_2 and Ta_2O_5. The multiple coating layers form dielectric cavities that selectively transmit or reflect light depending on the wavelength. The lasers were constructed so has to have a one-to-one wavelength correspondence with the bandpass response of this commercially available device. As the BWDM is fully connectorised with FC/PC connectors optical losses are minimised. Preliminary measurements were in agreement with the specified losses of the BWDM of between 2.5-3 dB per channel. The bandpass width is approximately 0.8 nm, so temperature-induced shifts in the DFB laser wavelengths would not adversely effect the system sensitivity. The use of a BWDM is somewhat different from the monochromator. The BWDM has FC-PC connectors (rather than SMA), is singlemode and can thus

be used with smaller active-area photodiodes. With the DFB fibre lasers, this device gave the following performance:

- An average transmission of 60% (10% more than the monochromator configuration).
- A worst case cross-talk of 4 parts in 10^5 (an order of magnitude better than the monochromator).
- Polarisation: the polarisation dependent loss has a specified maximum of less than 3%.

Hence the BWDM provides a more readily usable and compact method of interrogating the laser array than the monochromator. The transmission and signal separation characteristics of the BWDM are superior to those of the monochromator, which is bulky (0.5 m long, 45 kg mass), relatively fragile and would need careful mechanical adjustment in order to provide a suitable response. Therefore the preferred demultiplexing method for the laser array is the BWDM.

6.14 Summary and Further Work.

6.14.1 Comparsion of acoustic detection techniques.

The DBR and DFB fibre laser noise limited pressure resolutions (NLPR) are summarized below in table 6.8 below, along with the acoustic pressure sensitivity derived from the 2.5 cm length DBR laser used in [15]. Also included for comparison purposes are the acoustic detection sensitivities of the interferometer-based hydrophone systems discussed previously in this chapter.

Acoustic sensor type	λ(nm)	M-Z Path imbalance (m)	Measurement frequency range (kHz)	Noise Limited Pressure Resolution (μPa/√Hz)	Sensitivity relative to DSSO (dB)
Lucent DBR Er^{3+} fibre laser	1568	100	4-6	20000	+46
Lucent DBR Er^{3+} fibre laser	1568	4200	4-6	400	+12
Fibrecore DBR	1548	100	4-6	20000	+46
DBR Er^{3+} fibre laser [ref 15]	1554	100	7	6000	+35
IONAS DFB Er^{3+} fibre laser with DWDM multiplexing	1551	100	0 - 1	10000	+40
IONAS DFB Er^{3+} fibre laser with DWDM multiplexing	1551	4200	1 -3	2000	+26
Single unbalanced Mach-Zehnder interferometer with acoustically compliant mandrel [3]	-	~100	0 - 3	3	-30 dB
Low finesse Fabry-Perot cavities with gated phase modulated heterodyne demultiplexing. [4]	-	-	0 – 3	100	0 dB
Unbalanced Mach-Zehnder with acoustically compliant mandrel with phase generated carrier multiplexing. [3]	-	~100	0 – 3	~32	-10 dB
Unbalanced Mach-Zehnder with acoustically compliant mandrel with time division multiplexing. [3]	-	~100	400 Hz – 2 kHz	-32	-10 dB

Table 6.8 Experimentally measured fibre laser acoustic pressure sensitivities.

Table 6.8 demonstrates that the use of a larger interferometer path imbalance with the fibre laser sensors gives a significant increase in the system sensitivity, although as mentioned previously, the figures above are at best an indication of the laser acoustic sensitivity. This is due to the effects of mechanical resonances in the fibre and the uncertainties in the measured acoustic pressure incident on the laser. The highest acoustic detection sensitivity achieved for both the DBR and DFB lasers was for the Lucent DBR laser with a 4.2 km M-Z path imbalance. Here the sensitivity was a factor of 12 dB above DSSO. For the DFB lasers with the DWDM multiplexing, a factor of 26 dB above DSSO was achieved for the IONAS 1551 nm laser. Table 6.8 also demonstrates that interferometer-based acoustic sensors readily achieve detection sensitivities of, or even in excess of DSSO. It is important to note that for strict comparison purposes, the lasers would need to be acoustically excited in water. This would constitute a significant body of further research and would allow a more direct comparison to be made between different systems.

6.14.2 Limiting noise sources in laser based acoustic detection systems.

The limiting noise source in the system was found to be the laser phase noise, which from examination of table 6.9 can be seen to be a factor of approximately 9 greater than the next largest noise source, the laser relative intensity noise.

Noise Source	Measurement frequency range (kHz)	Contribution to Noise Limited Pressure Resolution (Pa/√Hz) (Average over frequency range)
Laser phase noise [21,22,23]	0 - 3	~300 µPa/√Hz (100m path imbalance)
Thermodynamic phase fluctuations in interferometer path imbalance coil.	0 - 3	~2µPa/√Hz (100m path imbalance)
Optical shot noise	0 - 3	~1 µPa/√Hz
Laser relative intensity noise	0 – 10	~35 µPa/√Hz

Table 6.9 – Contributions of system noise sources to Noise Limited Pressure Resolution.

From table 6.8, the Lucent DBR laser with a 4.2 km interferometer path imbalance appears to be able to reach a noise limited pressure resolution approaching the noise floor determined by the laser phase noise.

6.14.3 Comparison of demultiplexing techniques.

As can be seen from the comparison section where the BWDM and the monochromator are compared, by far the most compact, simple and cost effective (~£1500) method of demultiplexing the laser array is the BWDM, as this device provides low inter-channel cross-talk coupled with high signal transmission. The transmission and signal separation characteristics of the BWDM are superior to those of the Digikrom DK480 monochromator, which is bulky (0.5 m long, 45kg mass), relatively fragile, more expensive (~£4000) and would need careful mechanical adjustment (and mechanical modification) in order to provide a suitable response. Therefore the preferred demultiplexing method for the laser array is the BWDM. Hence the use of a bulk-optic monochromator is unviable as an effective means of demultiplexing an array of fibre lasers.

6.14.4 Suggested further work.

- Coating the fibre lasers with an acoustically compliant coating [28,29,30] would allow pressure detection sensitivities of or possibly exceeding DSSO to be achieved, even with the relatively simple optical arrangement detailed in this chapter. This aspect of coating the fibre lasers with an acoustically amplifying coating could be performed in conjunction with measuring the acoustic detection sensitivities in water. This approach was not investigated in this thesis due to time and equipment constraints.

- Minimisation of the relative intensity noise could be achieved by the use of a balanced detection system as used here to measure the phase noise amplitude.

- A significant improvement in the amplifier noise floor could be achieved by the use of a second acousto-optic Bragg cell in the other arm of the interferometer, offset in frequency from the first by a known frequency of several tens of kHz or possibly a few hundred kHz. This would create a second, lower optical carrier frequency than the 40 MHz of the original Bragg cell. The acoustic signal would be heterodyned with this lower carrier frequency, allowing the use of highly frequency selective phase-lock signal recovery techniques such as lock-in amplification.

References:

1.   BUCARO, J.A., DARDY, H.D., CAROME, E.F.: 'Fibre-optic hydrophone', J. Acoust. Soc. Amer., 1977, **62**, pp. 1302-1304.

2.   COLE, J.H., LAGAKOS, N., BUCARO, J.A.: 'Advances in fiber optic based acoustic sensors', Proc. SPIE, 1982, **326**, pp. 116-126.

3.   NASH, P.: 'Review of interferometric optical hydrophone technology', IEE Proc. Radar, Sonar Navig., **143,** No. 3, Jun. 1996.

4.   DAKIN, J.P., WADE, C.A., HENNING, M.L. : 'Novel optical fibre hydrophone array using a single laser source and detector', Electronics Letters, **18**, 1984, pp . 302-305.

5.   DANDRIDGE, A. : 'The development of fiber optic sensor systems', Proc SPIE, 1994, 2360, pp. 154-161.

6.   KERSEY, A.D., MARRONE, M.J., DANDRIDGE, A.: 'Experimental investigation of polarization induced fading in interferometric fibre sensor arrays.', Electronics Letters, 1991, **27**, No. 7, pp 562-563.

7.   KERSEY, A.D., MARRONE, M.J., DAVIS, M.A.: 'Polarisation insensitive fibre optic Michelson interferometer', Electronics Letters, 1991, **27**, No. 6, pp 518-520.

8.   BOGER, Y.S., TUR, M.: 'Polarisation Induced Fading in Interferometric Sensor Arrays', Electronics Letters, **27**, No.8, 11th April 1991, pp 622-623.

9.   MEARS, R.J., BAKER, S.R.: 'Erbium Fibre Amplifiers and Lasers', Optical and Quantum Electronics, **24**, 1992, pp. 539-553.

10.   GILES, C.R., DESURVIRE, E.: 'Propagation of Signal and Noise in Concatenated Erbium-Doped Fiber Optical Amplifiers.', Journal of Lightwave Technology, Feb. 1995, **9**, No 2.

11.   MORKEL, P.R., LAMING, R.I.: 'Theoretical Modeling of erbium-doped fibre amplifiers with excited-state absorbtion.', Optics Letters, **14**, Oct. 1989, No. 19.

12.   BALL, G.A., GLENN, W.H.: 'Design of a Single-Mode Linear-Cavity Erbium Fiber Laser Utilizing Bragg Reflectors.', Journal of Lightwave Technology, July 1995, **10**, No.10.

13.   ZYSKIND, J.L., MIZRAHI, V., DIGIOVANNI, D.J., SULHOFF, J.W.: 'Short
       single frequency erbium-doped fibre laser.', Electronics Letters, 16th July 1992,
       28, No. 15

14.   KOO, K.P., KERSEY, A.D.: 'Bragg Grating-Based Laser Sensors Systems
       with Interferometric Interrogation and Wavelength Division Multiplexing.',
       Journal of Lightwave Technology, July 1995, **13**, No.6.

15.   KOO, K.P., KERSEY, A.D.: 'Fibre laser sensor with ultrahigh strain resolution
       using interferometric interrogation', Electronics Letters, 6th Jul. 1995, **31**,
       No. 14.

16.   SEJKA, M., VARMING, P., HUBNER, J., KRISTENSEN, M.: ' Distributed
       Feedback Er^{3+} doped fibre laser.', Electronics Letters, 17th Aug. 1995, **31**,
       No.16.

17.   YARIV, A.: 'Optical Electronics', 4th Edition, Saunders College Publishing.

18.   WANSER, K.H.: 'Fundamental phase noise limit in optical fibres due to
       temperature fluctuations.', Electronics Letters, 2nd Jan. 1992, **28**, No.1.

19.   BALL, G.A., MELTZ, G., MOREY, W. W.: 'Polarimetric heterodyning Bragg-
       grating fiber laser Sensor', Optics Letters, **18**, No. 22, Nov. 15th,1993.

20.   KIM, H.K., KIM, S.K., PARK, H.G., KIM, B.Y.: 'Polarimetric Fiber Laser
       Sensors', Optics Letters, **18**, No. 4, Feb. 15th,1993.

21.   WANSER, K.H., KERSEY, A.D., DANDRIDGE, A.: 'Measurement of
       fundamental thermal phase fluctuations in optical fibre.' Proc. OFS-9, Firenze,
       Italy, May 4th-6th 1993, pp. 255-256.

22.   GLENN, W.H.: 'Noise in Interferometric Optical Systems - an Optical Nyquist
       Theorem.' IEEE Journal of Quantum Electronics, June 1989, **25**, No. 6.

23.   MOSLEHI, B.: 'Noise Power Spectra of Optical Two-Beam Interferometers
       Induced by the Laser Phase Noise.', Journal of Lightwave Technology, Nov.
       1986, **4**, No.11

24.   CONSTABLE, J.A., WHITE, I.H., 'Laser linewidth measurement using a
       Mach-Zehnder interferometer and an optical amplifier', Electronics Letters, 20th
       Jan. 1994, **30**, No. 2.

25.   OKOSHI, T., KIKUCHI, K., NAKAYAMA, A.: 'Novel Method for High Resolution measurement of laser output spectrum.', Electronics Letters, 31st July 1980, **16**, No.16.

26.   SCHMID, W., JUNG, C., WEIGL, B., REINER, G., MICHALZIK, R., EBELING, K.J.: 'Delayed Self-Heterodyne Linewidth Measurement of VCSEL's', IEEE Photonics Technology Letters, Oct. 1996, **8**, No.10.

27.   HOCKER, G.B.: 'Fiber optic acoustic sensors with composite structure: an analysis', Applied Optics, **18**, No. 21, 1st Nov. 1979, pp. 3679-3683.

28.   BUDIANSKY, B., DRUCKER, D.C., KINO, G.S., RICE, J.R.: 'Pressure Sensitivity of a clad optical fibre.', Applied Optics, 15th Dec. 1979, **18**, No. 24.

29.   HUGHES, R., JARZYNSKI, J.: 'Static pressure sensitivity amplification in interferometric fiber-optic hydrophones.', Applied Optics, 1st Jan. 1980, **19**, No. 1.

30.   LAGAKOS, N., SCHNAUS, E.U., COLE, J.H., JARZYNSKI, J., BUCARO, J.A.: 'Optimising fiber coatings for interferometric acoustic sensors', IEEE Journal of Quantum Electronics, **18**, No. 4, April 1982.

31.   RONNELEIV,E., LOVSETH, S.W.,: 'Stability of distributed fibre lasers with optical feedback', OFS 13, Korea, SPIE 3746, P2-15, April 1999. Page: 181

Chapter 7

Summary and Further Work.

7.1   Summary.

Table 7.1 summarises the results of the experimental measurements of the noise limited pressure resolutions for the FBG, the low-finesse polymer film cavity and the erbium fibre laser sensors.

Sensor type	Frequency	Noise limited pressure resolution
5mm FBG	1.911 MHz	4.5 kPa/√Hz
Low-finesse PET polymer film cavity	1.911 MHz, 0.612 MHz	72 Pa/√Hz 11 Pa/√Hz
Lucent DBR Er³⁺ fibre laser	200Hz – 20 kHz.	400 μPa/√Hz

Table 7.1 Summary of experimental measurements of noise-limited pressure resolutions.

The figure for the noise limited pressure resolution in the case of the erbium laser sensor is that for the most sensitive laser.

7.1.1   Use of FBG's as ultrasonic detectors.

The use of FBGs to successfully detect MHz ultrasonic fields has been demonstrated. However, experimental results show conclusively, and the discussion in chapter 4 of travelling acoustic waves in acousto-optic fibre frequency shifters suggests, that point acoustic detection sensitivity cannot be achieved without some form of acoustic shielding on the bare fibre to avoid the transmission of acoustic compressional waves from elsewhere in the fibre to the FBG. It has been demonstrated that a Bragg grating may function effectively as a point ultrasonic probe with mm resolution if:

- The grating length is small (less than half the acoustic wavelength in fused silica).

- The fibre is appropriately desensitised using some form of acoustically damping coating. A distinct advantage that FBGs have over other forms of sensor are their potential to also simultaneously measure temperature.

Further work involving the use of FBG's as ultrasonic sensors could consist of :

- Using alternative forms of acoustically desensitising coatings as described in Chapter 4 to provide point ultrasonic detection sensitivity.

- Using a tunable ultrasonic source to assess the frequency response of a FBG sensor.

- Investigation of an array of FBG's with acoustically desensitising coatings to determine the potential of such an array for use in therapeutic applications of ultrasound.

7.1.2   Use of low-finesse cavities as ultrasonic detectors.

Further investigations would benefit from the availability of some form of tunable ultrasonic source so that the sensor frequency response could be more accurately assessed over a more comprehensive frequency range. At an ultrasonic frequency of 612 kHz the acoustic sensitivity is only an order of magnitude less than the significantly more expensive calibrated PVDF hydrophone. This suggests that the simple design investigated in chapter 5 may provide a cheap alternative to more expensive commercially available hydrophones. The use of other polymers with a lower Young's modulus than the PET film (e.g. polythene) would potentially provide higher ultrasonic detection sensitivities, as discussed in Chapter 5.

Hence further work could consist of :

- Investigation of the frequency response of a low-finesse polymer film cavity by using a tunable ultrasonic source. This would allow a more direct comparison of the sensor response with the results of the previous studies discussed in Chapter 5 of this thesis.

- Investigation of methods of bonding polymer films to the end of a cleaved single-mode fibre to allow the construction of sensors considerably smaller (~125µm diameter) than those investigated previously (~1.6 mm diameter).

7.1.3   Use of erbium fibre lasers as acoustic detectors.

The limiting noise source in the laser interrogation system was found to be the laser phase noise. The simplest method of demultiplexing an array of fibre lasers was by using a commercially available Bandpass Wavelength Division Multiplexer (BWDM) as discussed in chapter 6, where a comparison of a BWDM and a commercially available monochromator was performed. Further work on the erbium fibre laser system could consist of:

- Coating the fibre lasers with an acoustically compliant coating would allow pressure detection sensitivities of or possibly exceeding DSSO to be achieved, even with the relatively simple optical arrangement detailed in this chapter. This aspect of coating the fibre lasers with an acoustically amplifying coating could be performed in conjunction with measuring the acoustic detection sensitivities in water. This approach was not investigated in this thesis due to time and equipment constraints.

- Minimisation of the relative intensity noise could be achieved by the use of a balanced detection system as used here to measure the phase noise amplitude.

- A significant improvement in the amplifier noise floor could potentially be achieved by the use of a second acousto-optic Bragg cell in the other arm of the interferometer, offset in frequency from the first by a known frequency of several tens of kHz or possibly a few hundred kHz. This would create a second, lower optical carrier frequency than the 40 MHz of the original Bragg cell. The acoustic signal would be heterodyned with this lower carrier frequency, allowing the use of highly frequency selective phase-lock signal recovery techniques such as lock-in amplification.

Conference papers and presentations arising from this thesis.

Response of in-fiber Bragg Gratings to focused ultrasonic fields.
N.E. Fisher, S.F. O'Neill et al., Proc. of International Conference on 12th Optical Fiber
Sensors, OWC12, pp. 190-193, October 1997.

High Frequency Ultrasound Detection using a fibre Bragg grating.
D.J. Webb, N.E. Fisher, S.F. O'Neill, I. Bennion, L. Zhang, L. Gavrilov, J.W.Hand, IEE
Electronics and Communications Colloquium on Optical Fibre Gratings, 26th March
1999, Aston University.

Use of Fibre Bragg Gratings to detect Ultrasonic Fields.
S.F. O'Neill, D.J. Webb, N.E. Fisher, I. Bennion, L. Zhang, L. Gavrilov, J.W.Hand,
IOP Applied Optics Division Conference, Brighton, 16-19 March, 1998, pp. 111-116.

A fiber laser hydrophone array.
D.J. Hill , P.J. Nash , D.A. Jackson, D.J. Webb, S.F. O'Neill, I. Bennion, and L. Zhang.
Proc. SPIE Vol. 3860. September 1999.

Acoustic Detection using Er3+ fibre Bragg grating lasers.
S.O'Neill. Conference Proceedings for Prep 2000 Second Conference on Postgraduate
Research in Electronics, Photonics and related fields. 11-13 April 2000, University of
Nottingham, UK. pp. 321-326.

Acoustic Detection using erbium fibre Bragg grating lasers.
S.F.O'Neill, D.J. Webb, D.A. Jackson, L. Zhang, I. Bennion, IOP Applied Optics and
Opto-Electronics Conference, 17-21 September 2000, Loughborough University.

Appendix A

Frequency spectrum of a phase modulated carrier.

From Chapter 3, the interferometer response to the modulated FBG is given by :

$$I_{OUT} = A[1 + V(L)\cos(\omega_C t + \phi(t) + \Phi + \delta\Phi \sin \omega_S t)] \tag{A1}$$

where ω_C, ω_S the are carrier and signal angular frequencies, A is a constant proportional to the FBG reflectivity, $\phi(t), \delta\Phi$ are the amplitudes of the environmental and measurand-induced phase shifts respectively and Φ is the static phase difference. The cosine term in (A1) above can be written in complex notation as:

$$s(t) = \mathrm{Re}[\exp(i(\omega_C t + \phi(t) + \Phi + \delta\Phi \sin \omega_S t))]$$

$$= \mathrm{Re}[\tilde{s}(t)\exp(i(\omega_C t + \phi(t) + \Phi))] \tag{A2}$$

where $\tilde{s}(t)$ is given by:

$$\tilde{s}(t) = \exp(i\delta\Phi \sin(\omega_S t)) \tag{A3}$$

The function $\tilde{s}(t)$ is a periodic function of time with a fundamental frequency equal to the modulation frequency $f_S (= \omega_S/2\pi)$. As the function is periodic a complex Fourier series approach can be used to find an expression for the frequency spectrum of the modulated carrier. Hence:

$$\tilde{s}(t) = \sum_{n=-\infty}^{+\infty} c_n \exp(in\omega_S t) \tag{A4}$$

where the complex Fourier coefficient c_n is defined by:

$$c_n = \frac{\omega_S}{2\pi} \int_{-\pi/\omega_S}^{\pi/\omega_S} \tilde{s}(t)\exp(-in\omega_S t) \cdot dt \tag{A5}$$

$$c_n = \frac{\omega_S}{2\pi} \int_{-\pi/\omega_S}^{\pi/\omega_S} \exp(i(\delta\Phi \sin(\omega_S t) - n\omega_S t)) \cdot dt \qquad (A6)$$

Writing $x = \omega_S t$ and setting the integral limits accordingly gives:

$$c_n = \frac{1}{2\pi} \int_{-\pi}^{\pi} \exp(i(\delta\Phi \sin(x) - nx)) \cdot dx \qquad (A7)$$

The integral above is the nth order Bessel function. Hence the coefficients of the Fourier series expansion are simply the Bessel functions of order n. Hence the modulating function $\tilde{s}(t) = \exp(i\delta\Phi \sin(\omega_S t))$ can be written as:

$$\tilde{s}(t) = \sum_{n=-\infty}^{\infty} J_n(\delta\Phi) \exp(in\omega_C t) \qquad (A8)$$

and equation (A2) can be reformulated as:

$$s(t) = \mathrm{Re}\left[\sum_{n=-\infty}^{\infty} J_n(\delta\Phi) \exp(i((\omega_C + n\omega_S)t + \phi(t) + \Phi)) \right] \qquad (A9)$$

which reduces to

$$s(t) = \sum_{n=-\infty}^{\infty} J_n(\delta\Phi) \cos\left[(\omega_C + n\omega_S)t + \phi(t) + \Phi\right] \qquad (A10)$$

Hence the interferometer response to a phase modulation from the FBG is given by:

$$I_{OUT} = A\left[1 + V(L) \sum_{n=-\infty}^{\infty} J_n(\delta\Phi) \cos[(\omega_C + n\omega_S)t + \phi(t) + \Phi]\right] \qquad (A11)$$

For small modulation amplitudes ($\delta\Phi \ll 1$) the Bessel functions can be approximated by the following formula.

$$J_n(x) \approx \frac{1}{n!}\left(\frac{x}{2}\right)^n + O(x^{n+2}) \qquad (A12)$$

where $O(x^{n+2})$ denotes terms of the order of $n+2$. The carrier amplitude will therefore be given by the zeroth-order Bessel function :

$$I_{CARRIER} = AV(L)J_0(\delta\Phi) = AV(L) \qquad (A13)$$

and the amplitude of the first sideband will be

$$I_{\omega_S} = AV(L)J_1(\delta\Phi) = A\exp-2\left(\frac{\pi L \Delta v}{c}\right)^2 \left(\frac{\pi L}{\lambda_B^2}\delta\lambda\right) \tag{A14}$$

Appendix B

Optimum optical path difference for maximum sideband amplitude.

The optimum value of optical path difference which maximises the value of the first sideband can be found by differentiating equation (A14) from Appendix 1, given below.

$$I_{\omega_S} = AV(L)J_1(\delta\Phi) = A\exp-2\left(\frac{\pi L \Delta v}{c}\right)^2 J_1\left(\frac{2\pi L}{\lambda_B^2}\delta\lambda\right) \tag{B1}$$

As this analysis assumes a small (<<1) value of phase modulation, the Bessel function J_1 can be approximated by :

$$J_1(x) \approx \frac{x}{2} \Rightarrow J_1\left(\frac{2\pi L}{\lambda_B^2}\delta\lambda\right) \approx \frac{\pi L \delta\lambda_B}{\lambda_B^2} \tag{B2}$$

Hence from (B1):

$$\frac{d}{dL}\left(\frac{\pi L \delta\lambda_B}{\lambda_B^2}\cdot\exp-2\left(\frac{\pi L \Delta v}{c}\right)^2\right) = 0 \tag{B3}$$

writing $x = 2\left(\frac{\pi L \Delta v}{c}\right)^2$ and $y = \frac{\pi L \delta\lambda_B}{\lambda_B^2}$ and applying the chain rule gives:

$$\frac{d}{dL}(y\cdot\exp-x) = y\cdot\frac{d}{dL}(\exp-x) + (\exp-x)\cdot\frac{dy}{dL} \tag{B4}$$

Using $\frac{d}{dL}(\exp-x) = -\exp-x\cdot\frac{dx}{dL}$ and $\frac{dx}{dL} = \left(\frac{2\pi\Delta v}{c}\right)^2 L$, (B4) can be reduced to:

$$\frac{\pi\delta\lambda_B}{\lambda_B^2} - \frac{\pi L \delta\lambda_B}{\lambda_B^2}\cdot\left(\frac{2\pi\Delta v}{c}\right)^2 L = 0$$

Gathering terms and cancelling gives $L_{OPTIMUM} = \dfrac{c}{2\pi\Delta v}$. For a grating bandwidth of ~0.2 nm at 820 nm this gives $L_{OPTIMUM} \approx 530$ μm.